A COMPONENT-BASED APPROACH TO MODELLING BEAM-END BUCKLING ADJACENT TO BEAM-COLUMN CONNECTIONS IN FIRE

A thesis submitted for the degree of

Doctor of Philosophy

In the Faculty of Engineering of

The University of Sheffield

by

GUAN QUAN

Department of Civil and Structural Engineering
The University of Sheffield

August, 2016

ACKNOWLEGEMENTS

My special thanks go to Professor Ian Burgess and Dr Shan-Shan Huang for their guidance, inspiration and dedication in supervising me throughout my research project. Their continuous awareness and rich experience made this PhD project nowhere near a lofty mountain, but near a highway. My thanks also go to their financial support on my international conferences, which are great opportunities to present my own work and to communicate with worldwide researchers. The financial support provided by CSC program and by the University of Sheffield is also greatly appreciated.

My thanks also go to my colleagues and friends in the Structural Fire Engineering Research Group for the precious friendship we developed; and to Dr Ruirui Sun for his continuous advice on the development of Vulcan. I would like to express my gratefulness to my family for their love, understanding and sharing during the course of my PhD. Thanks to my boyfriend Dr Jun Ye. We have been together for more than six years from Wuhan University to Zhejiang University in China and to the University of Sheffield in the UK. Thank you for your love, accompany and support. I'm glad that we are going to put an end to our PhD courses as well as our single states together.

DECLARATION

I certify that this thesis submitted for the degree of Doctor of Philosophy is the result of my own research, except where otherwise acknowledged. No portion of the work presented in this thesis has been submitted for another degree or qualification to this, or any other university or institution.

Guan QUAN

(Signature of candidate)

28th August, 2016

ABSTRACT

The investigation of the collapse of “7 World Trade” as part of the events of 11 September 2001 in New York City (Gann, 2008) indicated that connections were among the most vulnerable elements of steel-framed or composite buildings, and their characteristics can determine whether such buildings survive in extreme scenarios such as fire. In this case total collapse of the building was triggered by the fracture of beam-to-column connections caused largely by thermal expansion of long-span beams. This emphasized the importance of investigating the complex mechanisms through which forces are transferred from the adjacent parts of a structure to the connections under fire conditions.

The Cardington fire tests in 1995-96 (Newman, 2000) provided ample evidence that both shear buckling of beam webs and beam bottom-flange buckling, near to the ends of steel beams, are very prevalent under fire conditions. Both of these phenomena could affect the force distribution at the adjacent column-face connection bolt rows, and therefore the sequence of fracture of components. However, there is a distinct lack of practical research investigating the post-buckling behaviour of beams of Classes 1 and 2 sections adjacent to connections at elevated temperatures.

In this PhD thesis, the development of analytical models of pure beam-web shear buckling and a combination of both beam-web shear buckling and bottom-flange buckling of beams of Classes 1 and 2 sections are reported. The analytical models are able to predict the post-buckling behaviour of the beam-end buckling panels in the vicinity of beam-column connections at elevated temperatures. A transition criterion, to distinguish between cases in which pure beam-web shear buckling occurs and those in which the instability is a combination of shear buckling and bottom-flange buckling,

has been proposed, including a calculation procedure to detect the transition length between these two buckling modes. A component-based buckling element has been created and implemented in the three-dimensional structural fire analysis software Vulcan. The influence of the buckling elements on the bolt row force redistribution of the adjacent connections has been investigated in isolated beams and a simple two-span two-floor frame. It is expected that the buckling element will be involved in more complex performance-based frame analysis for design, and that it will be used with an explicit dynamic procedure to simulate local and progressive collapse of whole buildings.

PUBLICATIONS

Journal papers:

1. Quan, G., Huang, S.-S. & Burgess, I.W., 2015. An Analytical Approach to Modelling Shear Panels in Steel Beams at Elevated Temperatures. *Engineering Structures*, 85, 73-82.

2. Quan, G., Huang, S.-S. and Burgess, I.W., 2016. Component-Based Model of Buckling Panels of Steel Beams at Elevated Temperatures. *Journal of Constructional Steel Research*, 118, 91–104.

3. Quan, G., Huang, S.S. and Burgess, I.W., 2016. Parametric Studies on the Component-Based Approach to Modelling Beam Bottom Flange Buckling at Elevated Temperatures. *Acta Polytechnica*,56(2), 132–137.

4. Quan, G., Huang, S.-S. and Burgess, I.W., 2016. The Behaviour and Effects of Beam-End Buckling in Fire using a Component-Based Method. *Acc. Engineering Structures.*

Conference papers:

1. Quan, G., Huang, S.-S. and Burgess, I.W., 2014. Shear Panel Component in the Vicinity of Beam-Column Connections in Fire. Proc. *Structures in Fire Conference*, Shanghai, China, 827-835.

2. Quan, G., Huang, S.-S. and Burgess, I.W., 2014. Shear Panel in the Vicinity of Beam-Column Connections - Component-Based Modelling. Proc*. Eurosteel 2014*, Naples, Italy, 218-225.

3. Quan, G., Huang, S.-S. and Burgess, I.W., 2015. A Parametric Investigation of the Transition Between Beam-Web Shear Buckling and Bottom-Flange Buckling at Elevated Temperatures, Proc*. CONFAB 2015*, Glasgow, UK, 273-278.

4. Quan, G., Huang, S.S. and Burgess, I.W., 2015. A Component-Based Approach to Modelling Beam Bottom Flange Buckling at Elevated Temperatures, Proc. *ASFE 2015*, Dubrovnik, Croatia, 19-24.

5. Quan, G., Huang, S.S. and Burgess, I.W., 2016. Component-Based Element of Beam Local Buckling Adjacent to Connections in Fire. Proc. *Structures in Fire Conference*, Princeton, USA, 352-359.

TABLE OF CONTENTS

LIST OF FIGURES

LIST OF TABLES

LIST OF SYMBOLS

a	distance between plastic hinges along the bottom flange
b	flange width
c	half flange width
d	depth of a beam web
e	Length of an arbitrary tensile strip
$E_{\alpha,\theta}$	young's modulus of steel at elevated temperatures
F	vertical shear force at the end of the buckling zone
F_e	shear resistance of the beam at the end of elasticity
$F_{\max}$	maximum reaction force
$F_{p,S}$	vertical reaction force at the initiation of plastic shear buckling
$F_{p,T}$	vertical reaction force when plastic bending moment resistance is reached
F_u	ultimate shear resistance of the beam
$k_{E,\theta}$	reduction factor for Young's modulus
l	half length of the beam
L	full length of a beam
L_m	full length of a member
M	bending moment at the end of the buckling zone
M_0	plastic bending moment capacity of one flange
M_1	reduced plastic bending moment capacity of one flange
M_p	bending moment resistance of one beam-web compressive strut
P_c	axial force resistance of one beam-web compressive strut
t	heating time
t_f	thickness of the beam flange
t_w	thickness of the beam web
T	temperature of the furnace atmosphere next to the specimen
T_0	ambient temperature
W_{At}	the internal work of tensile strips in Region A
W_{Bt}	the internal work of tensile strips in Region B
W_C	the internal work of the beam web caused by compression
W_e	the external work of the beam
W_f	the internal work of the plastic hinges on the beam flanges
W_T	the internal work of the beam web caused by tension
α	the angle between tensile strips and the deformed upper flange
γ	the angle between diagonal of the shear panel and deformed upper

	flange
δ_e	elongation of an arbitrary tensile strip
δ_{tA}	elongation of the tensile strip in Region A
δ_{tB}	elongation of the tensile strip in Region B
Δ	out-of-plane deflection of one strut
Δ_e	mid-span deflection at the end of elasticity
ΔL_{m}	temperature-induced elongation
Δ_p	mid-span deflection at the initiation of plastic shear buckling
Δ_{rB}	the resultant movement of the right point of the representative strip in Region B
Δ_{rs}	the resultant movement of the right edge of the shear panel
Δ_u	ultimate mid-span deflection
Δ_{vb}	mid-span deflection caused by bending moment
Δ_{vB}	the vertical movement of the right point of the representative strip in Region B
Δ_{vm}	the vertical movement of the mid span caused by shear force
Δ_{vs}	the vertical movement of the right edge of the shear panel
$\varepsilon_{l,\theta}$	limiting strain for yield strength at elevated temperatures
$\varepsilon_{p,\theta}$	strain at the proportional limit at elevated temperatures
ε_t	tensile strain of a tensile strip
$\varepsilon_{u,\theta}$	ultimate strain of steel at elevated temperatures
$\varepsilon_{\mathrm{y},\theta}$	yield strain of steel at elevated temperatures
θ_1	the rotation caused by bottom-flange buckling
θ_2	the rotation caused by shear buckling
θ_a	steel temperature
σ_c	compressive stress in the compressive strips
σ_{cf}	compressive stress in the flange along beam length
σ_{eq}	yield strength of the flange considering reduction caused by axial stresses and shear stresses
σ_{eq1}	yield strength of the flange considering reduction caused by axial stress parallel to yield lines
σ_r	stress normal to the yield lines
σ_t	tensile stress in the tensile strips
σ_{tf}	tensile stress in the flange along beam length
$\sigma_{\mathrm{p},\theta}$	stress at the proportional limit at elevated temperatures
$\sigma_{\mathrm{y},\theta}$	yield strength of steel at elevated temperatures

$\sigma_{yf,\theta}$	yield strength of the flange without considering reduction at elevated temperatures
$\sigma_{yw,\theta}$	yield strength of steel web at elevated temperatures
τ_r	shear force parallel to the yield lines

1.

INTRODUCTION

1.1 BACKGROUND

Steel is one of the most popular construction materials for buildings world-wide. Its high strength-to-weight character enables steel structures to be built using longer spans with smaller foundations, which allow high flexibility in layout for architects. The fast erection sequences make steel construction more time-efficient than competing systems. However, due to the high thermal expansion coefficient of steel, high axial forces will be produced in members of steel structures when they are heated, due to restraint to thermal expansion. Moreover, the strength and stiffness of steel both decrease at a faster rate than those of other structural materials at high temperatures. This emphasizes the necessity to provide additional protection to steel structures against fire.

The main objectives of fire protection are usually fulfilled by applying active and passive measures, either alone or in combination. Active measures include detection, alarms and sprinklers, which come into operation only in the event of fire; whereas passive measures include escape provisions, compartmentation and structural protection, as part of the built system. Structural fire engineers are involved in the specification of passive fire protection to ensure that the structure is designed and constructed such that its stability will be maintained for an appropriate period (CEN, 2005b). For steel-framed structures, the most commonly used form of passive fire protection is to apply a layer of insulating material to provide adequate thermal insulation to steel members. Although this approach has proved adequate, it can be extremely conservative. Also, application of protective materials can be relatively expensive compared with the frame cost, and can affect the appearance of a building. It is preferable that intensive fire protection should only be applied to critical elements.

Therefore, it is very important for fire engineers to further develop their understanding of the behaviour of steel structures when affected by fire, in order to distinguish critical elements, and to promote the efficient use of steel protection in construction.

The establishment of the British Fire Protection Committee (BFPC) at the end of the 20th century initiated a scientific approach to research into structural fire resistance. In the UK, the primary corresponding national standard is *BS 5950-8:1990: Structural use of steelwork in building* (BS, 1990). The more recent CEN 1993-1-2 (CEN, 2005b) and CEN 1994-1-2 (CEN, 2005d), which supersede BS 5950-8, present structural fire design in terms of general concepts, material properties and calculation procedures. However, the current fire design codes (Standard, 1990, CEN, 2005b, CEN, 2005d) were developed from standard fire tests on isolated elements, and these tests ignore the interactions between elements. However, the importance of considering the interactions between elements in structural fire design was revealed in the late 19th century.

Several full-scale fire tests were carried out within a fire research programme conducted on modern multi-storey composite structures built within the BRE large scale test facility at Cardington during 1995-96. The tested structures included an eight-storey steel-framed composite building (Newman *et al.*, 2000) and a seven-storey reinforced concrete building (Bailey and Moore, 2000a, Bailey and Moore, 2000b). The Cardington tests revealed that the performance of a whole building in real fires is much better than that of isolated members in standard fire conditions. This generated an awareness that the interactions between the structural members should be fully taken into consideration in fire-resistant design, since structural performance in fire is controlled by high geometrical and material nonlinearity. The large deflections

caused by the loss of material strength and stiffness can have significant influences on force redistribution, either within isolated members or between adjacent members. Therefore, it is an inevitable trend to adopt the performance-based design approach, by which structures are treated as a whole, to enable the analytical results to be more realistic. In the performance-based analysis, connections were found to be one of the most critical elements affecting the robustness of an entire structure exposed to fire (Burgess, 2007).

Fire research over the last two decades has assumed that connections have sufficient fire resistance compared with the connected members, because they heat more slowly. However, observations from the full-scale fire tests at Cardington (Newman *et al*., 2000), and the collapse of buildings of the World Trade Centre in 2001, raised concerns that joints are potentially the weakest parts of a structure (Burgess, 2007). The investigation of the "7 World Trade" collapse (Gann, 2008) in the aftermath of the collapse of the Twin Towers indicated that the building was unaffected by the aeroplane impacts, but collapsed totally due to the effect of prolonged internal fires. This was triggered by the failure of beam-to-column connections as a result of large thermal expansions of beams. Connection failure may initiate fire spread, or may lead to progressive collapse of a whole building. A number of previous research studies (Burgess, 2010, Burgess *et al.*, 2012, Huang *et al.*, 2013, Al-Jabri *et al.*, 2008, Sun *et al.*, 2015) have shed light on the role of beam-to-column connections in fire, including:

- force-deflection behaviour,
- the influence of connections on the building's survival time,
- connection ductility demand,
- component-based connection models.

The characteristics of connections, especially their ductilities, can influence the robustness of a whole building, and therefore, need to be paid special attention to.

There is a great variation of the definitions of robustness used for technical applications; a robust solution in an optimization problem is the one that has the best performance under its worst case (Kouvelis and Yu, 2013); the robustness in control theory is the degree to which a system is insensitive to effects that are not considered in the design (Slotine and Li, 1991); a procedure can also be said to be robust if the results are stable, convergent and accurate relative to the input (Sun et al., 2012b). In structural engineering, a structure is said to be robust if initial local damage does not extend to a progressive collapse or other damages, which violates the key structure performance (Starossek and Haberland, 2010).

Design methods to ensure a robust structure have been categorized into two types, namely the direct and indirect approaches. Direct robustness design aims at resisting collapse by verifying that the key structure elements meet specified performance objectives subjected to specified hazard scenarios. This can be achieved using an alternative load path, in which the key structural components are able to resist local initial damage. In other words, direct design strongly relies on local structural resistance. On the other side, the indirect design approach focuses on enhancing structural robustness through continuity, redundancy and ductility.

Robustness of structures under extreme loading has been recognized as a desirable property of structures and structural systems since the collapse of the Ronan Point apartment building in 1968. In this incident, a gas explosion on the 18th floor led the entire southeast part of the apartment block to collapse (Pearson and Delatte, 2005). Renewed interest in this topic was generated as a result of the attack on the World Trade Center in New York in 2001 (Gann, 2005), in which simultaneous post-flashover

fires on several adjacent storeys eventually triggered complete collapse. Fire disasters of this kind can induce massive loss of life, severe damages to properties, large economic losses and the disruption of education and public services.

The software Vulcan (Vulcan Solution Ltd, 2015), developed by the Structural Fire Engineering Research Group at the University of Sheffield is a three-dimensional program which allows engineers to conduct three-dimensional structural robustness assessments (Huang *et al*., 1999a). A variety of elements (beam-column (Huang *et al*., 2000), shear connector (Huang *et al*., 1999b) and slab (Huang et al., 2003a)) are implemented in this software. The basic static solver is based on the Newton-Raphson method (Süli and Mayers, 2003). Since the collapse of "7 World Trade" aroused concerns about the fire resistance of connections and progressive collapse of buildings in fire, semi-rigid component-based connection elements and a combination of static and explicit dynamic solvers have been implemented into Vulcan. The software has recently been used to model the progressive collapse in fire of structural frames connected by semi-rigid connections which are modelled using component-based elements.

Component-based models of connection behaviour were first introduced by Tschemmernegg *et al.* (1987) to model the small-rotation behaviour of joints at ambient temperature, and after much development the method is now included in EUROCODE 3-1.8 (CEN, 2005c) as a standard tool to calculate semi-rigid joint stiffness and plastic capacity at ambient temperature. The component-based method considers each connection as an assembly of individual nonlinear springs with predefined force-deformation characteristics. The component-based semi-rigid connection element can represent the real behaviour of semi-rigid connections in terms of force and deflection relationships as well as ductility demand and fracture (Block, 2006, Dong *et al*., 2015)

with very acceptable accuracy. The component-based method offers considerable time savings compared to detailed FE modelling and is considerably more economical than prohibitively expensive fire tests. It is one of the most practical approaches in considering the robustness of connections in frame analysis under fire conditions.

Sun *et al*. (2015) developed a static-dynamic solution procedure for Vulcan. This procedure is able to capture re-stabilization after initial instability has occurred as a result of local failure. For instance, the procedure can be used to track the sequential failure of different connection components during progressive collapse of a whole structure. Sufficient validations (Huang et al., 2000, Najjar and Burgess, 1996) have been carried out to demonstrate that Vulcan is an accurate and computationally-efficient software to be used in performance-based fire engineering design. This has provided later researchers with a convenient platform which can be used as a foundation on which to further develop new elements and to implement these to investigate the collapse in fire of either isolated members or whole structures.

1.2 RESEARCH MOTIVATIONS

The ductility and robustness of connections can influence the survival time of a building; a connection fracture may either be kept within a certain range or be extended to a connection failure, which may trigger complete detachment of the connected members, leading to progressive collapse of the whole building. Since it has been stated that performance-based fire design has been widely accepted as the most realistic design method compared with isolated element design, interactions between adjacent members can have significant effects on the overall structural performance.

The Cardington Fire Tests indicated that combinations of beam-web shear buckling and flange buckling near to connections are very prevalent under fire conditions (Figure 1-1).

Figure 1-1 Flange buckling and beam-web shear buckling in combination (Newman et al., 2000)

This phenomenon can significantly influence the internal forces in the connections. It has been revealed by the author that beam-end buckling reduces the rotational stiffness at the beam-end, which will inevitably decrease the beam-end bending moment. In addition, a steel beam of which a considerable part has buckled can transfer less axial compression force to its end connections before the catenary stage is reached at high temperatures. Local buckling at the beam ends will also have an effect on the deflection of the beam, and therefore will again influence the net tying force within the connection. The increased beam deflection during the heating phase of the fire can significantly increase the tension force on the connection during the cooling period. However, the contribution of the combination of beam-web shear buckling and flange buckling in the vicinity of beam ends has not been taken into consideration by almost any of the existing research. On the one hand, there has been

a lack of theoretical models which can represent the plastic post-buckling behaviour of stocky (Class 1 or 2) sections at elevated temperatures. On the other hand, although detailed modelling using commercial FEA packages, such as ABAQUS or ANSYS, can account for the beam-end buckling phenomenon, this is computationally very demanding, and is not feasible when a global frame analysis is required to enable performance-based structural fire engineering design. Therefore, it has become essential to develop a simplified model which can simulate the beam-end buckling phenomenon sufficiently accurately within an acceptable computing run-time and integrate it into global frame analysis. In this study this has been achieved by developing a new buckling element and integrating it into Vulcan. Based on the existing element types (beam-column, slab, semi-rigid connection, etc) and the development of the static and static-dynamic approaches, Vulcan is capable of considering the influence of the buckling panel adjacent to the beam-column face connections with a full progressive collapse capability if the buckling elements are to be implemented as component-based models.

1.3 SCOPE OF THIS RESEARCH

The objective of this research is to investigate the influence of beam-web shear buckling and bottom-flange buckling at the ends of steel beams on the robustness of the adjacent connections, and to use this to study the inherent robustness of steel-framed buildings in fire. In order to achieve these targets there are five main research activities:

I. To investigate the post-buckling behaviour of beams with Class 1 and 2 sections at elevated temperatures in the aftermath of beam-web shear buckling, based

on the existing “tension field theory” for plate girders. To create an analytical model for the pure shear buckling behaviour.

II. To investigate the post-buckling behaviour after combined beam-web shear buckling and bottom-flange buckling of Class 1 and 2 sections at elevated temperatures, based on Dharma’s (2007) yield-line mechanism. To create an analytical model for the combination of these two buckling phenomena.

III. To provide a transition criterion to distinguish between cases in which pure beam-web shear buckling occurs and those in which the instability is a combination of shear buckling and bottom-flange buckling.

IV. To create a component-based beam-end buckling element, which considers beam-web shear buckling and bottom-flange buckling at the beam end within the beam-end buckling zone. To implement the new element in Vulcan, adjacent to the existing component-based connection element. The component-based model should be able to consider the post-buckling descending force-deflection relationship of the bottom spring, which simulates the bottom-flange buckling behaviour.

V. To perform case studies for both single beams and frames, to investigate the influence of the buckling element on the robustness of adjacent connections and on the survival of steel structures in fire.

2.

LITERATURE REVIEW

In this chapter, existing knowledge on material properties of steel materials and structures in fire, isolated member models, composite slab models, joint models, full-scale frame fire testing and numerical modelling for robustness analysis in fire, shear buckling theory of plate girders, bottom-flange buckling yield line models have been reviewed in sequence. The sequence of descriptions of the 3D structure is from section level to system level, as shown in Figure 2-1.

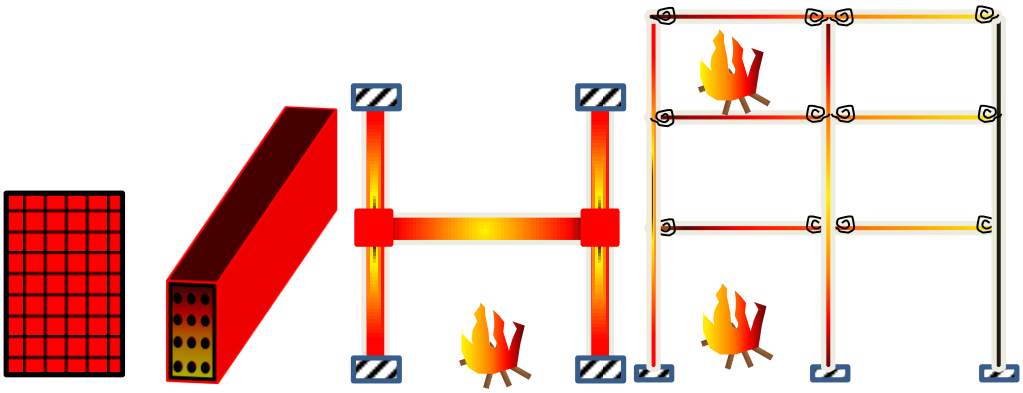

(a) Section Level (b) Component Level (c) Sub-structure Level (d) Frame Level

Figure 2-1 Sequence of descriptions of 3D structure in fire

Relevant research, which is closely related to this study, has been reviewed sequentially. This research includes an introduction to the Vulcan finite element analysis software, shear buckling of plate girders and bottom-flange buckling yield-line models.

2.1 MATERIAL PROPERTIES

The important temperature-dependent material properties of steel involved in structural fire analysis include strain, strength and stiffness. Stiffness and strength reduction occurs in structures subjected to fires. Extremely large internal forces can be produced if thermal expansion of a member is restrained.

The stress-strain relationship for carbon steel at high temperatures defined in EUROCODE 3 (CEN, 2005b) is shown in Figure 2-2. It is defined in EC3 that steel remains linear-elastic before the limit of proportionality $\sigma_{p,\vartheta}$ which reduces progressively from 100°C; the elastic modulus also reduces from 100°C as the temperature rises. The yield stress $\sigma_{y,\vartheta}$, which is defined always to occur at a strain of 2%, initiates a yield stress plateau which may then be enhanced by a strain hardening part for temperatures below 400°C, as shown in Figure 2-2 (a). For temperatures above 400°C, there is a more gradual increase in strength with increasing strain between the proportional limit stress and yield stress, and the yield stress itself progressively reduces with temperature. The yield stress again initiates a stress plateau, as shown in Figure 2-2 (b), but no strain hardening occurs is reached. The limiting strain for the yield plateau 15%, and the strength then falls linearly, vanishing completely at an ultimate strain of 20%. This ultimate strain significantly influence the ductility of steel members; the greater the ultimate strain is, the greater ductility the steel member obtains.

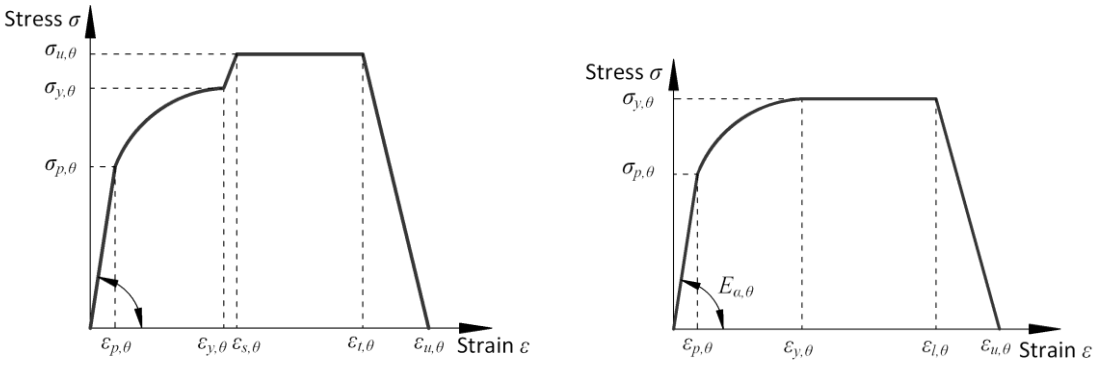

Figure 2-2 Stress-strain relationship for carbon steel at elevated temperatures: (a) below 400°C; (b) above 400°C

The strength reduction factor is defined as the ratio between the steel yield strength at any particular temperature and that at room temperature. The reduction factors for

strength, stiffness and limit of proportionality for low-carbon structural steel at elevated temperatures are shown in Figure 2-3. From this figure it can be seen that yield stress starts to degrade at 400°C. Young's modulus and the proportional limit stress are reduced when the temperature is above 100°C.

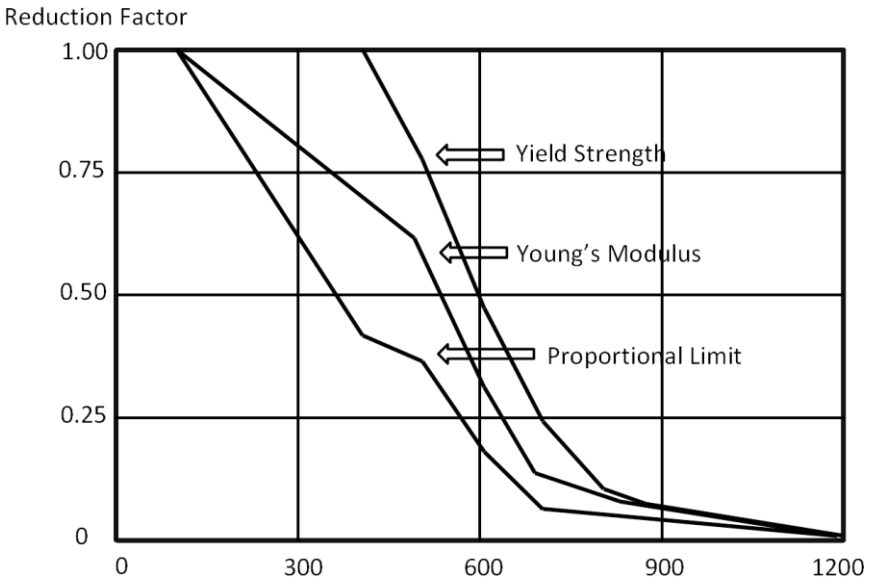

Figure 2-3 Reduction factors for the stiffness and strength of carbon steel at elevated temperatures

The thermal elongation of steel increases with temperature up to about 750ºC, when steel starts to undergo a phase-change in crystal structure. The relative thermal elongation of steel determined in EC3 Part 1.2 can be calculated using the following equations:

for $20°C \le \theta_a \le 750°C$,

$$\Delta L_{\mathrm{m}} / L_{\mathrm{m}} = 1.2\times10^{-5}\theta_a + 0.4\times10^{-8}\theta_a^2 - 2.416\times10^{-4} \quad (2\text{-}1)$$

for $750°C \le \theta_a \le 860°C$,

$$\Delta L_{\mathrm{m}} / L_{\mathrm{m}} = 1.1\times10^{-2} \quad (2\text{-}2)$$

for $860°C \le \theta_a \le 1200°C$,

$$\Delta L_{\mathrm{m}} / L_{\mathrm{m}} = 2\times10^{-5}\theta_a\text{-}6.2\times10^{-3} \quad (2\text{-}3)$$

The thermal elongation can play a negative role on the tensile resistance of steel members. Taking a connection bolt-row that fractures in tension as an example: the ultimate (fracture) strain is fixed for a bolt and the total strain in the bolt is the summation of the strain due to thermal elongation and that due to tensile stress. Once the bolt elongates due to thermal expansion, there will be a reduced deformability left to cope with the elongation due to tensile stress, and so the total strain can reach the ultimate strain, resulting in fracture, at a lower tensile stress level.

At high temperatures, a member can experience different temperatures distributions at different locations, depending on their distances from fire source and the relative massivity of different parts of the cross-section. In order to allow for the different thermal strains and material properties which accompany different temperature distributions across member cross-sections, the cross-section of a member can be divided into a matrix of segments (Najjar and Burgess, 1996). Each segment can have its own temperature, thermal and mechanical strains, and temperature-dependent material properties at each analytical stage. In this way rather complex nonlinear structural behaviour, such as thermal expansion and material degradation at elevated temperatures can be taken into account in the segmented cross-section, as shown in Figure 2-1 (a).

2.2 FIRE RESISTANCE DESIGN METHODS

The concept of structural fire engineering design has experienced two main stages: isolated member design based on furnace testing using the standard fire curve, and performance-based structural fire design.

The Standard Fire curve was first standardized in 1932 (Malhotra, 1980), in the form expressed using the following equation:

$$T = T_0 + 345\log(0.133t + 1) \quad (2\text{-}4)$$

The structural member fire resistance defined in the current design guides BS 476 (1987), BS 5950 (1990), EC3 (2005c) and EC4 (2005e) are based on the standard fire testing of isolated members, in which a loaded single member is heated in a furnace according to ISO834 Standard Fire (1975) exposure. Standard fire testing has been used to assess the behaviour of walls, floors, columns and beams. There are three possible failure criteria for structures in fire; Resistance failure (which applies to all member types), Insulation and Integrity failure (which apply only to separating elements such as walls and floors). For resistance failure of a beam the criterion is that the maximum deflection reaches a prescribed limit, such as (span/30) or (span/20); the fire resistance rating of the member is the time of standard fire exposure at which the failure criterion is reached.

In the UK, the Yellow Book (ASFP, 2010) provides a guide to passive structural fire protection on the basis of fire test data, in accordance with BS 476. In the first and second editions of this publication, the thickness of fire protection was specified such that the maximum temperatures of 550°C for columns, and 620°C for beams (supporting concrete floors), were not exceeded for a given period of fire resistance. The time at which the appropriate one of these member temperatures occurs under the Standard Fire Curve is the member fire resistance. Since the third edition, the limiting temperatures of 550°C and 620°C have been recommended for general use, although more detailed critical temperatures, taking account of different load ratios, building types and exposure conditions, have been considered. For each fire protection

system, the effect of a specified thickness of fire protection on the heating rate is simply measured by a parameter called the “section factor”. The section factor is the ratio of the exposed surface area per unit length to the volume of the member within this length. For various member types and fire protection materials, fire resistance periods and section factors can be calculated, and therefore appropriate fire protection material thicknesses can be found in the Yellow Book.

The standard fire resistance test is often criticized as not representing a real fire scenario. This suspicion came from the fact that buildings can be affected by severe fire scenarios, in which member temperatures are far above the critical temperatures defined in the design codes. In the late 20th century, a series of full-scale fire tests were carried out at Cardington, UK. In these tests it was found that a composite building survived in severe natural fire scenarios, even when many beams were unprotected. These fire tests revealed that the standard fire test can be very conservative, because it ignores any interaction between members, although this interaction may not always be advantageous. Therefore, performance-based design, which fully considers the likely fire behaviour, heat transfer to the structure and the structural response including member interactions, has become more popular in structural fire design.

2.3 RESEARCH INSPIRED BY CARDINGTON FIRE TESTS

2.3.1 The Cardington Fire Tests

A fire research programme on a modern multi-storey composite steel framed structure built within the BRE large scale test facility at Cardington (O'Connor and Martin, 1998) was carried out by British Steel’s Swinden Technology Centre, co-sponsored by the European Coal and Steel Community (ECSC) with TNO (The Netherlands) and CTICM

(France) as partners, between 1995 and 1997. This research programme aimed to understand the results of the large-scale fire tests at Cardington in order to develop rational design guidance for composite steel frameworks at the fire limit state. Six major fire tests were carried out during 1995-96 on different parts of the frame. They were: a restrained beam test, a plane frame test, two corner compartment tests, a large compartment test and an office fire (demonstration) test. In the first and second of these tests, particular elements of interest were heated by gas fires. In all the other tests, wooden cribs were ignited in the compartments in order to model natural fires. In one case a ventilation shutter was used to control the compartment temperature. For the final test of this series, a fire in a simulated office environment was created in order to subject the structure to a fire which could be related to a real scenario (Usmani *et al*., 2000).

Another large-scale fire test at Cardington was carried out on the same steel–concrete composite framed building in 2003 (Wald *et al*., 2006). The test took place as a result of a collaborative research project between Czech Technical University (Czech Republic), University of Coimbra (Portugal), Slovak Technical University (Slovak Republic) and Building Research Establishment (United Kingdom). The test was carried out as part of a European collaborative research project: Tensile membrane action and robustness of structural steel joints under natural fire. The project concentrated on the investigation of the structural integrity of a compartment subjected to natural fire conditions. The test results are reported by Lennon and Moore (2004).

Two of the main observations from the Cardington fire tests were that the steel beams did not “run away” as predicted by furnace fire tests, and the composite slabs did not collapse. In order to reveal the reasons for these phenomena, experimental and numerical studies were conducted on steel beams and composite slabs, considering

their beam-end restraint and slab-edge support. Theories of catenary action for steel beams and tensile membrane action for composite slabs became the main explanations of what actually occurs in beams and slabs subjected to large deflection at high temperatures.

2.3.2 Steel beam and concrete slab research inspired by the Cardington Fire Tests

Liu *et al*. (2002) conducted restrained steel beam fire tests in the Fire Laboratory at Manchester. In these experiments, small-section I-beams were supported between two columns in a "rugby-post" arrangement. In some tests additional horizontal restraint stiffnesses were applied to the ends of the beams to simulate the restraining effect from surrounding structure. The behaviour was studied under different beam load ratios.

Yin and Wang (2004, 2005) developed methods to describe the catenary action of steel beams at elevated temperatures both theoretically and numerically. In traditional isolated beam analysis, only the flexural capacities were checked, without considering any axial restraint at the beams ends. The beams were predicted to "run away" when the applied load exceeded the beam's bending moment capacity. However, it has been proved that beams can experience catenary action when the temperature is above their limiting temperatures, which are governed by their bending resistance provided that enough axial restraint has been provided. Therefore, a beam's loading-carrying system progressively becomes catenary action, experiencing increasing tension force. Eventually the vertical components of this tension force, along the highly-deflected beam, are responsible for balancing the vertical external load. Consideration of catenary action in design can reduce construction cost by saving fire protection to

steel beams, as they will not collapse unless the beam-end axial restraints are not strong enough.

Tan and Huang (2005) applied FE modelling to investigate the structural response of steel beams with axial restraint in fire. The behaviour of both pin-ended and semi-rigid restrained beams was investigated. The dominant factors considered included thermal gradient, load utilization factor, beam slenderness ratio and axial restraint ratio. Their analysis demonstrated that axial restraints provide beams with axial tying capacity, which enables these beams to experience catenary action instead of collapse at high temperatures.

Li and Guo (2008) conducted experiments on two restrained steel beams exposed to fire during both the heating and cooling phases. Obvious catenary action was observed during these experiments.

In all the elevated-temperature steel beam tests mentioned above, sufficient axial restraint was provided so that catenary action of steel beams could occur. However, in real structures, such a level of axial restraint can only exist if the beam-to-column connections are of sufficient strength and ductility. The buckling at the beam ends, frequently seen from the Cardington Fire Tests, on the one hand, can change the force distribution between the connection bolt rows. Therefore, the design bolt-row forces can reach their strengths and ultimate strain at a different temperature level. The buckling elements can influence the fracture temperature the bolt rows of their adjacent connection. On the other hand, the buckling element can also change the surviving temperature of the beam when no sufficient axial restraint from the connection can be provided. This inspires the research reported in this thesis.

Another main breakthrough from the Cardington Fire Tests was the Tensile Membrane Action of concrete slabs.

Huang *et al*. (2000) presented a three-dimensional, nonlinear finite-element procedure for modelling composite and steel-framed building behaviour in fire. He also reported theoretical and numerical research to predict the response of reinforced concrete slabs subjected to fire (2003a, 2003b). This procedure was based on thick plate theory. The influences of different thermal expansion characteristics, differential temperature distributions through the slab thickness and tensile membrane action were investigated. It was shown that the proposed model could properly simulate membrane action of concrete slabs in fire.

Bailey *et al.* (2000a, 2004) proposed a tensile membrane action method for designing composite slabs at elevated temperatures. Burgess *et al*. (2014, 2016) presented an initial re-examination of the mechanisms of tensile membrane action of thin concrete floor slabs, attempting to remove the arbitrary assumptions from Bailey's TMA method, and to analyse the slab's developing deflections kinematically.

2.4 FRAME NUMERICAL MODELLING

Numerical Modelling and theoretical investigation

Saab and Nethercot (1991) presented a formulation for the bilinear analysis of two-dimensional steel frames under fire conditions. This was one of the initial attempts to carry out numerical frame analysis in fire. Their work was capable of considering the effects of geometric nonlinearity, temperature-dependent nonlinear material behaviour and temperature distributions through each member.

Najjar and Burgess (1996) described the principles of a three-dimensional frame analysis for fire conditions using a program which was at that time named 3DFIRE, which aimed at modelling the behaviour of skeletal frames under fire conditions. The program was based on an existing two-dimensional program INSTAF which had been

written for nonlinear 'spread of yield' analysis of two-dimensional rigid steel frameworks at ambient temperature. High material nonlinearities could be taken into account by this program. Temperature distributions, which could induce differential thermal expansion, could be adopted. Various test cases correlated well with previous independent analytical studies. However, the program did not include composite action, plate elements or semi-rigid connections.

Rotter *et al*. (1999) discussed the response of a structural element under fire conditions within a large, highly redundant, building. Aspects such as thermal expansion, the relative stiffnesses of adjacent parts of the structure, material strength degradation, development of large deflections, buckling and temperature gradients were illustrated with simple examples. The significance of these findings for the design of large buildings was briefly investigated and explained.

Usmani *et al*. (2001) attempted to illustrate some of the most important and fundamental principles that dominate the behaviour of composite-framed structures in fire. The descriptions were developed in the context of numerical modelling of the full-scale Cardington fire tests. Fundamental principles, concerning the evolution of internal forces and displacements in real structures with acceptable simplifications, were presented in this work.

Liew *et al*. (2004) developed a numerical approach for inelastic transient analysis of steel-framed structures subjected to explosive loading followed by fire. This approach enabled realistic overall frame modelling by adopting the use of beam-column elements utilizing fibre cross-section representations. Verification examples indicated that the proposed analysis could be effectively used to solve structural explosion and thermal response problems. However, their work was limited to two-dimensional frames, and could not avoid singularity at the onset of local buckling.

Lien *et al*. (2010) used the Vector Formed Intrinsic Finite Element (VFIFE) method to carry out structural analysis in fire. This method is based on Newton's Laws of Motion, and discretizes the structural system into particles. Large deformation and catenary action of structures can be well simulated without forming a structural stiffness matrix. This is an alternative way of avoiding the singularity problem when local structural failure occurs.

Franssen *et al*. developed a computer program known as SAFIR (2011). This software has been used by many researchers. For instance, Junior and Creus (2007) extended the "plastic hinge concept" into fire analysis. They developed an alternative simplified procedure to analyse the behaviour of three-dimensional frames under elevated temperatures. The model was compared with results from SAFIR and experimental results, and was shown to be accurate, with low computational cost.

Sun *et al*. (2012b) developed a static-dynamic procedure and extended it within the Vulcan software to model the behaviour of steel-framed buildings during both local and global progressive collapse under fire conditions. An explicit integration method was adopted in the dynamic part of this procedure, in order to make the analysis continue beyond local, temporary instabilities. This procedure enables the modelling to automatically switch between static and dynamic analysis, which allows Vulcan to investigate initial stable behaviour, local failure, restabilization and progressive collapse of buildings. The work has subsequently been extended (Sun *et al*., 2012a, Sun *et al*., 2015).

It has been found that the research on frame behaviour in fire has been extended from two-dimensional to three-dimensional, intending to consider more and more realistic interactions between the structural elements of a frame. Carrying out performance-based fire design through FEA frame analysis is an obvious solution. However, its

extremely high computational cost makes it impractical, given that each connection consists of many different components and a frame contains many connections. Therefore, a practical and accurate enough alternative method, which is to use component-based method to model the connections, is adopted.

2.5 PROGRESSIVE COLLAPSE OF WTC7 BUILDING

On September 11th 2001, the twin towers of the World Trade Centre in New York were attacked (McAllister and Corley, 2002) by terrorists with hijacked jet airliners. One of the aircraft was flown into the face of the North Tower (WTC1), and the other crashed into the South Tower (WTC2). Later, at 5:21 p.m. on the same day, WTC building 7 collapsed because of fires which had started as a result of the collapse of WTC 1. The progressive collapse of WTC 7 is of significant interest, as the collapse was triggered by the failure of beam-to-column connections under fire conditions rather than by impact damage from the collapsing towers.

The floor plan of Floors 12-14 of WTC 7 is shown in Figure 2-4. Particular attention was paid (NIST, 2008) to the connection of a non-composite primary beam to Column 79. The primary beam (44/79) supported several protected composite secondary beams with long spans, on only one side. During the fire these fully protected secondary beams were heated to between 500°C and 600°C, which would have produced approximately 100mm of free thermal expansion. In order to restrain the secondary beams, large horizontal shear resistance needs to be provided by the column-face connection of the primary beam. However, the connection was only designed to resist gravity load. The locating bolts at this connection were easily fractured, as they had little horizontal shear resistance. The primary beam was separated from Column 79 soon after the shear resistance of the connection was reached. This separation

sequentially happened on adjacent lower floors as their loads were progressively increased by debris from upper floors. Collapse then progressed from east-to-west across the core, ultimately overloading the perimeter columns and causing the entire superstructure to fall downward as a single unit. The progressive collapse of WTC7 indicated that connection failure can initiate the collapse of the connected beams, and can cause accumulation of gravity loads, together with sequential impacts from the fallen beams and slabs, onto the lower-storey columns. The buckling of the columns under increased load and with longer effective lengths may cause progressive collapse of the whole building. Therefore, it is reasonable to investigate the robustness, fracture sequences and survival times of semi-rigid connections in fire.

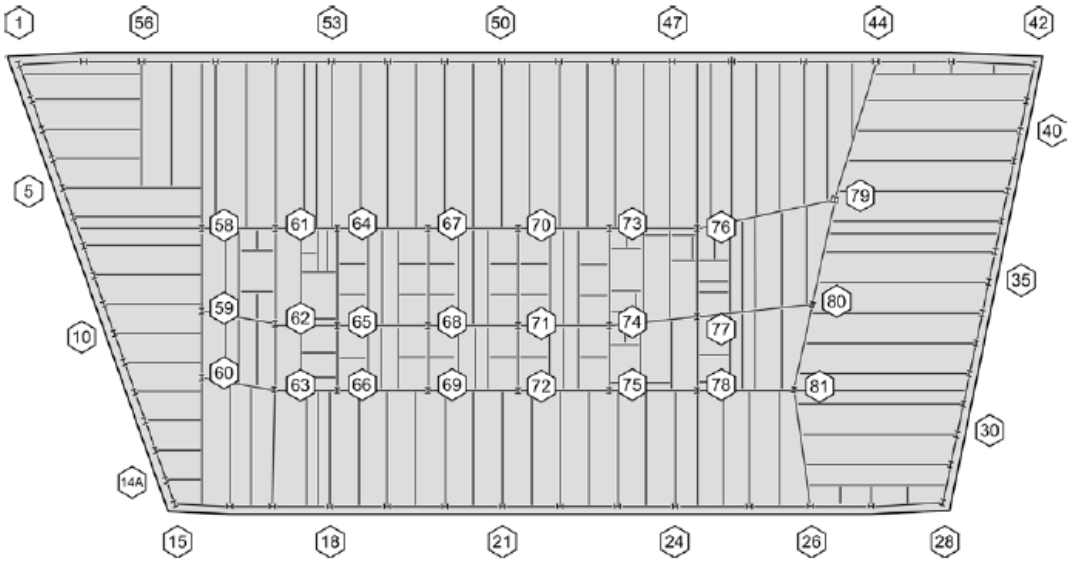

Figure 2-4 Typical floor plan (NIST, 2008)

2.6 JOINT MODELS

As has been stated, the collapse of the WTC buildings emphasized that connections are among the weakest components of structural frames in fire conditions. The connections are subjected to complex combinations of moment, axial and shear forces

transferred from adjacent beams and slabs under fire conditions. If the joint is with sufficient strength and ductility, the joint is able to provide sufficient axial restraint to the beam. In this case, the steel beam can experience catenary tension at high temperatures and dramatically increases the survival temperature of the beam. On the other side, a joint with insufficient strength and ductility may suffer from a fracture, which leads to an additional load onto the lower floor when the steel beam falls. This may trigger a 'pancake' effect and finally lead to the progressive collapse of the whole building. That is why when investigateng steel beams with brittle connections, the beam survival temperature is always assumed to be the temperature, at which the net tying force in the connection turns from compression to tension (when catenary action initiates).

In traditional analysis, joints are assumed to be either 'pinned' or 'rigid', 'pinned' joints have almost no rotational stiffness while 'rigid' joints are of infinite rotational stiffness, without any relative rotation between beams and columns. Nevertheless, the majority of practical joints are semi-rigid. This is mainly because components, each with a finite flexibility, tend to be connected in series, forming even more flexible assemblies.

Al-Jabri (2011) presented an overview of numerical modelling and simulation methods to summarise the behaviour of beam-column joints at elevated temperatures. He classified these models as finite element models, curve-fit models, component-based models, and artificial neural network models. However, in assessment of the robustness of composite structures in fire, a stable, simple and reasonably accurate model is sufficient to model the overall behaviour. A mature way is to develop component-based models, which are capable of predicting the behaviour of semi-rigid beam-column connections, and to incorporate them into global structural analysis programs.

Anderson and Najafi (1994) reported the results of five ambient-temperature tests on composite beam-to-column connections, and six bare-steel connections of the same type. Parameters such as the quantity of reinforcement and the depth of the steel section, which are both related to the moment capacity and stiffness of composite connections, were investigated. A simple spring model was proposed to predict a bilinear approximation of the moment-rotation relationship of these connections.

Da Silva *et al*. (2001) described a type of component-based model for the behaviour of semi-rigid steel joints. These mechanical models consist of extensional springs and rigid links. The springs exhibit a bi-linear force-deformation characteristic. This model was used to model a cruciform steel flush end-plate beam-to-column joint experiment. The analytical procedure produced by da Silva is able to predict the moment-rotation relationships of semi-rigid steel connections under fire conditions.

A large number of tests were conducted by Spyrou *et al*. (2004a, 2004b) to investigate the behaviour of the tension and compression zones of semi-rigid connection components at high temperatures. He further developed component-based force-displacement models for the tension and compression zones of connection elements. These models were combined to represent the behaviour of a whole component-based connection element at elevated temperatures.

Al-Jabri *et al*. (2005) conducted five series of tests to investigate the rotational behaviour of semi-rigid joints at elevated temperatures. Moment-rotation curves were derived at different high temperatures. His tests offered more fundamental experimental data for later researchers to compare with.

Block *et al*. (2007) further developed the component model for endplate connections, based on the earlier work by Spyrou. In his work, the joint model was assembled from components representing bolts in tension, the column web in compression, the

endplate in bending and the column flanges in bending. A shear spring was included to transfer the vertical shear force between the two nodes of the connection element. However, this shear spring was assumed to be rigid.

Yu *et al*. (2009a) divided semi-rigid endplate connection components into T-stub models. An optimum yield-line model was developed, based on the plastic work-balance principle, to capture the behaviour of endplate connections at large deformations up to failure. The model was validated against experiments at both ambient and elevated temperatures. A number of validation studies were carried out comparing finite element analysis with the analytical model, which indicated that the analytical model was able to represent the behaviour of endplate connections well at both ambient and high temperatures. She then developed a component-based model (Yu *et al*., 2009b, 2009c) to model the behaviour of web cleat joints at elevated temperatures subjected to tying forces. In this model, the effect of opening of the angles was considered as forming a four-plastic-hinge mechanism. The model was again validated against FEM and both ambient- and high-temperature tests.

In order to investigate the relative robustness of different types of steel joints in steel-framed structures in fire, Wang *et al*. (2011) carried out ten fire tests on medium-scale partially-restrained steel “rugby goalpost” frames with five different types of joint, including web cleat, fin plate, flexible endplate, flush endplate and extended endplate connections. Their structural fire response, including joint failure modes, the development of beam mid-span deflections and axial forces in the joints at high temperatures were investigated.

Hantouche *et al*. (2016) conducted studies to investigate the main parameters that affect the behaviour of web cleat connections in fire. The characteristics and behaviour of these connection types were compared at high temperatures. This study helped to

extend the understanding of the factors controlling the deformation capacity and strength of web cleat connections in fire.

The robustness of beam connections in the direct vicinity of the column face is vitally significant to the fire resistance of steel-framed/composite buildings. In recent years, a large number of experiments have been conducted to investigate the behaviour of steel connections at elevated temperatures, in order to validate the proposed component-based models. Numerical simulation is also a good way to conduct parametric studies. Since realistic tests may be costly in both time and money, robust numerical simulations have been the preferred tool of many researchers. Beam-web shear buckling and bottom-flange buckling near to the ends of beams have been consistently observed in the full-scale fire tests at Cardington and in the aftermath of accidental fires. These phenomena may have effects on the stress distribution of the adjacent column-face connection bolt rows, as well as the survival temperature of the connected beam when beam-end connections of insufficient ductilities have been used. Therefore, it is important to include these buckling phenomena in structural fire analysis.

2.7 SHEAR BUCKLING OF PLATE GIRDERS

As early as 1886, the possibility of utilizing the post-buckling strength of plate in bridges was considered by Wilson (1886). Later Wagner (1931) presented a diagonal tension theory concerning buckling and post-buckling behaviour for aircraft structures in 1931. However, the post-buckling behaviour of beam web panels was not considered as a design concept until the 1960s; until this time the elastic buckling load was used as the only design limit criterion. In the 1960s, Basler *et al.* (1960, 1961a, 1961b) presented a method of calculating the ambient-temperature post-buckling

capacity of the webs of plate girders subject to shear; this work was later used as the basis of a design method (ASIC, 1963) introduced by the American Institute of Steel Construction (AISC). However, in this theory, the flanges of plate girders were assumed to be too flexible to carry significant bending moments, which led to conservative results. Subsequently, Fujii (1968) presented a modification of Basler's theory, considering the contribution of flanges to the total post-buckling load capacity. In the 1970s, Rockey *et al.* (1968, 1972, 1978, 1987) presented a systematic study of, and a design method for, plate girders subject both to pure shear and to combined shear and bending. Their theory further improved Basler's theory by considering the strength of flanges. The theories above are all classified as 'tension field theory' or its derivatives, because the fundamental assumption is that, after elastic buckling, any additional load is carried by a tensile membrane field. Tension field theory only deals with web panels with aspect ratios less than 3 (Galambos, 1998). Hereafter, the term 'aspect ratio' refers to the ratio of the distance between adjacent transverse stiffeners to the depth of the web panel. The theory was later shown, by Lee and Yoo (2008), to be able to predict well the post-buckling strength under pure shear of panels of aspect ratios smaller than 1.5, but to lose accuracy for higher aspect ratios. This indicates that tension field theory should only be used to represent plate girders with transverse stiffeners. Lee and Yoo (1998, 2006, 2008) carried out a series of finite element studies to investigate the post-buckling behaviour. They modified the existing formulations to decrease the discrepancy between tension field theory and their finite element modelling. They also proposed empirical amendments to classical tension field theory for web panels with aspect ratios higher than 3. Vimonsatit *et al.* (2007a, 2007b) extended the classical ambient-temperature tension field model for plate girders, to account for elevated-temperature behaviour, by changing material properties and

incorporating the effect of compressive forces due to axial restraint. However, the "tension field theory" developed for plate girders can not be directly used for the analysis of the beam-web shear buckling of Class 1 and 2 sections. This is because that the beam-web shear buckling length of a plate girder is predefined by the distance between two adjacent stiffeners, which do not exist for most Class 1 and 2 sections. Therefore, the shear buckling lengths of Class 1 and 2 sections have to be calculated. Moreover, as the webs of plate girders are very thin (usually classified as Class 4 sections), buckling would usually occur in the linear-elastic phase, whereas, for the Class 1 and 2 sections, nonlinear buckling will often occur. Therefore, the tension field theory needs to be revised to model the beam-web shear buckling of Class 1 and 2 sections, as described in Chapter 3.

2.8 BOTTOM-FLANGE BUCKLING YIELD LINE MODELS

A body of research has been carried out to investigate the local in-plane flange buckling phenomenon, including both the pre- and post-buckling stages. Recent research has a common solution for the pre-buckling stage, while different collapse models of the post-buckling stage have been proposed since 1965. The evolution mainly focused on the attempts to transform the yield line mechanism from experimental observation to analytical and numerical models. In all the assuming yield-line mechanisms, the buckling zone consisted of plastic zone and yield lines. The calculations were all based on the energy principles. There were two basic types of yield line models, which were symmetric collapse plastic mechanism and asymmetrical collapse mechanism.

Climenhaga and Johnson (1972) presented an approximate method to predict the moment-rotation relationship of an I-shape beam when local flange buckling was

developed. In their theory, the collapse model was perfectly symmetric, and the length of the flange plastic zone equals to the flange width. Comparisons between the theoretical predictions and several test curves showed consistently conservative, but reasonable agreement.

Kuhlmann's model (1986) was on the basis that there were only yield lines at the buckled flange. There assumed to be a plastic zone, which can be squashed, and several yield lines at the beam web. However, Kuhlmann's model is performing unreasonable in terms of deformation compatibility since if there was any squash within the beam-web plastic zone, the buckled flange couldn't be squashed as there was no relevant plastic zone on the flange.

The mechanisms mentioned above are symmetric collapse plastic mechanisms.

The most recent developed yield line mechanisms consist in a more suitable buckling shape for the beam flange and web.

A more careful examination of experimental results observed that the width of the web plastic zone is different from the flange width. Gioncu and Petcu (1997) improved the length of the yield-line mechanism by carrying out experimental observation and numerical modelling. A most recent yield line mechanism was reported by Gioncu and Mazzolani (2003). The parameters defining the shape of the mechanism, apart from its length, were determined based on the principle of the minimum of the total potential energy.

All the yield line mechanisms mentioned above are suitable for ambient-temperature analysis. A summary of the yield line mechanisms is shown in Table 2-1.

Table 2-1 Collapse yield line mechanisms in the post-buckling stage

Author(s)	Flange	Web
Climenhaga and Johnson (1972)	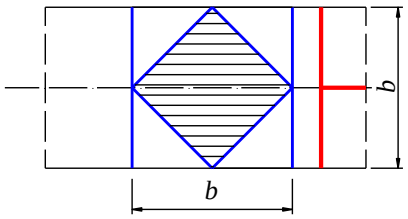	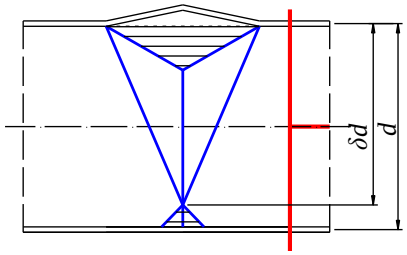
Kuhlmann (1986)	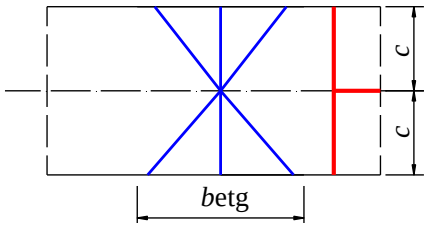	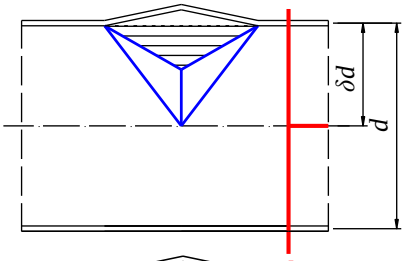
Gioneu and Petcu (1997)	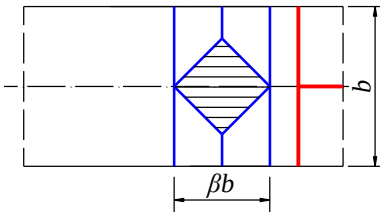	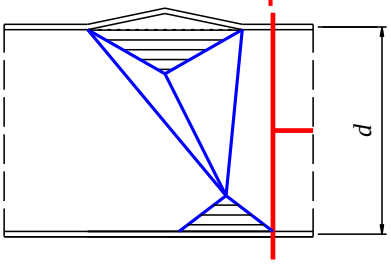
Gioncu and Mazzolani (2003)	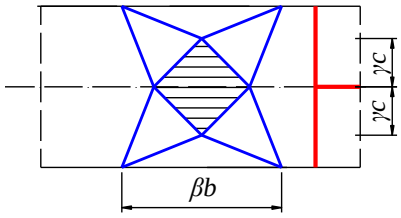	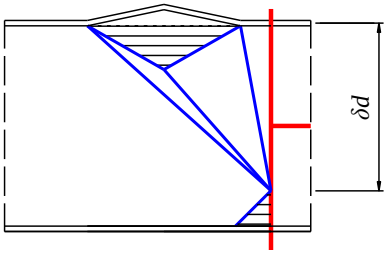

Dharma extended the most up-to-date ambient temperature model, proposed by Gioncu and Petcu, to elevated-temperature applications for both steel beams (Dharma and Tan, 2007b) and composite beams (Dharma and Tan, 2008) by introducing reduction factors to the flange buckling wavelengths to account for temperature-dependent material properties. In Dharma's research, the buckling wavelength is based on elastic plate buckling theory (Timoshenko and Gere, 2009), in which the beam web acts as a rotational spring providing rotational restraint to the flange.

However, this assumption tends to over-estimate the flange wavelength when the beam web is relatively thin (but may still be classified as Class 1 or 2 according to EC3 Part 1.1 (CEN, 2005a). The results derived from Dharma's research have been shown to be extremely conservative for thin-web beams at elevated temperatures (Dharma, 2007). Moreover, Dharma's model considers the beam-web buckling as a passive movement, which is caused by the rotation of the web-flange intersection when flange buckling occurs; and so the beam-web buckling wave is vertical rather than diagonal (what the shear buckling wave should be, as observed in the majority of images from the Cardington Tests). The beam-web shear buckling is likely to be independent of flange buckling, and is triggered at least in part by shear force. The occurrence of shear buckling depends on various factors, such as the relative slenderness of the beam web and flanges and the ratio between the shear force and bending moment at the beam ends. Therefore, Dharma's model is not suitable to be further utilised, such as to be converted to a component-based model, before relative corrections have been made.

2.9 CONCLUSION

As the connection is one of the most critical components in a structure under fire conditions, and the existence of the beam-end buckling phenomenon can influence the survival time of the connection, it is important to involve the beam-end buckling behaviour in structural fire analysis. It has been presented that the most updated Dharma's model tends to over-estimate the resistance of the buckling element when the beam web is relatively thin. Therefore, it is necessary that a new analytical model is created based on Dharma's model to fully consider the interaction and independency between the beam-web shear buckling and bottom-flange buckling, and

to provide good accuracy of results in all the beam-web slenderness ranges for the Class 1 and 2 beams.

3.

AN ANALYTICAL APPROACH TO MODELLING SHEAR PANELS IN THE POST-BUCKLING STAGE AT ELEVATED TEMPERATURES

3.1 INTRODUCTION

Since no practical research has been done on the post-local-buckling behaviour of beams of Class 1 and 2 sections at either ambient or elevated temperatures so far, the analytical model is based on the classic “tension field theory” of plate girders. This has been adapted to the structural response of Class 1 and 2 sections, which can form a plastic hinge with the rotation capacity required by plastic analysis, without reduction of its resistance according to Eurocode 3 Part 1-1 (CEN, 2005a). A brief review of the development of tension field theory has been presented in Chapter 2.

3.2 DEVELOPMENT OF ANALYTICAL MODEL

Classical tension field theory can represent the post-buckling behaviour of plate girders very well (Basler *et al*., 1960, Basler, 1961a, Basler, 1961b, Rockey and Skaloud, 1968, Rockey and Skaloud, 1972, Rockey *et al*., 1978, Porter *et al*., 1987). In these models, shear resistance involves three stages: pre-buckling, post-buckling and collapse. In the pre-buckling stage, no buckling appears in the panel, and the principal tensile and compressive stresses are identical until elastic buckling happens. The elastic buckling strengths of plates under various conditions are given by Timoshenko (1961). In the post-buckling stage, stress redistribution occurs, with increase occurring especially in the directions of the tensile principal stresses. Any additional compressive stress produced after the elastic stage, can effectively be neglected after web shear buckling. In the collapse stage, four plastic hinges appear on the flanges, and finally the plate girder fails in a “sway” mechanism. In the proposed analytical model, for Class 1 sections, the shear response once again consists of three stages, which differ from those of tension field theory. These are the elastic, plastic and plastic post-buckling

stages. The behaviour of the web panel of a Class 1 section subject to shear and bending moment is compared with that of a plate girder in Figure 3-1.

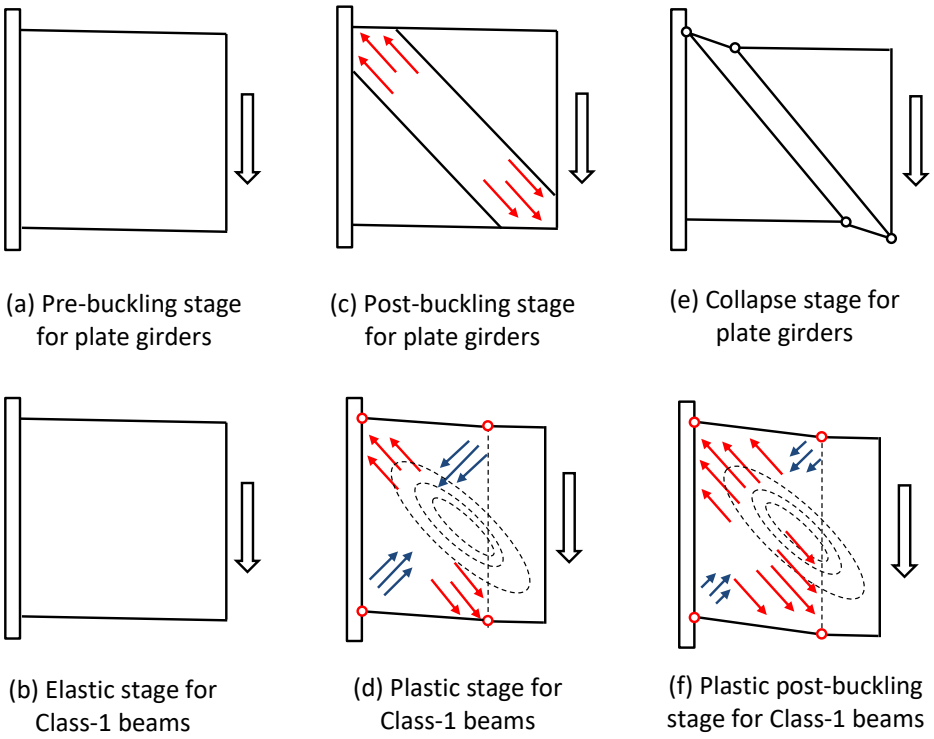

Figure 3-1 Comparisons of web panel behaviour for plate girders and Beams of Class 1 and 2 sections under shear and bending

The aim of the proposed model is to produce a tri-linear force-displacement relationship for any shear panel, from initial loading to failure. An example characteristic is shown schematically in Figure 3-2.

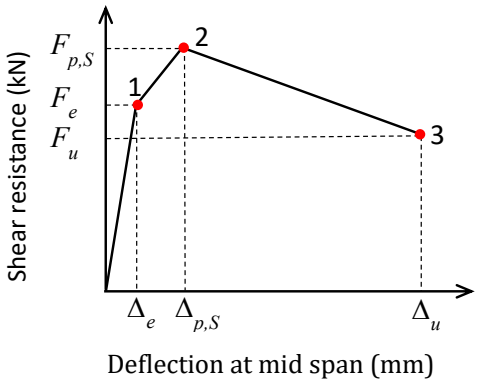

Figure 3-2 Schematic tri-linear force-deflection curve of a shear panel

In this figure, Point 1 illustrates the end of the pre-buckling elastic stage. In the elastic stage, it is assumed that no buckling appears in the panel, and the principal tensile and compressive stresses are identical. The beam-end reaction force is calculated on the basis of the design elastic shear resistance according to Eurocode 3 Part 1-1 (CEN, 2005a). Up to Point 1, the mid-span vertical deflection of a beam is assumed to be induced by both bending and shear. Therefore, Eurocode 3 can be used to calculate the shear resistance and deflection at this point. Point 2 refers to the initiation of buckling, and Point 3 represents failure. The failure here is only a defined point to put an end to the force-deflection curve of the analytical model with a strain too large to be reached by beams in a real fire scenario; it does not necessarily represent a real failure. In the analytical model, the strain 0.15, which is the end of plateau in the material stress-strain characteristic according to Eurocode 3 (CEN, 2005b), has been used in the calculation of Point 3. As the object of the study is beam-web shear buckling, for all the beams analysed, resistance to shear is more critical than to bending moment. Therefore, the resistances below all refer to shear resistance. Bending moment is assumed to be solely resisted by the top and bottom flanges. The shear resistance and the mid-span vertical deflections at Points 2 and 3 are to be evaluated by the proposed analytical model.

In the calculation procedure, several assumptions have been made for the post-buckling phase.

(1) The four edges of the shear panel are assumed to be rigid.

(2) The panel is composed of tensile strips aligned at 45^{o} to the horizontal ($\alpha+\vartheta_2$) and compressive strips perpendicular to these tensile strips (see Figure 3-1 (f)).

α is the angle between the tensile strip and the upper edge of the shear panel while ϑ_2 is the angle between the upper edge of the shear panel to horizontal. The stresses within all the tensile strips are identical, as are the stresses within all the compressive strips.

(3) The bending moment of the buckling panel is only resisted by compressing or stretching the top and bottom flanges. There is no bending deformation on the beam web.

The stress-strain relationship for structural steel at high temperatures is based on Eurocode 3 Part 1-2 (CEN, 2005b) , for which the model is shown in Figure 3-3 (b); however the curvilinear inelastic development phase of the Eurocode curve is replaced by a sharp transition from elasticity to plasticity, as only the two end points of the sharp transition (corresponding to proportional limit state and the initiation of yield state) have been used in the analytical model; the path in between these two points does not affect the result of the key points in the analytical model. The reduction factors for yield strength and Young's modulus at high temperatures from this code have been used in the analytical model. At ambient temperature, the stress-strain relationship is based on the same general constitutive model. To be consistent with the stress-strain relationships at high temperatures, the same limiting strain at yield $\varepsilon_{l,\theta}$ and the same ultimate strain $\varepsilon_{u,\theta}$ are applied to the stress-strain curve at ambient temperature. The stress-strain relationship for structural steel at ambient temperature is shown in Figure 3-3 (a).

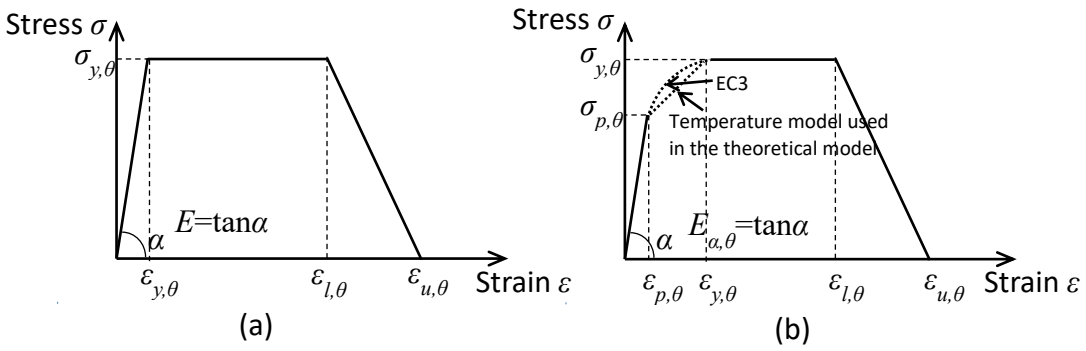

Figure 3-3 Stress-strain relationship of structural steel; (a) at ambient temperature; (b) at elevated temperatures

3.2.1 The deflection at mid-span

It has been mentioned above that, at Point 1, the mid-span vertical deflection of a beam is assumed to be induced elastically by bending and shear. The mid-span deflections at Points 2 and 3 both consist of a summation of the transverse drift of the shear panel due to shear force and the deflection caused by curvatures due to bending moment.

As the beam is short, for calculation simplification, the analytical model assumes that the mid-span deflection cause by bending moment from Point 1 to Point 3 can be calculated as

$$\Delta_{vb} = qL^4 / 384 k_{E,\theta} EI \tag{3-1}$$

While the overall deflection is assumed to be caused by bending and shear force, as shown in (3-2):

$$\Delta = \Delta_{vb} + \Delta_{vs} \tag{3-2}$$

For the transverse drift caused by shear buckling, it is assumed that the tensile strains of the tensile strips within the whole panel are identical. Thus, only the tensile strain of one representative tensile strip AB is calculated, as shown in Figure 3-4. The tensile

strain can be represented by the vertical deflection of the shear panel (Equation (3-5)). Therefore, by defining the tensile strain at Point 2 and 3 in Figure 3-2, the vertical deflection of the shear panel at Point 2 and 3 can be calculated.

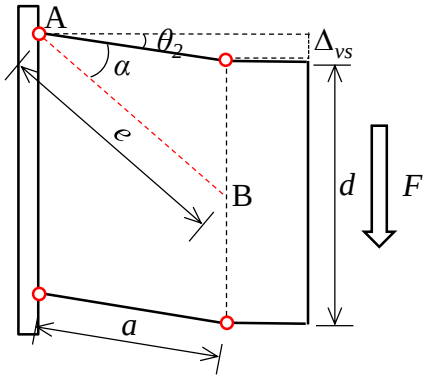

Figure 3-4 Representative strip and arbitrary point

For tensile strips,

$$\varepsilon_t = \delta_e / e \tag{3-3}$$

$$e = \sqrt{a^2 - \Delta_{vs}^2} / \cos(\alpha + \theta_2), \quad \delta_e = \Delta_{vs} \sin\alpha / \cos\theta_2 \tag{3-4}$$

Substituting Equation (3-3) into Equation (3-4) gives

$$\varepsilon_t = \Delta_{vs} \sin\alpha \cos(\alpha + \theta_2) / (\sqrt{a^2 - \Delta_{vs}^2} \cos\theta_2) \tag{3-5}$$

For Point 2, it is assumed that the principal tensile strain at an arbitrary point within the shear panel is 0.02, which is the yield strain in the material stress-strain relationship according to Eurocode 3 (CEN, 2005b). For Point 3, the strain at the arbitrary point is 0.15. Therefore, for any given distance *a* between plastic hinges on the flanges, the mid-span vertical deflection for Points 2 and 3 can be calculated. The key is to evaluate *a*.

3.2.2 Shear resistance of the beam

The calculation principle below is based on the equality of the internal plastic work and the external loss of potential energy of the load. Following this calculation, the distance between the plastic hinges can be calculated in order to fulfil the work equilibrium and to correspond to the smallest uniformly distributed load *q*. The method of calculating the internal work of the beam and the external loss of potential of the applied force is shown below.

Internal work of the beam web

It is assumed that the shear panel is composed of tensile and compressive strips, as shown in Figure 3-1 (a). Although the directions of both the tensile and compressive strips are initially defined in the second assumption above, the locations of the plastic hinges on the flanges are unknown. There are three possible cases, as shown in Figure 3-5, which may affect the internal work done by the tensile and compressive strips.

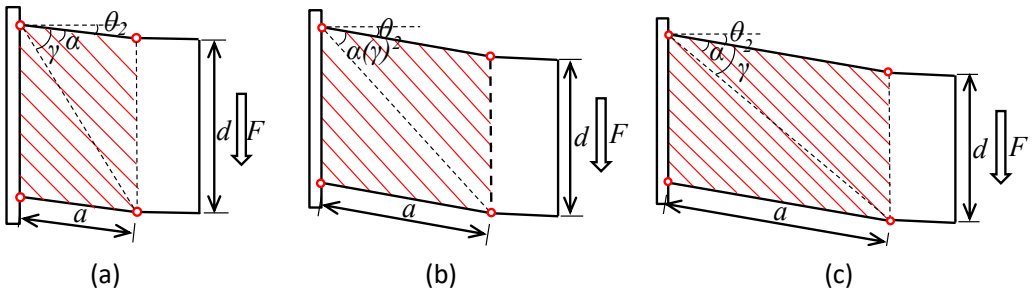

Figure 3-5 Possibilities for the position of plastic hinges; (a) Case 1; (b) Case 2; (c) Case 3

- Case 1

In Case 1, as shown in Figure 3-6 (a), the angle α is smaller than diagonal angle *γ*.

In Region B, for an arbitrary strip EF, the relationship between the elongation δ_{tB} of the strip and the resultant movement Δ_{rB} of Point F (as shown in Figure 3-6 (b)), is

$$\delta_{tB} = \Delta_{rB} \sin\alpha \tag{3-6}$$

A magnified figure of the stripe EF is shown in Figure 3-6 (b). The relationship between the vertical movement Δ_{vB} of Point F, which is equal to Δ_{vs} as shown in Figure 3-6 (a), and Δ_{rB} is

$$\Delta_{vB} = \Delta_{rB} \cos\theta_2 \tag{3-7}$$

Substituting Equation (3-6) into Equation (3-7), the relationship between the tensile elongation δ_{tB} of a strip and the vertical movement of the right-hand edge of the shear panel can be derived as

$$\delta_{tB} = \Delta_{vs} \sin\alpha / \cos\theta_2 \tag{3-8}$$

The internal work done due to the tensile stresses in Region B is

$$\begin{aligned} W_{Bt} &= \Delta_{vs} \int_0^{d\cos(\alpha+\theta_2)-a\sin\alpha} \sigma_t t_w \times (\sin\alpha / \cos\theta_2) dx \\ &= \Delta_{vs} \sigma_t t_w [d\cos(\alpha+\theta_2) - a\sin\alpha] \times \sin\alpha / \cos\theta_2 \end{aligned} \tag{3-9}$$

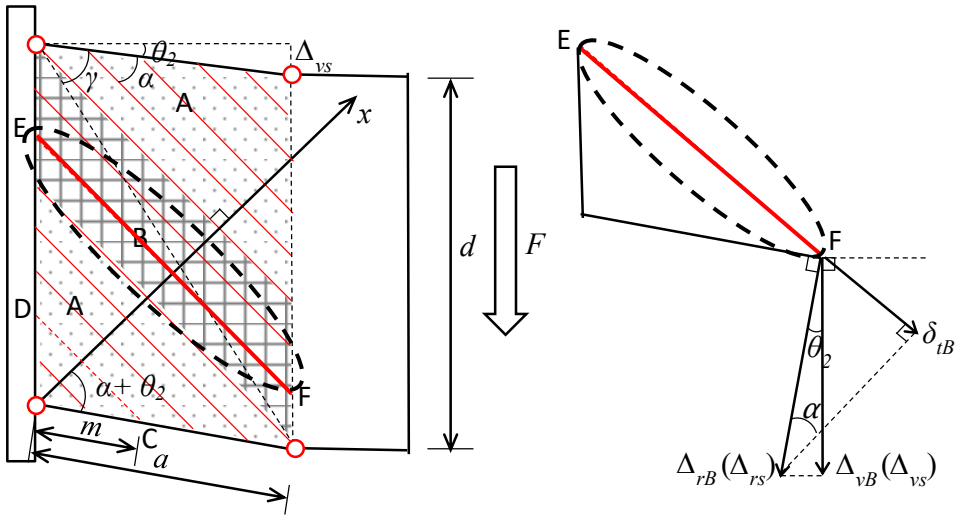

(a) (b)

Figure 3-6 Case 1: (a) Geometric relationship; (b) Movement relationship in Region B

In Region A in Figure 3-6 (a), the orientation of the strips in Region A is identical to that of the strips in Region B, and so the relationship between the tensile elongation in Region A and that in Region B is

$$\delta_{tA} = m\delta_{tB} / a \tag{3-10}$$

To obtain the relationship between the tensile elongation δ_{tA} and the vertical edge movement Δ_{vs}, substituting Equation (3-10) into Equation (3-8), gives

$$\delta_{tA} = (m / a) \times (\sin\alpha / \cos\theta_2) \times \Delta_{vs} \tag{3-11}$$

The internal work done by the tensile stresses in Region A is given as

$$W_{At} = 2\sigma_t t \int_0^{a\sin\alpha} (m / a) \times (\sin\alpha / \cos\theta_2) \times \Delta_{vs} dx \tag{3-12}$$

In Region A, $m = x / \sin\alpha$, and substituting this into Equation (3-12) gives

$$\begin{aligned} W_{At} &= \Delta_{vs} \times (2\sigma_t t / a\cos\theta_2) \int_0^{a\sin\alpha} x dx \\ &= a\sigma_t t \sin^2\alpha \times \Delta_{vs} / \cos\theta_2 \end{aligned} \tag{3-13}$$

The overall internal work done by stretching the entire shear panel is given by summation of W_{At} and W_{Bt}

$$\begin{aligned} W_T &= W_{At} + W_{Bt} \\ &= d\sigma_t t_w \cos(\alpha + \theta_2) \sin\alpha \times \Delta_{vs} / \cos\theta_2 \end{aligned} \tag{3-14}$$

- Case 2

In Case 2, the angle α of the tensile stresses to the upper edge of the panel is equal to *γ*, as shown in Figure 3-5 (b).

The internal work done by plastic stretching of the tensile strips can be determined similarly to that of Region A in Case 1. Case 2 has no Region B, and the internal work W_{At} done within Region A is still given by Eq (3-13). On the basis of the geometry of this case,

$$a\sin\alpha = d\cos(\alpha+\theta_2) \tag{3-15}$$

The overall internal work done by stretching of the shear panel is in this case given as Equation (3-14), which turns out to be identical to that of Case 1.

- Case 3

In Case 3, the angle α is larger than γ, as shown in Figure 3-5 (c). Again, the panel is divided into two regions A and B, as shown in Figure 3-7.

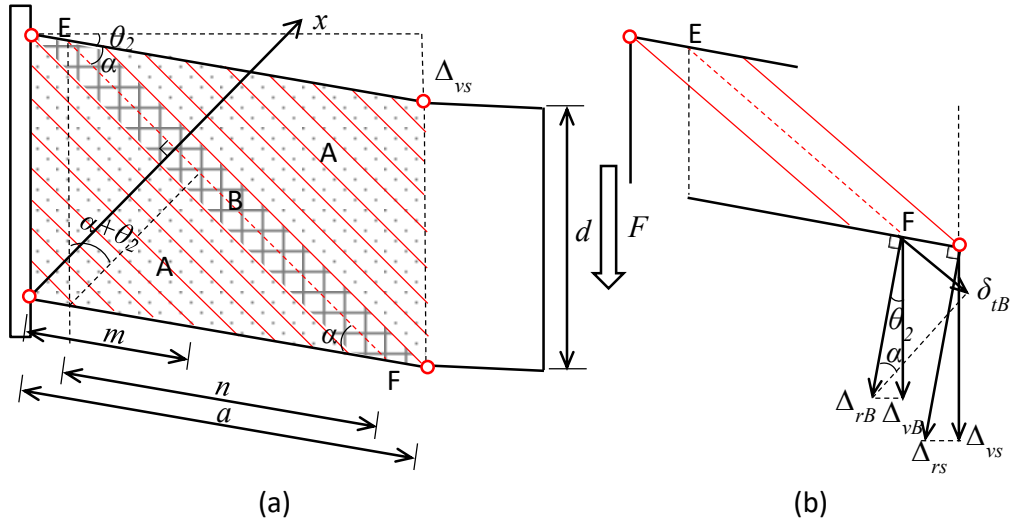

Figure 3-7 Case 3: (a) Geometric relationship; (b) Movement relationship in Region B

In Region B, for a sample tensile strip EF, the elongation of the strip can be related to the resultant movement of the right-hand edge of the shear panel:

$$\delta_{tB} = (n/a)\times\sin\alpha\times\Delta_{rs} \tag{3-16}$$

Based on the relationship, $\Delta_{vs} = \Delta_{rs}\cos\theta_2$

$$\delta_{tB} = \Delta_{vs}\times(\sin\alpha/\cos\theta_2)\times(n/a) \tag{3-17}$$

On the basis of geometry, $n = d\cos(\alpha+\theta_2)/\sin\alpha$

The relationship between the tensile elongation of a strip in Region B and the resultant movement of the right-hand edge of the panel Δ_{vs} is

$$\delta_{tB} = \Delta_{vs} \times (\sin\alpha / \cos\theta_2) \times d\cos(\alpha + \theta_2) / (\sin\alpha / a) \tag{3-18}$$

The internal work done by the tensile stresses in Region B is therefore

$$\begin{aligned} W_{Bt} &= \Delta_{vs} \int_0^{a\sin\alpha - d\cos(\alpha+\theta_2)} \sigma_t t_w \times (\sin\alpha / \cos\theta_2) \times d\cos(\alpha+\theta_2) / (\sin\alpha / a) dx \\ &= \Delta_{vs} \times [\sigma_t t_w d\cos(\alpha+\theta_2)\sin\alpha / \cos\theta_2 - \sigma_t t_w d^2 \cos^2(\alpha+\theta_2) / (a\cos\theta_2)] \end{aligned} \tag{3-19}$$

The internal work of Region A is given as,

$$W_{At} = 2\sigma_t t_w \int_0^{d\cos(\alpha+\theta_2)} (m/a) \times (\sin\alpha / \cos\theta_2) \times \Delta_{vs} dx \tag{3-20}$$

In Region A, $m = x/\sin\alpha$, and substituting this into Equation (3-20) gives

$$\begin{aligned} W_{At} &= \Delta_{vs} \times (2\sigma_t t_w / a\cos\theta_2) \int_0^{d\cos(\alpha+\theta_2)} x dx \\ &= \sigma_t t_w d^2 \cos^2(\alpha+\theta_2) \times \Delta_{vs} / (a\cos\theta_2) \end{aligned} \tag{3-21}$$

Then adding W_{At} and W_{Bt} gives the total internal work done by plastic stretching of the shear panel in this case.

$$W_T = d\sigma_t t_w \cos(\alpha+\theta_2)\sin\alpha \times \Delta_{vs} / \cos\theta_2 \tag{3-22}$$

It can be seen that the formulation of the internal work done by tension turns out to be the same for all the three cases. This shows that the tensile resistance of a shear panel is not sensitive to the locations of plastic hinges.

For compressive strips, there are also three cases depending on the locations of plastic hinges. Similarly to the tensile resistance, it can also be proved that the compressive capacity of a shear panel is not sensitive to the locations of the plastic hinges. For all three cases, the formulation of the internal work of the compressive strips is identical, and is given as

$$W_C = d\sigma_c t_w \sin(\alpha+\theta_2)\cos\alpha \times \Delta_{vs} / \cos\theta_2 \tag{3-23}$$

Therefore, the internal work of the web in the post-buckling stage is

$$\begin{aligned} W_W &= W_T + W_C \\ &= d\sigma_t t_w \cos(\alpha+\theta_2)\sin\alpha \times \Delta_{vs} / \cos\theta_2 + d\sigma_c t_w \sin(\alpha+\theta_2)\cos\alpha \times \Delta_{vs} / \cos\theta_2 \end{aligned} \quad (3\text{-}24)$$

It is not surprising to see that the three cases have an identical relationship for internal work since, when the entire panel is in uniform tension in one direction and in compression in the perpendicular direction, the internal work is derived similarly.

Internal work of the top and bottom flanges

The internal work of the flanges is the work done in deforming the four plastic hinges on the top and bottom flanges of the beam. The plastic moment resistance of each of the four hinges is

$$M_0 = \sigma_{y,\theta} b t_f^2 / 4 \quad (3\text{-}25)$$

In this equation M_0 does not account for the effect of the axial stresses in the flanges caused by bending of the overall beam cross-section, which reduces the flange moment capacity. The reduced moment capacity due to overall bending is given as

$$\begin{aligned} M_1 &= M_0[1-(\sigma_{t(c)} / \sigma_{y,\theta})^2] \\ &= \sigma_{y,\theta} b t_f^2 [1-(M_r \times 0.5 \times (d+0.5\times t_f) / (I \times \sigma_{y,\theta}))^2] / 4 \quad (M_1 \geq 0) \\ M_1 &= 0 \quad (M_1 < 0) \end{aligned} \quad (3\text{-}26)$$

Where M_r is the applied bending moment of the section

The internal work done by the plastic hinges in the flanges is therefore

$$W_f = 4M_1\theta_2 = \sigma_{y,\theta} b t_f^2 [1-(0.5\times M_r (d+0.5\times t_f) / I\sigma_{y,\theta})^2]\theta_2 \quad (3\text{-}27)$$

Total internal work of the beam

The analytical model can calculate the distance between the plastic hinges on the flanges. The calculated value indicates whether plastic hinges have been formed;

positive values indicate the occurrence of plastic hinges, whereas negative or imaginary values mean the opposite. If plastic hinges have been formed, the internal work done by the beam is given by summation of the work done in the beam web and flanges. Otherwise, the internal work is solely that of the beam web. It is assumed that the beam-end buckling zone is short, and the bending is resisted by compression or stretching the top and bottom flanges only; the deformation of the shear panel caused by bending can be neglected. Therefore, the internal work caused by bending is ignored in this calculation.

As discussed above, there are three key points to decide the theoretical force-deflection relationship. Point 1 is the end of elastic range, Point 2 refers to the initiation of buckling, and Point 3 represents failure. It is assumed that, at the initial buckling point (Point 2), the compressive stresses in the beam web have not been decreased due to the effect of buckling. Therefore, the tensile and compressive stresses are equal:

$$\sigma_t = \sigma_c \tag{3-28}$$

Using the Huber-von Mises plasticity criterion (von Mises, 1913), the relationship between the tensile and compressive stresses for a two-dimensional panel is

$$\sigma_c^2 + \sigma_t^2 + (\sigma_t - \sigma_c)^2 = 2\sigma_{y,\theta}^2 \tag{3-29}$$

Substituting Eqs. (3-28) and (3-29) into Equation (3-24), the internal work of the web panel is

$$W_W = \frac{\sigma_{y,\theta} d t_w \sin(2\alpha + \theta_2)}{\sqrt{3}\cos\theta_2} \Delta_{vs} \tag{3-30}$$

If plastic hinges occur, the internal work of the flanges can be calculated according to Equation (3-27).

Beyond the buckling point, the shear panel enters the post-buckling stage. For Point 3 in Figure 3-2, the post-buckling strength reduction is accounted for by reduction of the compressive stresses in the compressive strips. In the post-buckling stage, the compressive strips are considered as struts with three plastic hinges, as shown in Figure 3-8.

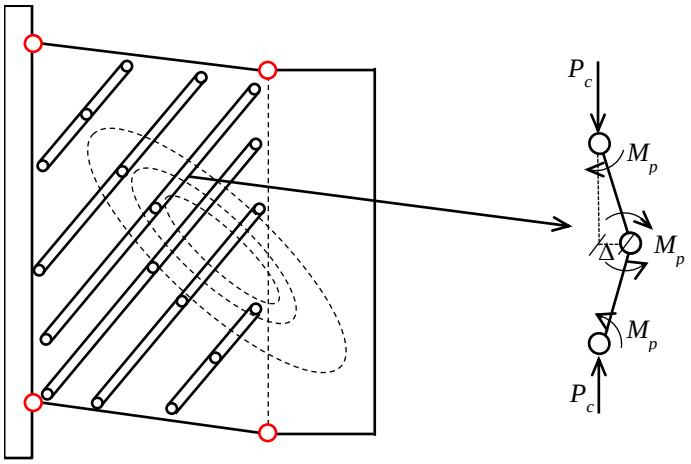

Figure 3-8 Struts representing compressive strips

It has been assumed that the central plastic hinge always forms at the mid-length of each strut, although this assumption may lead to an out-of-plane deflection shape, which is slightly different from reality. For each strut shown in Figure 3-8, the rectangular cross section can be divided into two parts, as shown in Figure 3-9. The axial compressive strength of the strut is resisted by Region A and its bending moment resistance is provided by Region B. Therefore,

$$P_c = \sigma_c h_c f \tag{3-31}$$

$$M_p = f(t_w^2 - h_c^2)\sigma_c / 4 \tag{3-32}$$

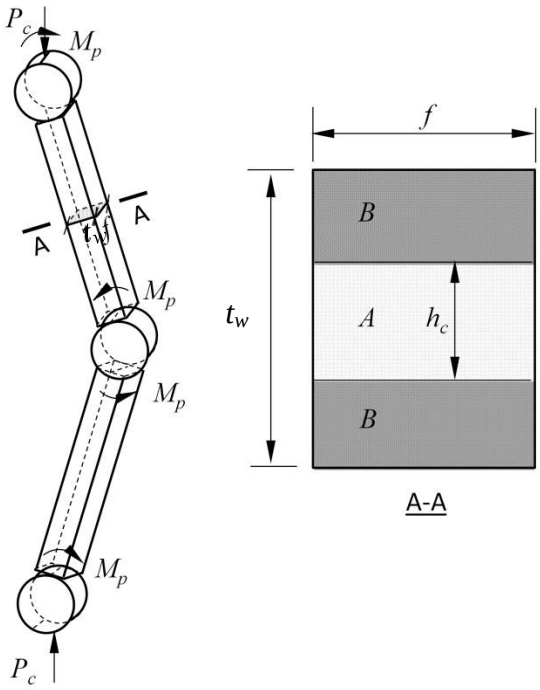

Figure 3-9 Cross section of one strut

Based on force equilibrium, the relationship between the compression force P_c of the strut and the plastic moment M_p at the plastic hinge is

$$P_c\Delta = 2M_p \tag{3-33}$$

Substituting Eqs. (3-31) and (3-32) into Equation (3-33), the height h_c of the compression zone can be calculated. The reduced compressive stress σ_c is proportional to h_c, which gives

$$\sigma_c = h_c\sigma_{y,\theta} / t_w \tag{3-34}$$

Following Equation (3-29), for any reduced σ_c, the tensile stress σ_t can be calculated. Both σ_c and σ_t are proportional to the yield strength. *A* and *B* in Equation (3-35) are the ratios of σ_c and σ_t to $\sigma_{y,\theta}$, respectively. *A* and *B* can be calculated by substituting Eqs. (3-32)-(3-34) into Equation (3-29) . Therefore, the high-temperature yield strengths can be defined as

$$\sigma_c = A\sigma_{y,\theta} \text{ and } \sigma_t = B\sigma_{y,\theta} \tag{3-35}$$

Substituting Equation (3-35) into Equation (3-24) gives

$$\begin{aligned} W_W &= W_T + W_C = \sigma_t t_w d \sin\alpha\cos(\alpha+\theta_2) + \sigma_c t_w d \sin(\alpha+\theta_2)\cos\alpha \times \Delta_{vs} / \cos\theta_2 \\ &= A\sigma_{y,\theta} t_w d \sin\alpha\cos(\alpha+\theta_2) + B\sigma_{y,\theta} t_w d \sin(\alpha+\theta_2)\cos\alpha \times \Delta_{vs} / \cos\theta_2 \\ &= \sigma_{y,\theta} t_w d \times \Delta_{vs} \times [0.5\times(A+B)\sin(2\alpha+\theta_2) + 0.5\times(B-A)\sin\theta_2] / \cos\theta_2 \end{aligned} \tag{3-36}$$

As has been presented above, for each a the transverse drift Δ_{vs} of the shear panel can be calculated. This can influence the reduction of compressive stress, which in return changes the calculated value of the distance between the plastic hinges. Therefore, an iterative process is used here to balance the value of a .

External work

If a beam is subjected to uniformly distributed load, the external work is given as

$$W_e = aq\Delta_{vs} / 2 + q(l-a)\Delta_{vs} = q(l - a/2)\Delta_{vs} \tag{3-37}$$

It has been explained above that internal work is only related to the distance *a* between plastic hinges, rather than the length of the shear buckling wave. This is also the case for the external work, as indicated by Equation (3-37).

As the calculation principle is based on equality of the internal plastic work and the external loss of potential energy of the load, the summation of the internal work of the shear panel web and flange is equal to the external work, as shown in Equation (3-38).

$$W_W + W_f = W_e \tag{3-38}$$

The distance *a* between plastic hinges on one flange can be calculated from Equation (3-38). As the uniformly distributed load *q* progressively increases, there will eventually be an *a* and the corresponding smallest *q* that fulfil Equation (3-38). It can be proved mathematically by solving the nonlinear Equation (3-38) that *a* is not related to either the yield stress or to Young's modulus. In other words, *a* is not related to temperature. It is worth noting that the distance *a* is related to the loading conditions.

The shear buckling model cannot be modelled as a separate component, as its behaviour is related to the loading conditions. However, it can be used to represent the beam-web shear buckling phenomenon for any given loading condition.

3.3 VALIDATION AGAINST FINITE ELEMENT MODELLING

In this study, the S4R element of ABAQUS (Hibbit *et al*., 2005) was adopted. This is a four-noded shell element which is capable of simulating buckling behaviour with reasonable accuracy. A mesh sensitivity analysis was carried out, and a 15mm x 15mm element size was selected to achieve optimum accuracy and efficiency. Riks analysis was used to track the descending load path of the shear panel in the post-buckling stage. An initial imperfection of amplitude $(d + t_f)/100$ was adopted. The shape of the initial imperfection was based on a first-buckling-mode analysis. Figure 3-10 (a) shows the finite element model of an isolated beam of Class 1 section. Six cases were analysed using different beam lengths with identical cross sections, at temperatures of 20^{o}C, 500^{o}C, 600^{o}C and 700^{o}C. The dimensions of the cross section are shown in Figure 3-10 (c). The same material properties used for the analytical model (illustrated in Figure 3-3) were applied. The detailed material properties used in both the FE and analytical models at ambient temperature are shown in Table 3-1. The material properties at high temperatures were reduced by applying the reduction factors for proportional limit stress, yield stress and Young's modulus to those at ambient temperature, as given in BS EN 1993-1-2. To save computing time, only half of a beam was modelled. The beam is fixed at one end. The other end of the FE model, which is the mid span of the beam, is allowed to move vertically without any rotation due to symmetry. As the effects of axial force caused by thermal expansion has not been

considered in the analytical model, the mid span is allowed to move horizontally in the FE model. Boundary conditions are shown in Figure 3-10 (b).

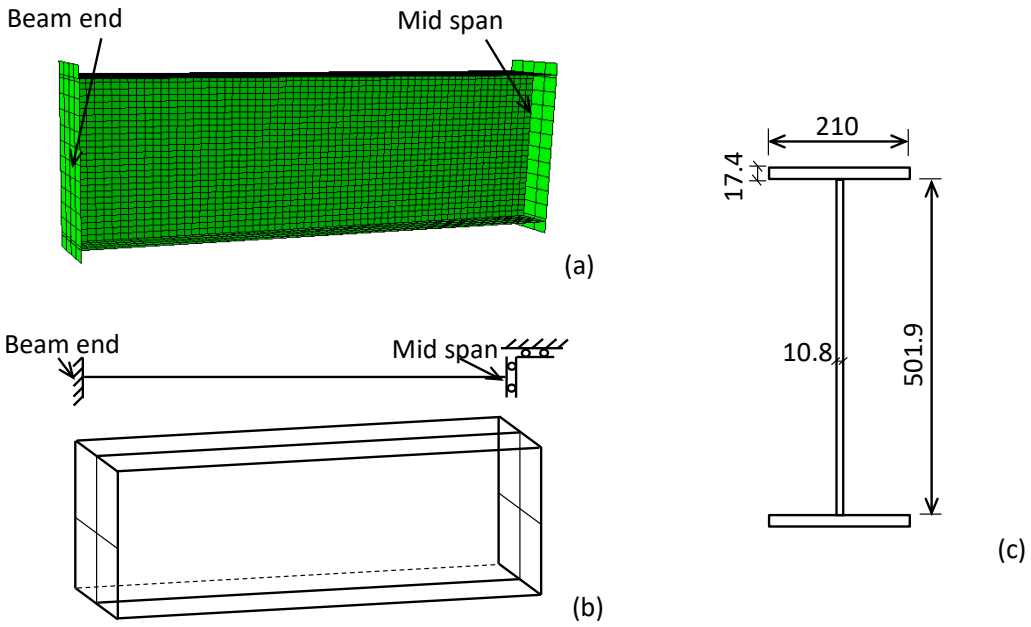

Figure 3-10 Finite element model; (a) Image of finite element model; (b) Boundary conditions; (c) Cross section dimensions (in mm)

Table 3-1 Material Properties of the FE model at ambient temperature

σ_y (N/mm^2)	E_α (N/mm^2)	$\varepsilon_{y,\theta}$ (%)	$\varepsilon_{t,\theta}$ (%)	$\varepsilon_{u,\theta}$ (%)
275	2.1e5	2	15	20

Since no practical experimental results exist for the shear buckling of Class 1 and 2 sections, the ABAQUS models cannot be validated against experiments directly. In order to verify the accuracy of the ABAQUS models, similar models in Chapter 4 were validated against experimental results at elevated temperatures. The ABAQUS models in this chapter were created on the basis of those in Chapter 4, by changing the loading and boundary conditions. The force-displacement relationships given by the analytical model and the ABAQUS analysis are compared in Figure 3-11, at

temperatures varying from 20^{o}C to 700^{o}C. The solid lines represent ABAQUS results, whereas the three round markers in each part of this figure show Points 1 to 3 given by the analytical model. As can be seen from Figure 3-11, the beam-end reaction forces given by the analytical model generally compare well with those from the ABAQUS model at all three stages. The theoretical results are always on the safe side for the cases analysed. More validations of the analytical models against ABAQUS model with different cross-section dimensions will be presented in Chapter 5.

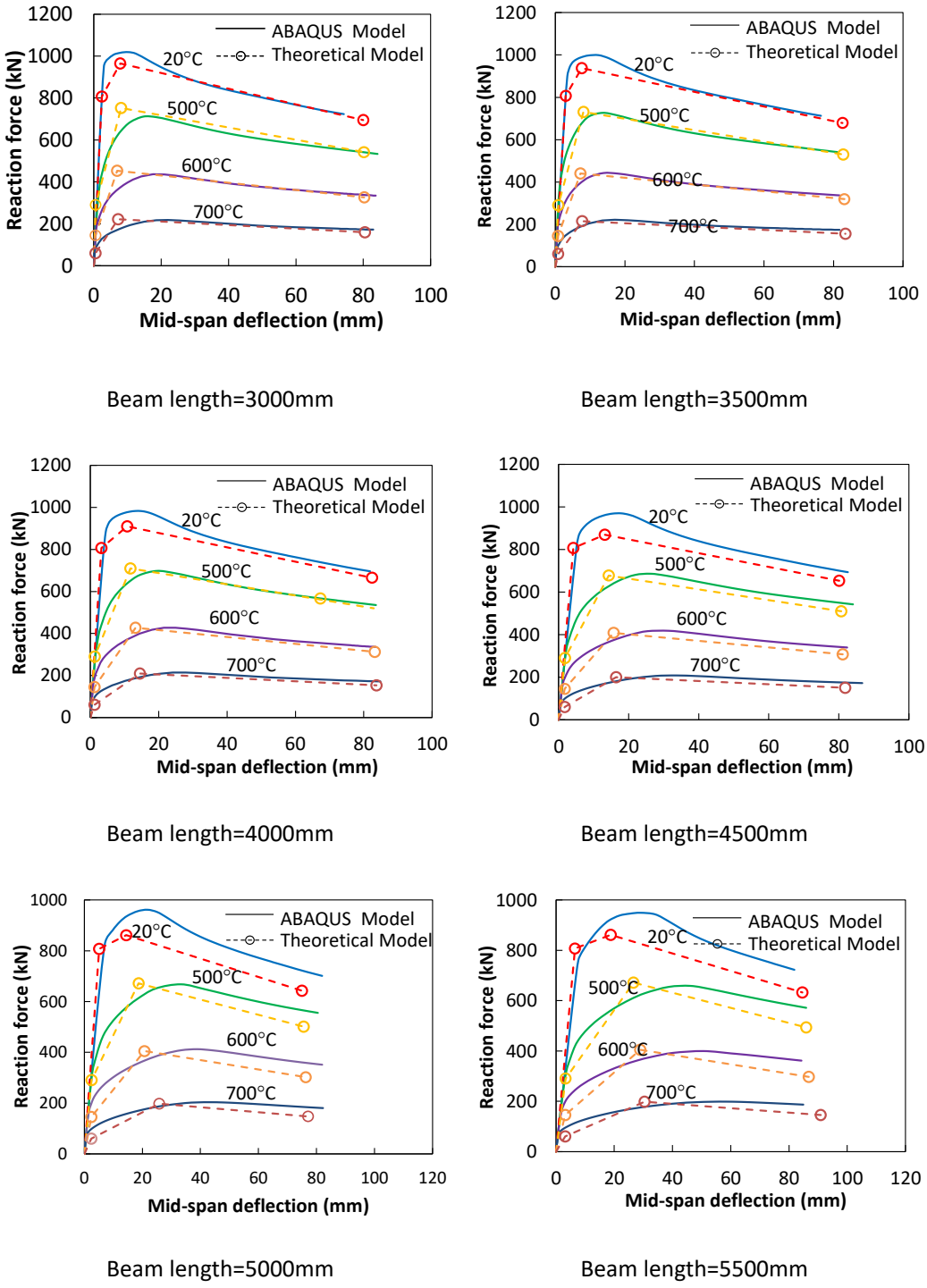

Figure 3-11 Comparison of force-displacement curves of beam mid-span between ABAQUS and theoretical analysis

The distances a between plastic hinges for different beam lengths, given by the analytical model, are shown in Figure 3-12. The distance a does not change with temperature. Therefore, for a particular beam length only one distance between

plastic hinges has been derived for any temperature. The solid line represents the variation of a with beam length at Point 2, and the dashed line is that for Point 3. The values of a for both Points 2 and 3 are positive definite for beams shorter than 5m. This means that the plastic hinges have been formed before beam web buckling occurs. For beams of lengths between 5-6m, the value of a at Point 2 doesn't exist, whereas that for Point 3 remains positive. This means that plastic hinges are formed on the flanges after the beam web buckles. These results can not be validated by FE modelling; even if plastic hinges occur on the flanges, the rotations across the hinges will be too small to be observed. For all beams shorter than 6m, failure is controlled by the shear buckling of the beam web. As the beam length increases, the distances between plastic hinges for both Points 2 and 3 do not exist. This means that plastic hinges do not form and shear buckling does not occur. This shift of failure mode is also observed from the ABAQUS model, as shown in Figure 3-13 and Figure 3-14.

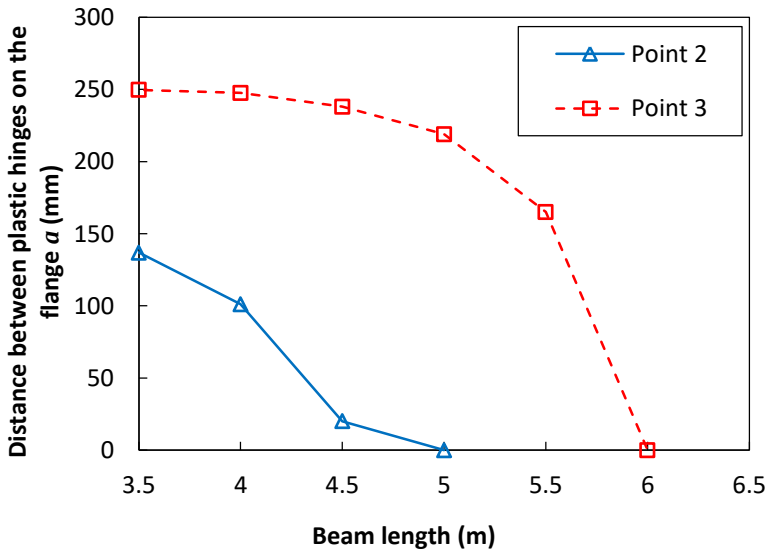

Figure 3-12 Distance between plastic hinges calculated from the analytical model

Figure 3-13 is a contour plot of the out-of-plane deflection of a representative 3m beam. The formation of plastic hinges and beam-web shear buckling are obvious from this figure. The same phenomenon occurs to beams of lengths between 3.5m and 5.5m. Figure 3-14 is a contour plot of out-of-plane deflection for a 6m beam, which fails by bottom-flange buckling rather than by shear buckling of the beam web. This may be caused by an increasing level of compressive stress, due to bending, in the bottom flanges as the beam length increases, which causes the bottom-flange buckling to occur prior to beam-web shear buckling. However, the bottom-flange buckling has not been included in the current analytical model, and will be considered in the next chapter.

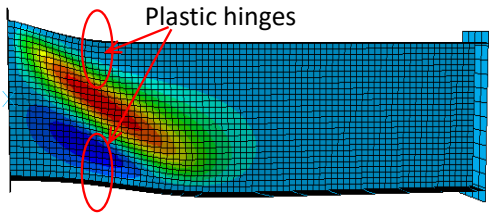

Figure 3-13 Shear buckling of 3m beam

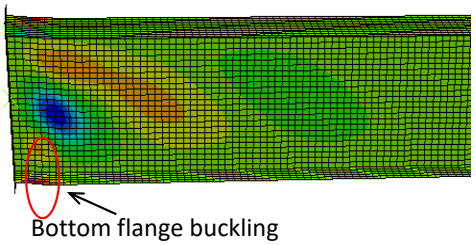

Figure 3-14 Bottom flange buckling of 6m beam

3.4 CONCLUSION

An analytical model has been created to predict the shear capacity and vertical deflection of shear panels at both ambient and elevated temperatures. The analytical model is capable of predicting the formation of plastic hinges on flanges, the initiation of beam-web shear buckling and the failure point for Class 1 and 2 sections. A tri-linear curve can be created by linking these three points, in order to track the load-deflection route of the shear panel. In the following chapter a new component-based shear panel

element, which considers the shear panel as a separate component, will be created based on the analytical model.

The theoretical results have been validated against finite element modelling using ABAQUS over a range of geometries. For beams for which beam-web shear bucking is the main 'failure' mode, the comparisons between the theoretical and FE models have shown that the proposed method provides satisfactory accuracy in terms of both shear capacity and mid-span vertical deflection. However, as beam length increases, the 'failure' mode switches to bottom-flange buckling. This phenomenon can be observed from the ABAQUS models. However, bottom-flange buckling has not been involved in the analytical model so far.

4.

COMBINING THE EFFECTS OF SHEAR BUCKLING AND BOTTOM-FLANGE BUCKLING IN THE POST-BUCKLING STAGE

4.1. INTRODUCTION

The Cardington Fire Tests (Newman *et al*., 2000) indicated that combinations of beam-web shear buckling and flange buckling are very prevalent under fire conditions (Figure 4-1). This combination of phenomena can significantly influence the internal forces in the connections. However, the contribution of the combination of beam-web shear buckling and flange buckling in the vicinity of beam ends has not been taken into consideration by almost any of the existing research. The analytical model which simulates pure beam-web shear buckling behaviour has been described in Chapter 3. It has been stated in the Introduction chapter that, as the beam length increases, bottom-flange buckling can occur simultaneously with beam-web shear buckling, and the occurrence of bottom-flange buckling can have a significant influence on the bolt-row force distribution, as well as beam mid-span deflection at both ambient and elevated temperatures. As the bottom-flange buckling phenomenon was not considered in the analytical model of Chapter 3 it will be presented, in combination with web shear buckling, in this chapter.

Figure 4-1 Flange buckling and beam-web shear buckling in combination (Newman et al., 2000)

Elghazouli *et al*. (1999) implemented a local-buckling model within a frame analysis program to investigate the influence of local buckling at the beam ends on the fire response of frame members and sub-assemblies. This study indicated that, although local buckling at the beam ends may not directly trigger overall structural collapse, it can have detrimental effects on the deflections of, and load re-distributions between, structural elements. This could influence the fire resistance of the structure. However, the local buckling model presented in Elghazouli's work is based on elastic plate buckling theory, which is not appropriate for representing the buckling behaviour of Class 1 and 2 sections. No sufficient validation of the local-buckling model presented in his paper has been provided. A body of research (Kato, 1965, Climenhaga and Johnson, 1972, Gioncu and Petcu, 1995, Gioncu and Petcu, 1997, Gioncu and Mazzolani, 2003) has been carried out to investigate the local in-plane flange buckling phenomenon, including both the pre- and post-buckling stages. Recent research has a common solution for the pre-buckling stage, while different collapse models of the post-buckling stage have been proposed since 1965 (Kato, 1965). The local buckling collapse mechanisms in all these models are composed of yield lines and plastic zones. The choices of possible yield line patterns are based on experimental observations. All models assume that the yield lines, formed within the elastic buckling wavelength, will not change their positions in the post-buckling stage. However, these studies nearly all focus on the effects of local buckling on the rotational capacity and ductility of beam-ends, rather than on its influence on the global structural behaviour. Dharma extended the most up-to-date ambient temperature model, proposed by Gioncu and Petcu (2003), to elevated-temperature applications for both steel beams (Dharma and Tan, 2007b) and composite beams (Dharma and Tan, 2008). However, Dharma's research has been shown to be extremely conservative for thin-web beams at elevated

temperatures (Dharma, 2007). The detailed gap between the existing Dharma's model and the analytical model needed has been introduced in Chapter 2.

In this chapter, the new analytical model (1) considers the combination and interaction of flange buckling and web shear buckling; and (2) adopts a revised calculation approach for flange buckling wavelength to represent slender beams. Two comparison cased were considered to compare the analytical model with Dharma's model and finite element (FE) models using ABAQUS. In the first comparison case, the FEA analyses a short cantilever with a fixed length of $2\,d$ at the end of the beam. It is able to consider any loading condition, without uniformly distributed load on top of the buckling panel, by varying the combination of shear force and bending moment transferred to the end of the buckling panel. In the second comparison case, the FEA analyses a short cantilever with the length from the beam end to its adjacent point of contraflexure. It is able to consider any loading condition, with uniformly distributed load on top of the buckling panel, by varying the shear force at the end of the cantilever and the uniformly distributed load on top of the beam. After validation, the analytical model has been implemented in calculating the deflection of a full-length beam, and this has been compared with an equivalent ABAQUS model. The analytical model will eventually be integrated into the software Vulcan, to be placed in structural models between the existing connection element, which is assumed to exist at the column-face, and the beam element, using a component-based approach. Performance-based analysis will then be carried out to investigate the overall structural behaviour under fire conditions.

4.2. DEVELOPMENT OF ANALYTICAL MODEL

The proposed analytical model uses a short cantilever to represent the beam-end buckling zone; the length of this cantilever is considered as equal to the beam depth d. By applying different combinations of moment and shear force at its free end, this model can represent the bucking panel at the end of a beam of any length, and with arbitrary loading and boundary conditions. The corresponding shear force F and bending moment M at the end of the buckling element can be transferred from the adjacent part of the beam. No horizontal restraint is applied to the buckling panel ends. In order words, the analytical model does not consider the axial force caused by restraint to thermal expansion. This model aims to deal with the post-buckling phase when the full yield line mechanism has developed under certain loading conditions and temperatures. If these loading conditions cannot be fulfilled (for example when, for a simple beam, the bending moment is not large enough to trigger bottom-flange buckling), the proposed buckling element will remain a part of a normal beam. The complete force-deflection relationship of the buckling element includes three stages: non-linear pre-buckling, plateau and post-buckling. If the material properties (Figure 4-2) for steel at temperatures higher than 400°C are used, the vertical force-deflection relationship of the buckling element without considering the axial force can be illustrated schematically as in Figure 4-3.

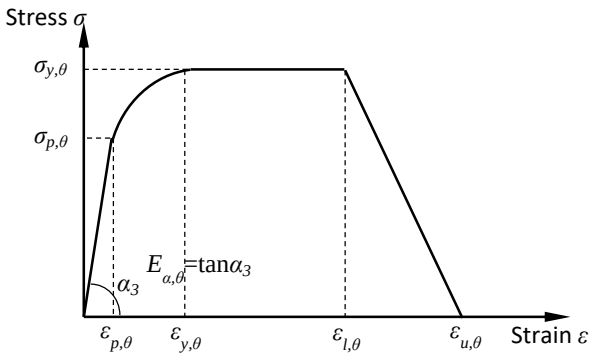

Figure 4-2 Stress-strain relationship of structural steel

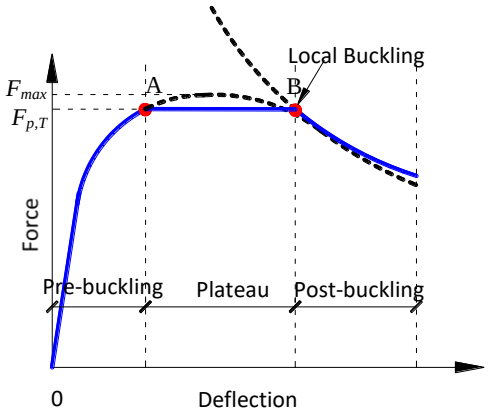

Figure 4-3 Schematic force-deflection curve of a beam-end buckling model

4.2.1 Pre-buckling stage and plateau

The characteristics of the buckling element in the pre-buckling stage are identical to normal beams, with linear elastic and nonlinear phase, as shown in Figure 4-3. In the plateau stage, a plateau line at force level $F_{\mathrm{p},T}$, which is the force that causes the fully plastic moment resistance to be reached, is drawn to connect Points A & B in Figure 4-3 with the pre- and post-buckling curves; this has been defined as the plateau stage.

4.2.2 Post-buckling stage

Development of plastic buckling mechanism

The plastic buckling mechanism (Figure 4-4) forms at Point B in Figure 4-3. The buckling mechanism is composed of yield lines and plastic yield zones. The yield line pattern adopted in this study is based on Dharma's model (2007).

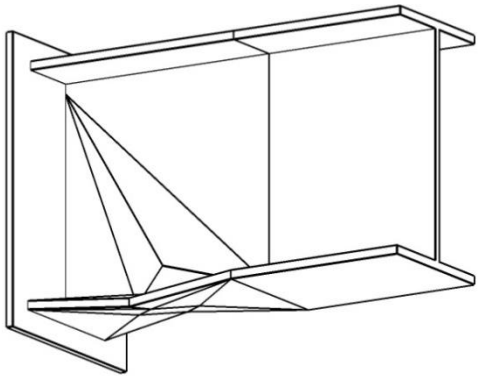

Figure 4-4 Plastic Buckling Mechanism

The deflection of the buckling zone is composed of the total deflection due to both bottom-flange buckling and beam-web shear buckling. In this study, the individual effects of these two buckling phenomena are considered. As the buckling zone is considerably shorter than the entire beam, it is assumed that the influence of bottom-flange buckling is to cause a rotation of the whole beam-end about the intersection of the web yield lines, which is approximated as the top flange of the beam (due to stretching of the top flange and buckling of the bottom flange), as shown in Figure 4-5 (a). Beam-web shear buckling can cause transverse drift of the shear panel, as shown in Figure 4-5 (b). Therefore, the combined effects of flange buckling and beam-web shear buckling on the overall beam vertical deflection is as expressed in Figure 4-5 (c).

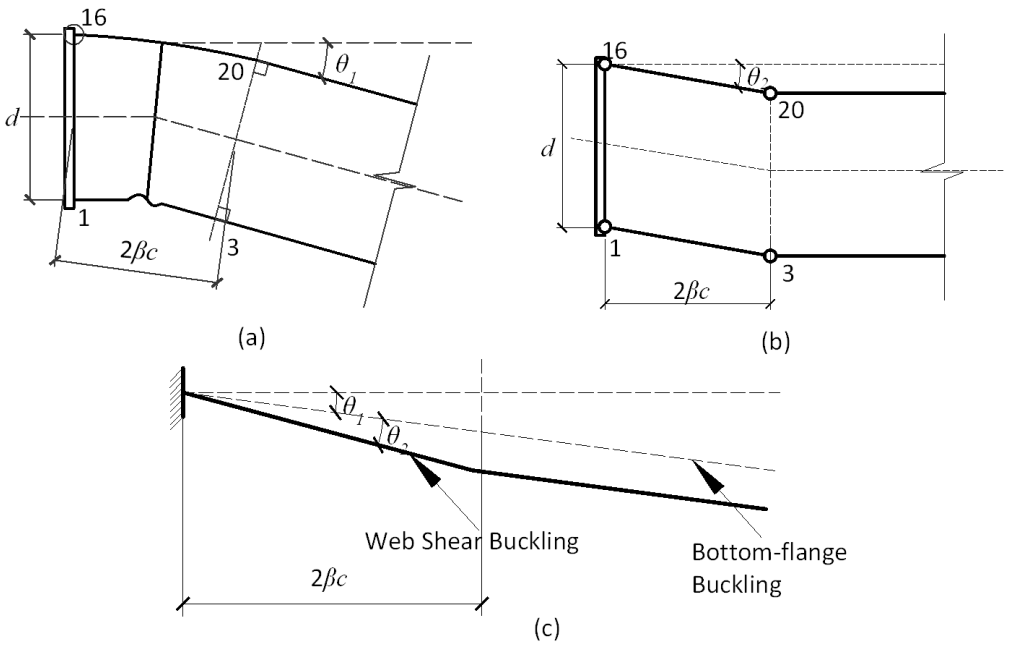

Figure 4-5 The effects of flange buckling and beam-web shear buckling on beam vertical deflection (a) bottom-flange buckling; (b) shear buckling; (c) total deflection

- Bottom-flange buckling

When bottom-flange buckling occurs, the buckled shape is composed of a squashed quadrilateral plastic zone (4-5-7-6) and several yield lines, as shown in Figure 4-6 (a). The centre of the plastic zone is at the centre of the buckled panel in both directions. It is assumed that the plate facets surrounded by the yield lines rotate rigidly about the yield lines. The plastic zone (shaded area in Figure 4-6 (a)) will be squashed along 5-6 due to compression; it can also rotate about Line 5-6. It is assumed that there is no relative rotation between the beam web and the bottom flange at their intersection (web and flange will always be perpendicular to each other). Therefore, the rotation of the plastic zone in the bottom flange will lead to the rotation of the beam web, as shown in Figure 4-7. This results in an isosceles-right-triangle plastic zone being formed in the beam web (5-6-11 in Figure 4-8). This zone will be compressed along line

5-6 as well as rotate about this line. Several yield lines form in the beam web as a result of this rotation; the centre of rotation is located where the neutral axis of bending meets the beam end (Point 12 in Figure 4-8). The angle of rotation due to bottom-flange buckling is θ_1, as shown in Figure 4-5 (c). The top flange remains in-plane, experiencing only plastic tensile deformation at the beam end, as shown in Figure 4-6 (b).

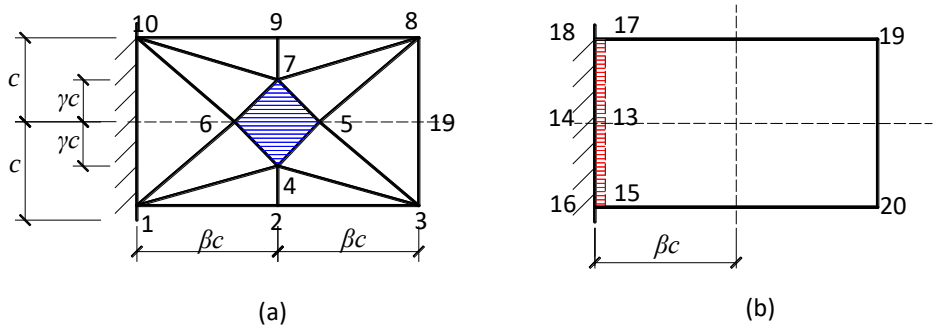

Figure 4-6 Flange yield line mechanism (a) bottom flange; (b) top flange

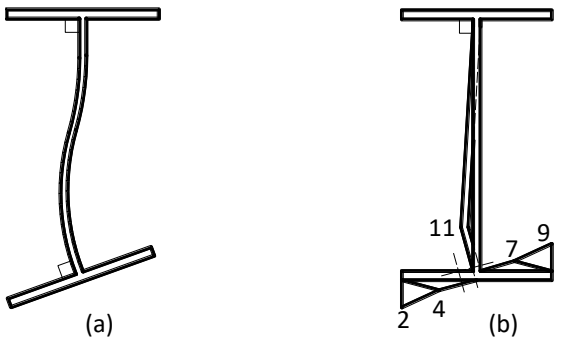

Figure 4-7 Deformation compatibility between bottom flange and beam web (a) real-beam deformation; (b) deformation in the model

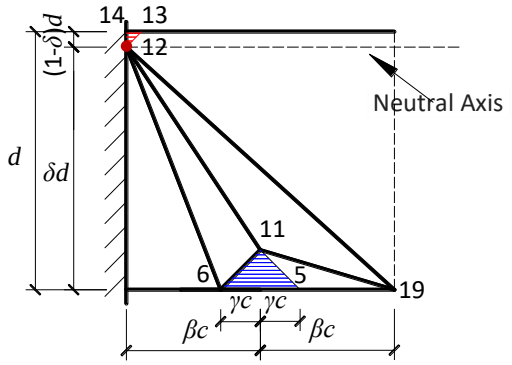

Figure 4-8 Beam-web yield line pattern

- Beam-web shear buckling

When beam-web shear buckling occurs, the two opposite edges (Lines 1-16 and 3-20 in Figure 4-5 (b)) of the buckling panel move in parallel due to shear force, producing two plastic hinges on each of the top and bottom flanges. The angle of rotation due to this transverse drift is θ_2, as shown in Figure 4-5 (b). The four edges of the buckling zone are considered to be rigid. The beam web is assumed to be composed of tensile and compressive strips, which are aligned at 45° to the horizontal and perpendicular to each other, as shown in Figure 4-9 (a). When the buckling panel deforms due to shear force, the tensile strips are elongated due to the tensile force component of the vertical shear force, while the compressive stresses are shortened due to its orthogonal compressive force component. The out-of-plane deformation is assumed to occur only within the yield lines 12-6-19 (Figure 4-8).

The out-of-plane deflection of the beam web due to bottom-flange buckling and that due to shear buckling need to be identical to ensure geometric compatibility. This implies a relationship between the beam end rotations ϑ_1 and ϑ_2, due to bottom-flange buckling and shear buckling.

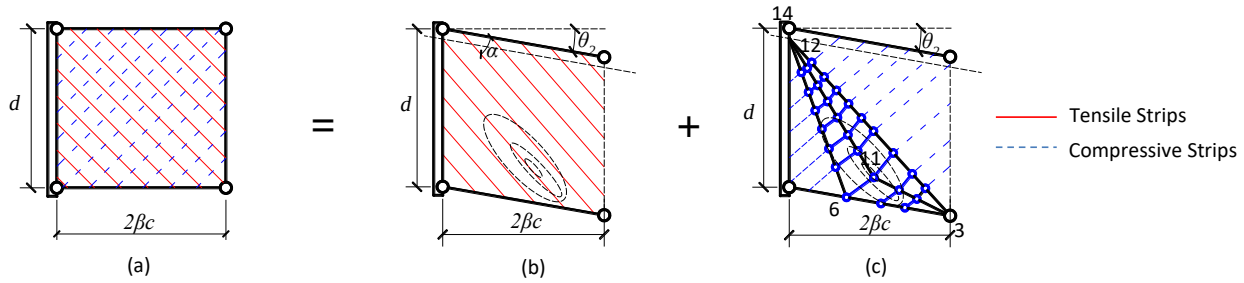

Figure 4-9 Beam-web behaviour under shear force (a) Overall behaviour; (b) Tensile strips; (c) Compressive strips

- Length of the buckling panel

The flange-buckling wavelength given by Dharma (2007) tends to considerably over-estimate the capacity of a slender beam. In most fire tests, only one shear-buckling wave has been observed, and the shear-buckling wave is usually aligned at around 45° to the horizontal. Therefore, the shear-buckling panel is usually no longer than the beam depth d , and the flange buckling wave lies in between the two plastic hinges in the bottom flange. Hence, the flange-buckling wavelength L_p can be calculated according to Equation(4-1) considering the effects of steel grade and temperatures.

$$L_p = 2\beta c = 2\times 0.713\sqrt{\frac{275}{\sigma_{y,\theta}}}\left(d/b\right)^{1/4}\left(t_f/t_w\right)^{3/4}\left(k_E/(0.7k_y)\right)\times c \qquad (4\text{-}1)$$

The calculation of L_p is based on elastic plate theory by Timoshenko (1961), and by introducing reduction factor $k_E/(0.7k_y)$ to consider high temperatures. In most fire tests, only one shear-buckling wave has been observed, and the shear-buckling wave is usually aligned at around 45° to the horizontal. Therefore, the shear-buckling panel is usually no longer than the beam depth d, and the flange buckling wave lies in between the two plastic hinges in the bottom flange. Hence, it has been assumed that the flange-buckling wavelength L_p, calculated by Equation (4-1), is limited to the beam

depth d. The out-of-plane deflection of the beam web due to bottom-flange buckling and that due to shear buckling need to be identical to ensure geometric compatibility. This implies a relationship between the beam end rotations θ_1 and θ_2, due to bottom-flange buckling and shear buckling.

Calculation principle

The calculation principle is based on equality of the internal plastic work and the loss of potential energy due to the external load:

$$W_{\text{int}} = W_{ext} \tag{4-2}$$

- Internal Work

The internal plastic work W_{int} includes the work done in the flanges ($\sum_i (W_l)_i$ due to the rotation about the yield lines and $\sum_j (W_z)_j$ due to axial deformation of the plastic zones) and the work W_W done in the beam web due to its transverse drift during shear buckling. The deformations of the plastic zones are uniform across each of them, and the rotations about yield lines are uniform along every yield line. Summaries of the lengths and rotations of the yield lines, as well as the volumes and strains of the plastic zones, are given in Table 4-1 and Figure 4-5.

The total internal plastic work is then given by Equation (4-3). The factor γ, which determines the dimension of the bottom-flange plastic zone, and the distance δd between the neutral axis of bending and the bottom flange, are to be determined through optimization on the basis of minimizing the total internal plastic work.

$$W_{\text{int}} = \sum_i (l_p t^2 \sigma_{y,\theta} \theta)_i / 4 + \sum_j (A_p t \sigma_{y,\theta} \varepsilon)_j + W_W \tag{4-3}$$

Table 4-1 Components of internal plastic work for plastic squash zones

Plastic Zones			
Zone(*j*)	Volume ($A_p t$)	Strain (ε)	Stress ($\sigma_{y,\theta}$)
4-5-7-6	$2\gamma^2 c^2 t_f$	$\theta_1 \delta d / (2\gamma c)$	$\sigma_{yf,\theta}$
5-6-11	$\gamma^2 c^2 t_w$	$\theta_1 \delta d / (2\gamma c)$	$\sigma_{yw,\theta}$
12-13-14	$(1-\delta)^2 d^2 t_w / 2$	θ_1	$\sigma_{yw,\theta}$
15-16-18-17	$2(1-\delta) c t_f d$	θ_1	$\sigma_{yf,\theta}$

Table 4-2 Components *of internal plastic work for yield lines*

Yeild Lines			
Line (*i*)	Length (l_p)	Rotation (ϑ)	Stress ($\sigma_{y,\vartheta}$)
2-4; 7-9	$(1-\gamma)c$	$2(\gamma/\beta\chi)^{1/2}\theta_1^{1/2}$	σ_{eq}
1-10; 3-8	$2c$	θ_2	σ_{eq}
1-4; 3-4; 7-8; 7-10;	$[\beta^2+(1-\gamma^2)]^{1/2}c$	$\frac{1}{[\beta^2+(1-\gamma^2)]^{1/2}}[\beta/(1-\gamma)+\frac{\beta^2-3\gamma-\gamma\beta+1}{\gamma(1+\beta-\gamma)}](\beta\gamma/\chi)^{1/2}\theta_1^{1/2}$	σ_{eq}
1-5; 3-6; 5-8; 6-10;	$[1+(\beta-\gamma)^2]^{1/2}c$	$\frac{[1+(\beta-\gamma)^2]^{1/2}}{\gamma(1+\beta-\gamma)}(\beta\gamma/\chi)^{1/2}\theta_1^{1/2}$	σ_{eq}
4-5; 4-6; 5-7; 6-7;	$2^{1/2}\gamma c$	$2^{1/2}\frac{1}{\gamma(1+\beta-\gamma)}(\beta\gamma/\chi)^{1/2}\theta_1^{1/2}$	σ_{eq}
3-11	$((\gamma c)^2+(d/2)^2)^{1/2}$	$2^{1/2}[\frac{1-(1-\beta)\chi}{1-(1+\beta)\chi}]^{1/2}\theta_1^{1/2}$	$\sigma_{yw,\theta}$
6-11	$2^{1/2}\gamma c$	$(\frac{2}{\gamma})^{1/2}[\frac{1-(1+\beta/\gamma)\chi}{1-(1-\beta/\gamma)\chi}]^{1/2}\theta_1^{1/2}$	$\sigma_{yw,\theta}$
5-12	$[1+(1+\beta)^2\chi^2]^{1/2}\delta d$	$\frac{1}{\chi^{1/2}}[\frac{1-(1-\beta)\chi}{1-(1+\beta)\chi}]^{1/2}[1+(1+\beta)^2\chi^2]^{1/2}\theta_1^{1/2}$	$\sigma_{yw,\theta}$
6-12	$[1+(1-\beta)^2\chi^2]^{1/2}\delta d$	$\frac{1}{\chi^{1/2}}[\frac{1-(1+\beta/\gamma)\chi}{1-(1-\beta/\gamma)\chi}]^{1/2}[1+(1-\beta/\gamma)^2\chi^2]^{1/2}\theta_1^{1/2}$	$\sigma_{yw,\theta}$
11-12	$[(1-\chi)^2+(\beta\chi/y)^2]^{1/2}\delta d$	$\frac{(1-\chi)^2+(\beta\chi/\gamma)^2}{(1-\chi)^2-(\beta\chi/\gamma)^2}]^{1/2}\theta_1^{1/2}$	$\sigma_{yw,\theta}$
15-13-17	$2c$	$[\frac{(1-\chi)^2+(\beta\chi/\gamma)^2}{(1-\chi)^2-(\beta\chi/\gamma)^2}]^{1/2}\theta_1^{1/2}$	σ_{eq}
16-18;19-20	$2c$	θ_2	σ_{eq}

In *Table 4-2*, the relationship in Equation (4-4) exists. Equation

$$\chi = (\gamma c)/(\delta d) \tag{4-4}$$

The normal stresses σ_r, which are perpendicular to the yield lines, and the shear stresses τ_r which are parallel to the yield lines (Figure 4-10) can both influence the reduced yield stresses σ_{eq} across the yield lines, and therefore cause a reduction of the flexural capacity M_{eq}. The stresses σ_r and τ_r are components of the axial stresses σ_{tf} and σ_{cf}, parallel to the beam length, which are caused by overall beam bending. According to the Mohr's Circle in Figure 4-10, σ_r and τ_r can respectively be calculated using Eqs. (4-5) and (4-6).

$$\sigma_r = 0.5(1+\cos(2\alpha_1))\sigma_{t(c)f} \tag{4-5}$$

$$\tau_r = 0.5\sin(2\alpha_1)\sigma_{t(c)f} \tag{4-6}$$

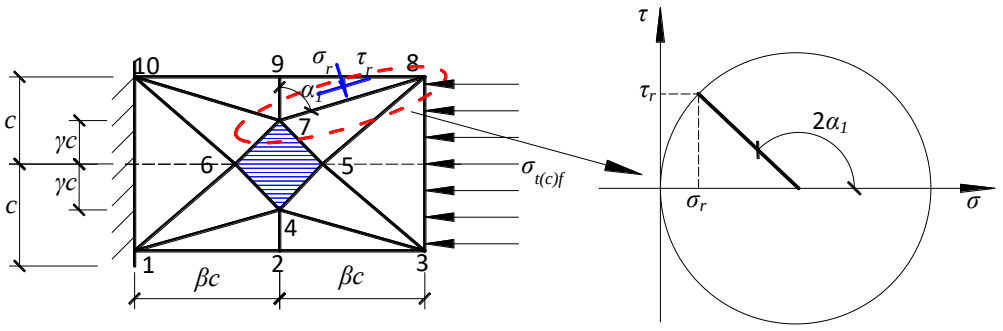

Figure 4-10 Mohr's circle for one yield line (7-8)

in which α_1 is the acute angle between the yield line and the vertical axis. The yield stress σ_{eq1} of the yield lines, considering only the effect of σ_r, is given as Equation (4-7).

$$\begin{aligned}\sigma_{eq1} &= \sigma_{yf,\theta}[1-(\sigma_{t(c)f}/\sigma_{yf,\theta})^2] \\ &= \sigma_{yf,\theta}[1-((0.5(1+\cos(2\alpha_1))\sigma_{t(c)f}/\sigma_{yf,\theta})^2]\end{aligned} \quad (4\text{-}7)$$

The relationship between the shear stress τ_r and the reduced equivalent yield stress σ_{eq} can be expressed as Equation (4-8).

$$(\sigma_{eq}/\sigma_{eq1})^2+(\tau_r/\tau_{eq1})^2=1 \quad (4\text{-}8)$$

where $\tau_{eq1}=\sigma_{eq1}/\sqrt{3}$.

Substituting Equation (4-7) into Equation(4-8) gives

$$\sigma_{eq}=\sigma_{yf,\theta}[1-(0.5(1+\cos(2\alpha_1))\sigma_{t(c)f}/\sigma_{yf,\theta})^2][1-(0.5\sin(2\alpha_1)/\sqrt{3})^2]^{1/2} \quad (4\text{-}9)$$

It has previously been ascertained in Chapter 3 that the internal work of the deformed beam web due to shear buckling is given by:

$$W_W=W_T+W_C=(\sigma_t td\sin\alpha\cos(\alpha+\theta_2)+\sigma_c td\sin(\alpha+\theta_2)\cos\alpha)\Delta_{vs}/\cos\theta_2 \quad (4\text{-}10)$$

where α is the angle between the tensile strips and the upper edge of the shear-buckling panel, as shown in Figure 4-10 (b). Δ_{vs} is the vertical displacement of the shear-panel edge, which is equal to $2\beta c\theta_2$. According to the Huber-von Mises plasticity criterion (von Mises, 1913), the relationship between the tensile and compressive stresses for a two-dimensional panel is given by

$$\sigma_c^2 + \sigma_t^2 + (\sigma_t - \sigma_c)^2 = 2\sigma_{yw,\theta}^2 \qquad (4\text{-}11)$$

The compressive strips in the beam web can be regarded as struts, each of which has three plastic hinges, as shown in Figure 4-11. The method to calculate the reduced compressive force of each strut after beam-web buckling as well as to calculate the tensile force for each strut is identical to that presented in Chapter 3.

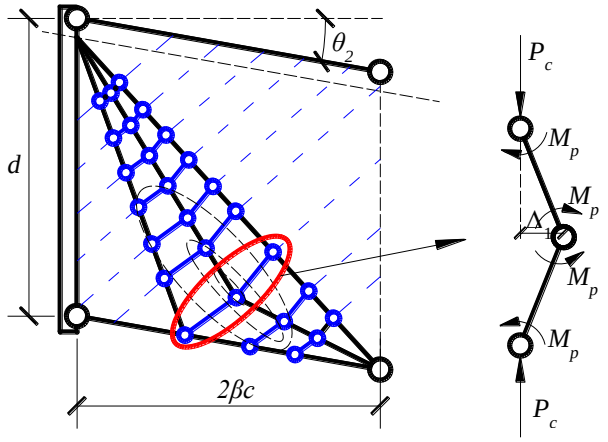

Figure 4-11 Strut representing an arbitrary compressive strip

- External work

The total external work can be expressed by Equation (16), where Δ_i includes the deflections caused by both bottom-flange buckling and beam-web shear buckling. Elastic deflection can be neglected due to the relatively short length of the buckling element.

$$W_{ext} = \sum P_i \Delta_i = F(4\beta c)\theta_1 + F(2\beta c)\theta_2 + M((4\beta c)\theta_1 + (2\beta c)\theta_2)/(4\beta c) \qquad (4\text{-}12)$$

- Deflection compatibility

The deflection compatibility is based on the assumption that the out-of-plane deflection of Point 11 (Figure 4-12) caused by bottom-flange buckling is identical to that caused by shear buckling. For the out-plane deflection caused by bottom-flange

buckling, the side lengths of the Triangle 1-4-5, shown in Figure 4-13, are illustrated in Eqs. (4-13) - (4-15).

$$l_1 = [1+(\beta-\gamma)^2]^{1/2} c \tag{4-13}$$

$$l_2 = 2^{1/2} \gamma c \tag{4-14}$$

$$l_3 = [\beta^2+(1-\gamma)^2]^{1/2} c \tag{4-15}$$

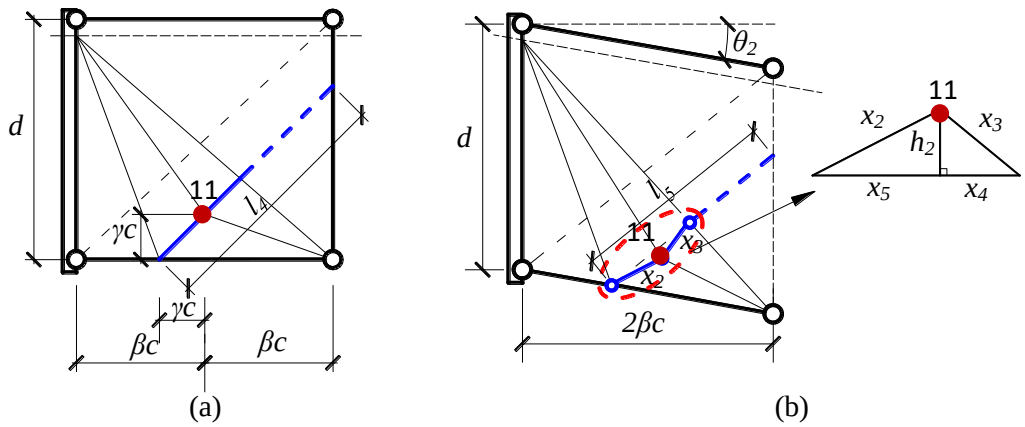

Figure 4-12 Deformed shape caused by shear buckling of the beam web

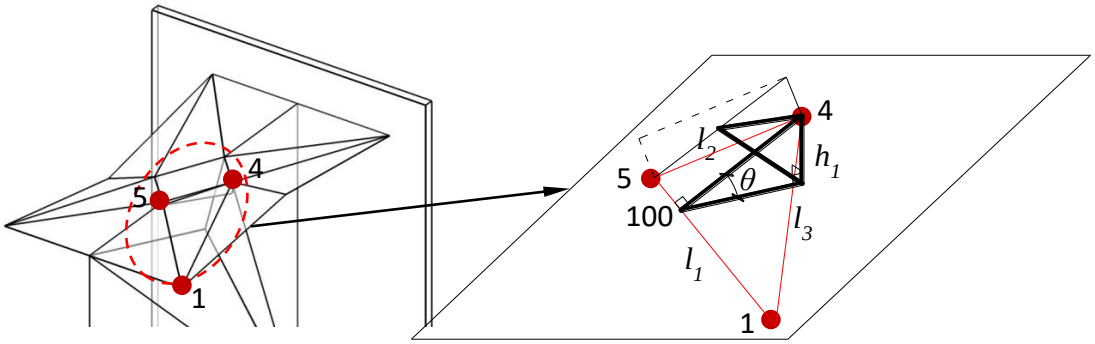

Figure 4-13 Deformed shape caused by bottom-flange buckling

The angle of rotation of Line 1-5 is

$$h_1 = l_{4\text{-}100}\sin(\theta) = \sin(\theta)\sqrt{l_2^2 - ((l_2^2+l_3^2-l_1^2)/(2l_3))^2} \tag{4-17}$$

The out-of-plane deflection of Point 11 (Figure 4-12 (a)) on the beam web, caused by bottom-flange buckling, is equal to h_1.

For the out-of-plane deflection caused by shear buckling, the initial length (as shown in Figure 4-13 (a)) of the compressive strut, which contains Point 11, is

$$l_4 = ((\beta + \gamma) / 2\beta) \times \sqrt{2}d \tag{4-18}$$

The deformed length of the same compressive strut is

$$l_5 = 2 \times ((\beta + \gamma) / 2\beta) \times d \sin(\pi / 4 - \theta_2 / 2) \tag{4-18}$$

The side lengths of the triangle, as shown in Figure 4-13 (b), are

$$x_2 = \sqrt{2}\gamma c \tag{4-20}$$

$$x_3 = l_4 - l_5 / 2 - x_2 \tag{4-21}$$

$$x_4 + x_5 = l_5 / 2 \tag{4-22}$$

According to the geometry, h_2 can be calculated as

$$h_2 = \sqrt{(x_3)^2 - ((x_3^2 - x_2^2 + (l_5 / 2)^2) / l_5)^2} \tag{4-23}$$

In summary, the calculation procedure for the analytical model of the combination of buckling modes is based on equality of the internal work in the buckling zone and the loss of potential of the externally applied load. The length of the buckling zone can be calculated according to Equation (4-1). It is assumed that yield lines and yield zones exist only within the buckling zone. The internal work done by the rotation about the yield lines and the squashing of the yield zones can be calculated according to Tables 4-1 and 4-2. The bending resistance reduction at each yield line due to its normal net compression has been considered. The relationship between the deflection angle ϑ_1 due to bottom-flange buckling and the angle ϑ_2 due to beam-web shear buckling can be derived by assuming displacement compatibility at Point 11 in Figure 4-12. For each

given ϑ_1, the corresponding ϑ_2 can be calculated. Therefore, the overall deflection can be calculated. The applied external load can be calculated according to the given ϑ_1. Therefore, a force-deflection relationship in the post-buckling stage can be determined.

4.3 VALIDATION AGAINST FINITE ELEMENT MODELLING

4.3.1 Validation of FE model against experimental results

The finite element software ABAQUS has been used to develop the finite element modelling. In this section, the FE models are validated against the experimental results published by Dharma (2007a).

Experimental programme

Dharma tested nine steel I-beams up to failure. In this research, four out of the nine I-beams have been chosen to validate the numerical models. All the nine I-beams in the tests failed in the combination buckling mode. Four specimens which demonstrated clear descending force-displacement relationships after the occurrence of local buckling have been selected to validate the FE model at the post-buckling stage. The test numbers for the four beam sections are S3-2, S3-3, S4-1 and S4-2. The test setup is shown in Figure 4-14. There is one stiffener at each end of the beam, as well as one at mid-span. No axial restraint was applied during the testing, so that no axial force was caused by thermal expansion. The specimens were heated to constant temperature before the hydraulic jack applied a static point load at the mid-span.

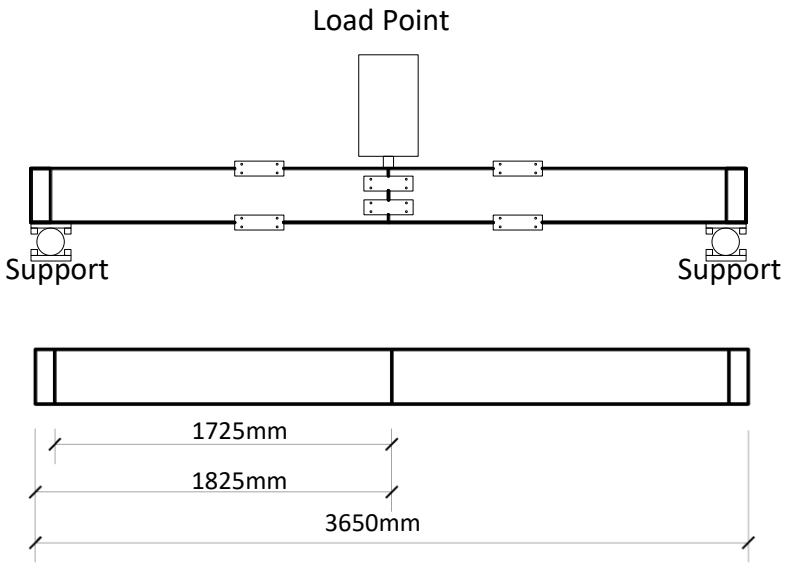

Figure 4-14 Test set-up (Dharma and Tan, 2008)

The results of the tensile coupon tests on these specimens at ambient temperature are given in Table 4-3.

Table 4-3 Results of tensile coupon tests at ambient temperature (MPa)

Beam No.		Yield Stress	Elastic Modulus	Ultimate Strength
S3-2	flange	224.1	201697	392.1
	web	277.1	206063	452.0
S3-3	flange	224.1	201697	392.1
	web	277.1	206063	452.0
S4-1	flange	393.5	205283	545.1
	web	449.4	205700	590.3
S4-2	flange	393.5	205283	545.1
	web	449.4	205700	590.3

These tests were used to validate the ABAQUS models, although the test setup was not identical to the exact conditions (restraint to thermal expansion, boundary conditions and the ratio of shear to moment in the buckling panel), which a real beam

would experience in a real fire. The validated FE models, subject to more realistic conditions, were then used to verify the analytical model.

Numerical modelling

In this study, the four-noded shell element (S4R) of ABAQUS, which is capable of simulating buckling behaviour with reasonable accuracy, was adopted. A mesh sensitivity analysis was conducted. Different mesh sizes were analysed. The mesh sensitivity results are shown in Figure 4-15. It has been shown that for mesh sizes smaller than 15mm x 15mm, the load-deflection results were nearly identical in the post-buckling stage. This indicated that elements of size 15mm x 15mm provided an optimum between accuracy and computing efficiency. Arc-length analysis (Hibbit *et al*., 2005) was carried out to track the descending load path of the buckling zone at the post-buckling stage. The shape of the initial imperfection was based on the first buckling mode. A small amplitude $(d + t_f)/100$ was adopted in order to trigger the asymmetric bottom-flange buckling mode without unduly influencing the load capacity of the buckling zone. Regarding the material properties used in the numerical modelling, the ambient-temperature coupon test results, as shown in Table 4-1, were reduced by applying the reduction factors for proportional limit stress, yield stress and Young's modulus, as given in BS EN 1993-1-2.

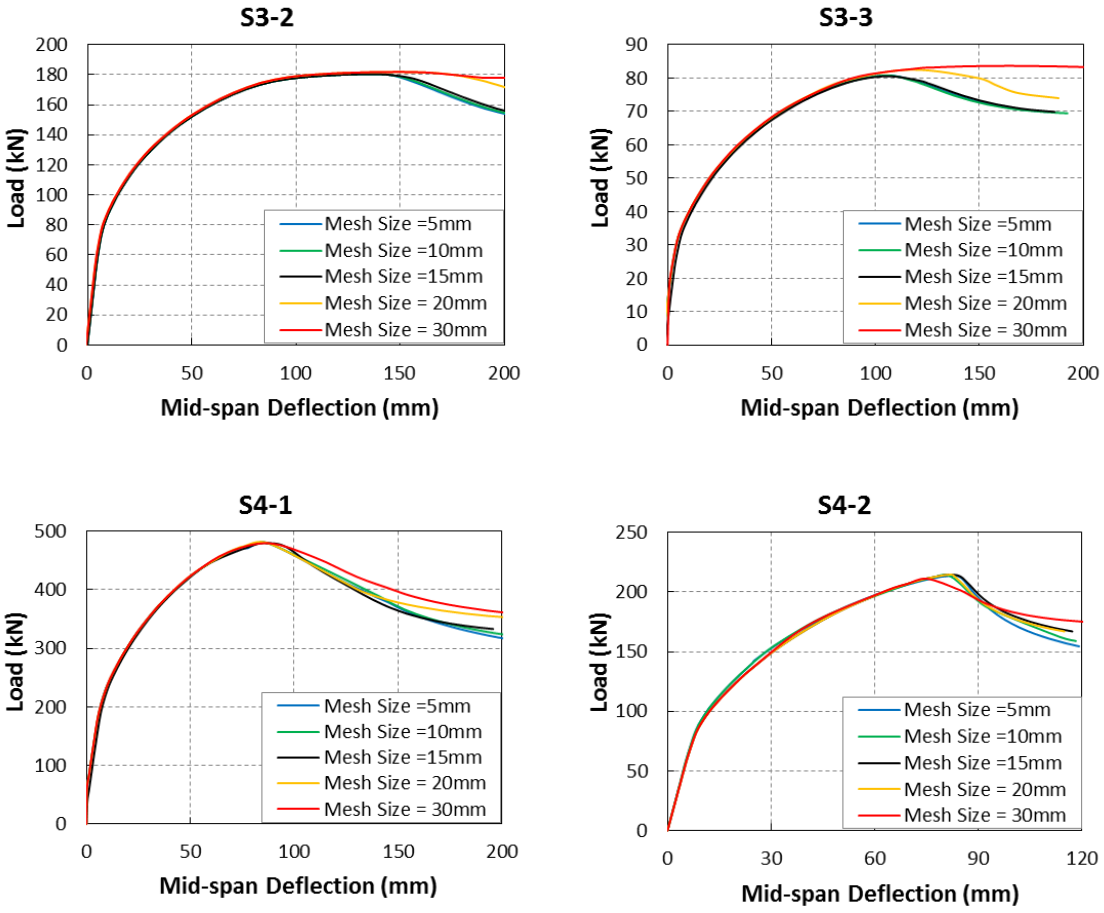

Figure 4-15 Mesh sensitivity analysis

The finite element model is illustrated in Figure 4-16. As the end supports were directly below the stiffeners, only the length of the beam between the two end stiffeners was modelled. The length of the model was 3450mm. Multi-Point Constraints (MPC) (Hibbit *et al.*, 2005) which allow constraint of the motion of slave nodes of a region to the motion of a point, were applied in ABAQUS between Points 1 and the left-end stiffener, as well as between Point 2 and the right-end stiffener. Boundary conditions were then applied to Points 1 and 2. For Point 1, all six degrees of freedom (DoF) were restrained except for rotation about the x-axis, whereas Point 2 was free to rotate about x and to move in translation parallel to z with the other DoFs constrained. In other words, the two beam ends could both rotate about x, and there

was no restraint to thermal expansion of the beam. MPC make it convenient to model pin-ended beams. A point load was applied to the mid-span of the beam. Table 4-4 presents the details of cross-section dimensions and test temperatures. All dimensions are the average values of measurements by Dharma (2008) from different locations.

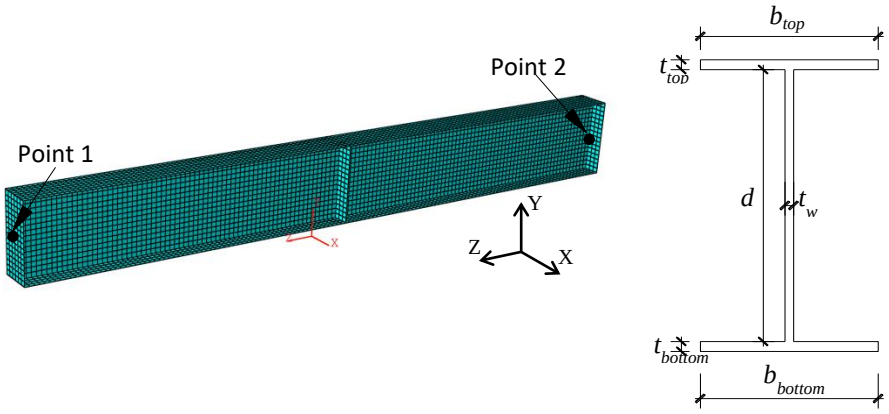

Figure 4-16 Finite element model. (a) Image of finite element model; (b) cross section dimensions (in mm)

Table 4-4 Measured cross-section dimensions (in mm) and test temperature (in °C)

Test No.	b_{top}	b_{bottom}	t_{top}	t_{bottom}	d	t_w	T
S3-2	162.89	163.51	10.00	9.95	275.5	8.14	415
S3-3	162.72	164.00	10.30	10.19	275.93	7.95	615
S4-1	176.70	178.26	10.08	10.46	380.76	7.83	415
S4-2	177.83	176.71	10.29	10.52	380.78	7.76	615

A comparison between the FE modelling and experimental results is shown in Figure 4-17. The lines represent the FE results while the data points represent test results. Good agreement between the test and the FE modelling results was obtained, except for S4-1, in which the FE model predicts lower capacity than that measured during testing. Since all the other three groups indicate good reliability of the FE models, the failure load given by Test S4-2 (same specimen as in Test S4-1, but tested at 615°C)

was used to predict the failure load of Test S4-1 (at 415 °C), using the strength reduction factors given in EUROCODE 3 (CEN, 2005b). This calculated failure load agrees with the modelling result. It is possible that the loading rate applied in Test S4-1 may have been too fast, resulting in an increase of the failure load, as has been experienced in other studies (Torić *et al*., 2014). The discrepancy between Test S3-2 and FEA S3-2 in the deflection range of 10 mm to 80 mm is possibly caused by the discrepancy between the real high-temperature mechanical properties of the tested steel and the properties used in the modelling (ambient-temperature coupon test results with the EUROCODE 3 reduction factors applied). The FE models can also predict well the buckling shape compared with the test results; one example is shown in Figure 4-18. Therefore, the numerical model is considered reliable and is used in the following study.

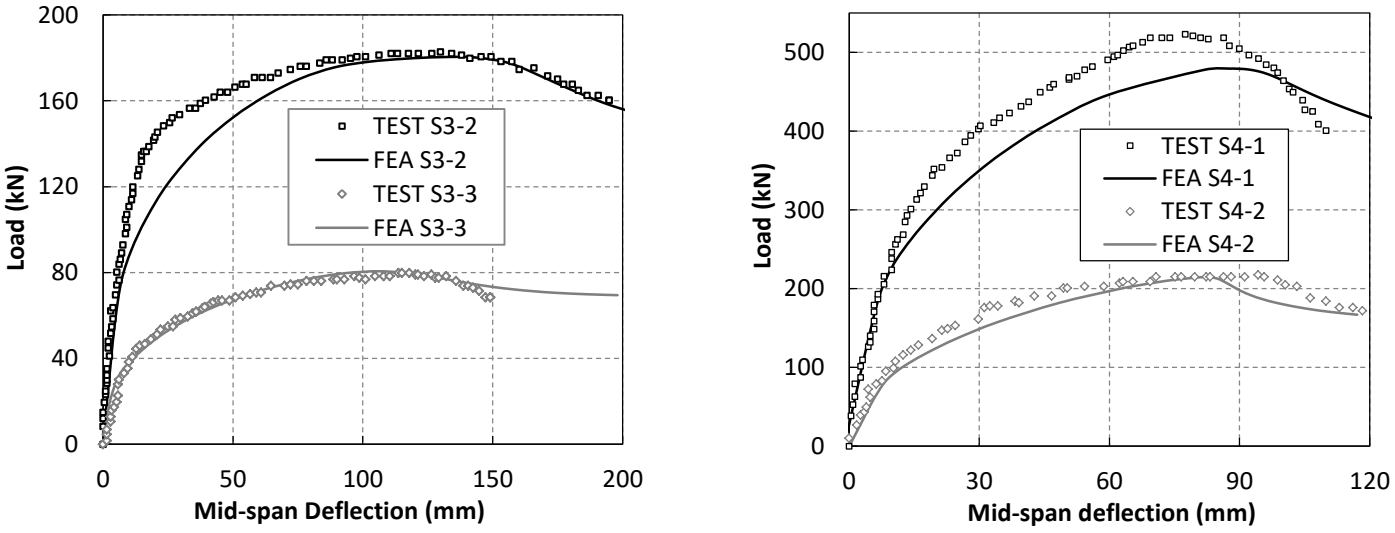

Figure 4-17 Load-deflection comparison between FEA and test results

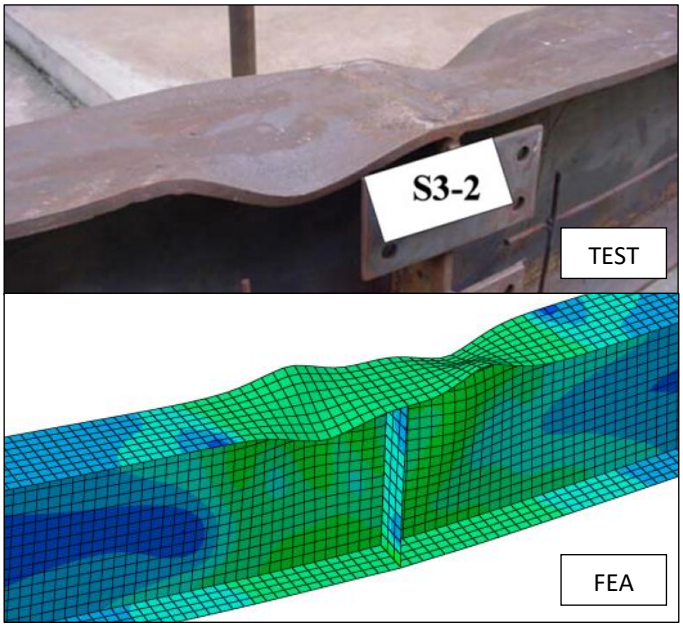

Figure 4-18 Comparison of failure modes of Test 3-2 (Dharma and Tan, 2008) and FEA

4.3.2 Comparison between the proposed analytical model, Dharma's model and FEA

Comparison 1

After validation, 48 FE models of various beam configurations and loading conditions were analysed at different temperatures. An illustration of an FE model, and its loading and boundary conditions, is shown in Figure 4-19. A short cantilever with the length/depth ratio equals to 2 was modelled. This length/depth ratio is chosen to ensure that (1) the model will include at least one full buckling wavelength, and (2) the effects of the boundary conditions can be minimised. The flexural curvature of this short beam-end buckling zone can be neglected. Different combinations of shear force and bending moment were applied, as shown in Table 4-5. The bending moment and the shear force were applied independently to the end of the short cantilever. By changing the combination of the shear force and the bending moment at the end of

the short cantilever, the model can represent any loading condition without uniformly distributed load on top of the buckling panel.

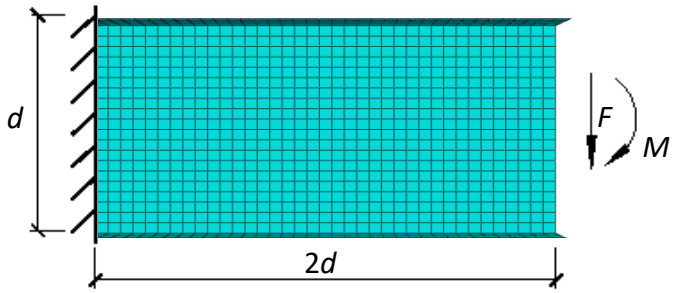

Figure 4-19 The finite element model

These cases have been divided into two groups, FEA1 and FEA2. The models in FEA1 are of the same dimensions as the specimen of Test S3-2 (Table 4-2), with web thicknesses varying between different models. Similarly, FEA2 uses the Test S4-2 specimen dimensions, again with different web thicknesses. Since this research focuses on Class 1 and 2 sections, the variation of web thicknesses is limited within this range. Temperatures of 415°C and 615°C have been applied. The material properties of the flanges of the test specimens S3-2 and S4-2 have been used for FEA1 and FEA2 models, respectively.

Table 4-5 Detailed group information

	Web thickness	Moment-shear force ratio *M*/*F* (in mm)	Temperatures (°C)	
FEA1	5mm	500 1000 1500	415	615
	6mm	500 1000 1500	415	615
	7mm	500 1000 1500	415	615
	8mm	500 1000 1500	415	615
FEA2	5mm	500 1000 1500	415	615
	6mm	500 1000 1500	415	615
	7mm	500 1000 1500	415	615
	8mm	500 1000 1500	415	615

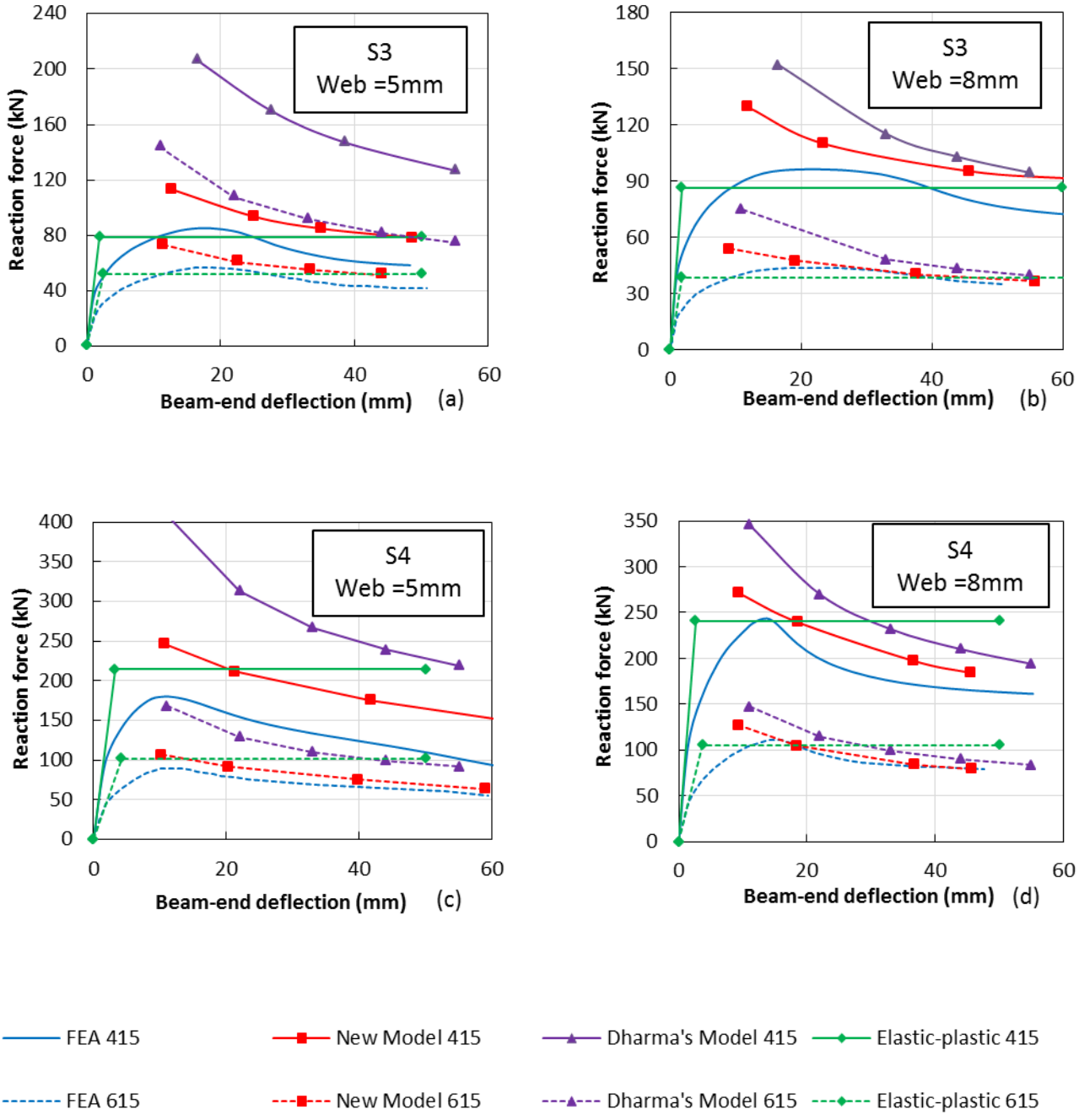

Figure 4-20 Comparison between the analytical model, Dharma's model and FE analysis

The force-displacement relationships given by the proposed analytical model, Dharma's model and the ABAQUS analyses have been compared. Figure 4-20 shows the comparisons for the two models with the largest and smallest web thicknesses (5mm and 8mm) subject to bending and shear force at *M/F* = 1000mm. Each part of

Figure 4-20 includes eight curves, representing the comparison between the analytical model, Dharma's model, FE analysis and the elastic-plastic curve (with peak loads assessed by assuming plastic moment resistance is reached at the middle of the flange buckling zone) at two different temperatures. The proposed analytical model gives upper-bound results compared to the FE models for all cases; it also gives more accurate results than that of the Dharma's model in all cases. The results from Figure 4-20 show that the maximum flexural capacity $F_{\max}$ of an I-beam is generally less than 10% above the vertical force $F_{p,T}$. The analytical model captures results for beams at 615°C better than at 415°C. This may be because the accuracy of the assumption of flange buckling length from Eq (4-1) may differ at different temperatures; this would have a significant effect on the beam post-buckling behaviour. Figure 4-21 shows a comparison of the force-web-thickness relationships between the new model and Dharma's model. The variable F_{FEA} represents the peak load given by the FE modelling. F_N and F_D respectively represent the load level of the new analytical model and that of Dharma's model, at the deflection at which the FEA model reaches its peak load. The vertical axis of Figure 4-21 represents F_N and F_D normalized with respect to the corresponding F_{FEA}. As shown in this figure, Dharma's model tends to overestimate the beam loading capacity when the web is thinner (of 5mm or 6mm thickness), whereas it gives a good prediction at larger web thicknesses (7mm and 8mm). The new analytical model is able to give a better upper bound of the beam load capacity for both slender and stocky beams within the analysed range. The proposed analytical model has been designed for Class 1 and 2 sections, whereas the two models of web thicknesses 5mm and 6mm in FEA2 fall into the Class 3 range. This explains the reason for the larger discrepancy between the proposed model and the FEA for these two

cases. It is, therefore, indicated that the new model gives a reasonable prediction of the load capacity of the beam end buckling zones of Class 1 and 2 sections at the post-buckling stage.

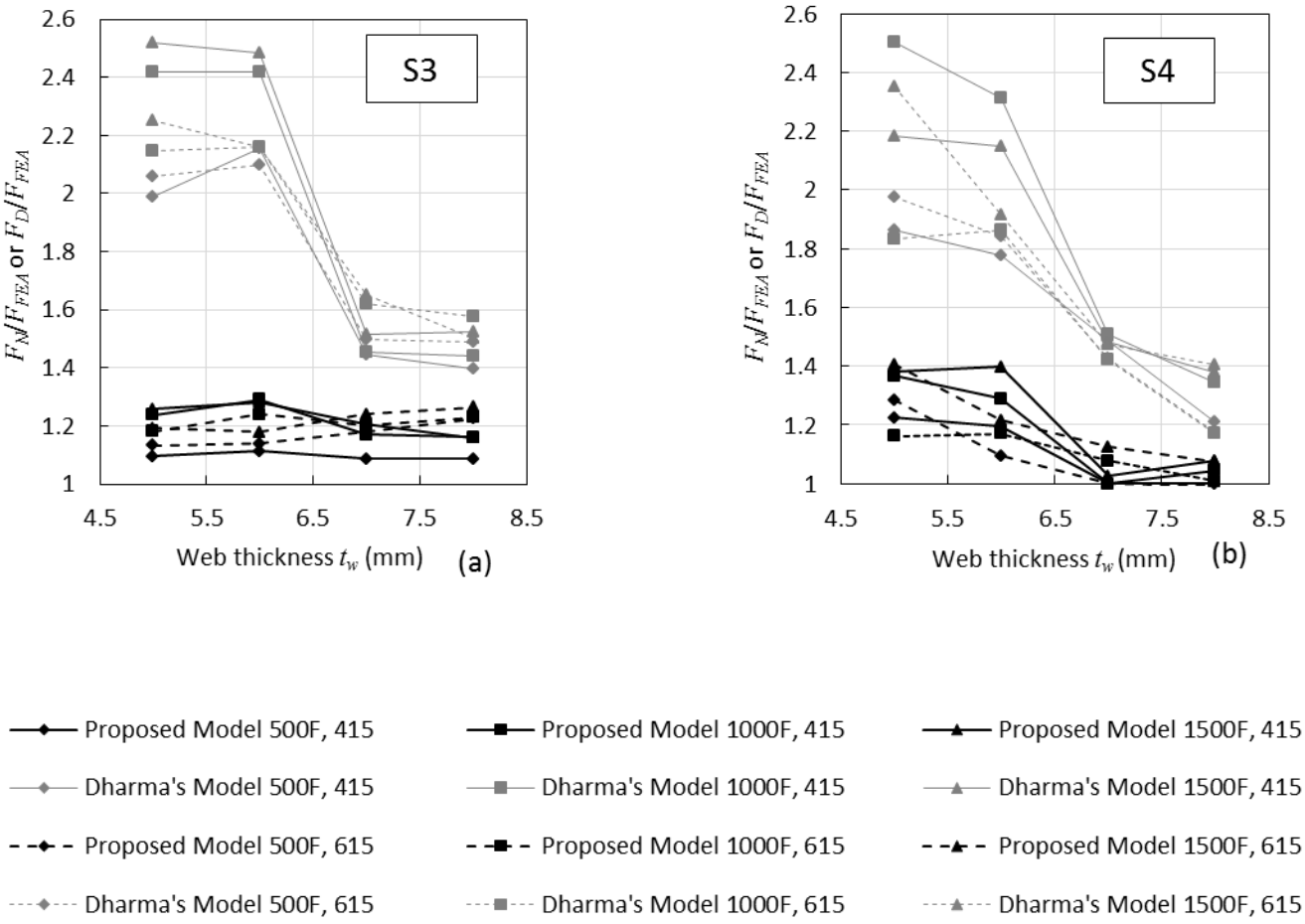

Figure 4-21 Comparison of predictions of the new model and Dharma's model: (a) FEA1; (b) FEA2

Comparison 2

Further parametric study and validation of the proposed analytical model have been carried out in this section for a group of beams with different cross-section dimensions from Section 4.3.2. The development of the analytical model is explained using a short cantilever I-beam section (Figure 4-22) as an example. By changing the cantilever

length and by applying different combinations of uniformly distributed load and shear force at the beam-end, the cantilever is able to represent part of a fixed-ended beam from its end to the point of contraflexure under a uniformly distributed load. It can be calculated that the distance from one end of the beam to its adjacent contraflexure point is equal to 0.2113 of the whole beam length.

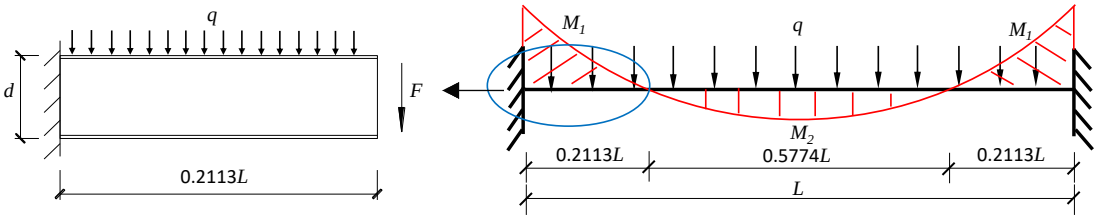

Figure 4-22 The analytical model

The results of the analytical model were compared with Dharma's model and FEA. The same methodology of the analytical was applied as introduced in Section 4.2. The commercial finite element software ABAQUS was used to simulate the buckling phenomena in the vicinity of beam-column connections at 615°C. The four-noded shell element S4R was adopted. A 15mm x 15mm element size was used, after a mesh sensitivity analysis. The Riks approach was used in order to identify the descending curve at the post-buckling stage. Cantilever models with one beam end fully fixed while free on the other end were set up. An image of the ABAQUS model is shown in Figure 4-23 (a). The cross-section dimensions are shown in Figure 4-23 (b). All the cantilevers shared the same configuration except for the beam web and flange thicknesses. The beam cross-section dimensions were based on the universal beam UB356x171x51, whose beam web and flange thicknesses are 7.4mm and 11.5mm respectively. As the analytical model applies generally to Class 1 and 2 sections, the thicknesses of the beam webs and flanges vary within this range. Therefore, the

thicknesses of the beam webs were varied from 5.5mm to 8mm, while those of the beam flanges were varied between 10mm and 13mm. In the cases validated, the potential beam length was 6m, on the basis that a beam depth-to-length ratio of 1/20 is commonly used in design practice. The cantilever length was 1267.8mm, which is identical to the distance from the beam-end to its adjacent contraflexure point. The shear force applied to the beam-end was 1732.2*q*, which enabled the cantilevers to be in the same loading condition as the corresponding end zones of the 6m fixed-ended beams.

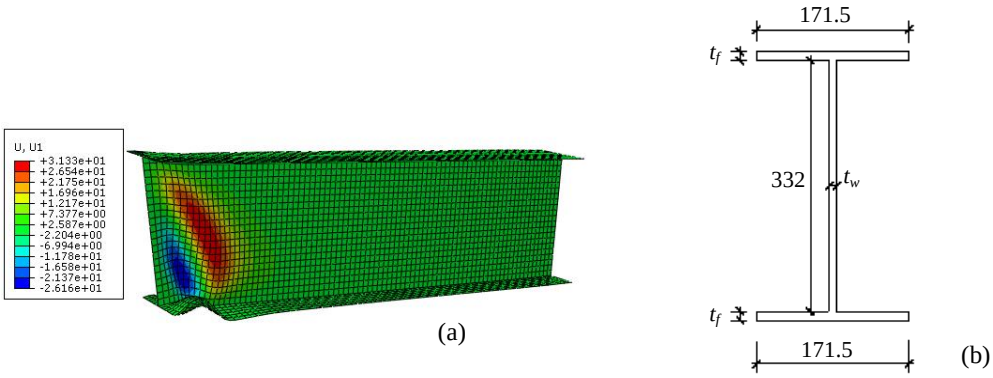

Figure 4-23 Finite element model: (a) image of finite element model; (b) cross-section dimension

The details of the material properties used in the ABAQUS models are shown in Table 4-6.

Table 4-6 Material Properties

$f_{y,\theta}$ (N/mm^2)	$\varepsilon_{y,\theta}$ (%)	$\varepsilon_{t,\theta}$ (%)	$\varepsilon_{u,\theta}$ (%)	$E_{\alpha,\theta}$ （N/mm^2）
224.1	2	15	20	201697

The force-displacement relationships given by the proposed analytical model, Dharma's model and the ABAQUS analyses have been compared. The first group of

beams compared have the same flange thickness of 11.5mm, while their web thickness varies. The detailed curves are shown in Figure 4-24. The lines with diamond markers, denoted "Elastic-plastic", represent the force-deflection relationships when the full plastic moment resistance is reached at the middle of the flange buckling zone. The smooth lines without markers represent the results of finite element modelling. The descending solid and dashed lines are the results from the new proposed buckling model and Dharma's model respectively. It can be seen that both the proposed analytical model and Dharma's model give very good comparisons to the FE modelling for beams with thicker webs. The proposed model is able to provide acceptable results for beams with webs within the Class 3 range. However, Dharma's model tends to over-estimate the beam capacity considerably for those with more slender webs.

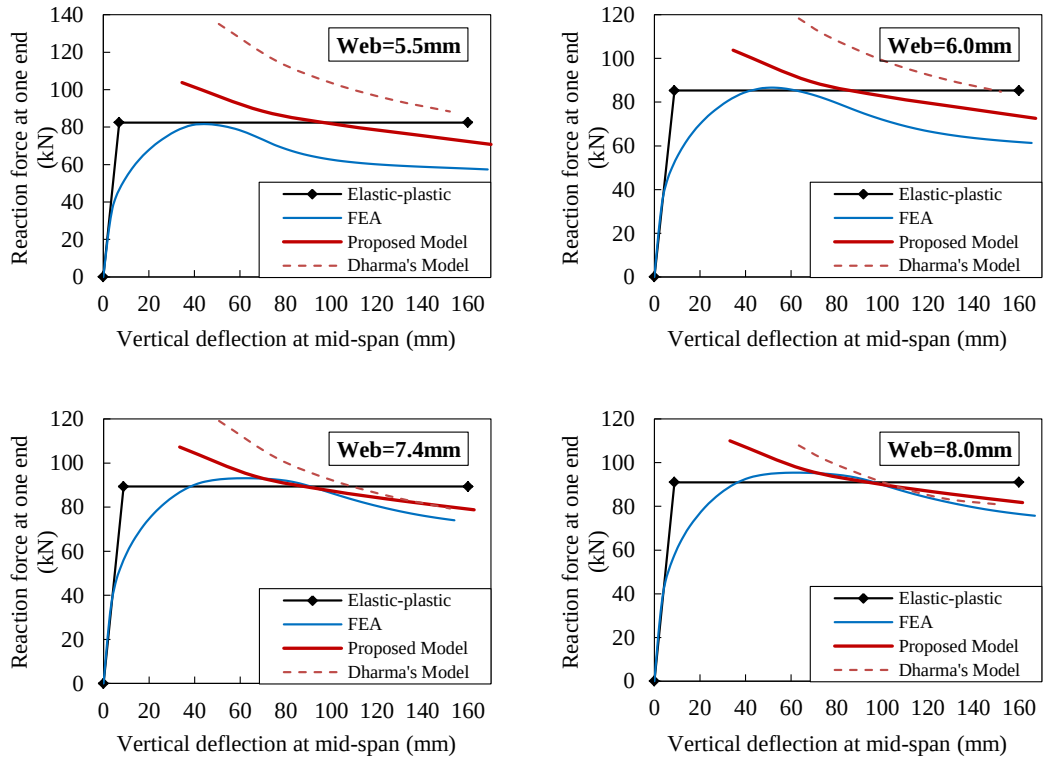

Figure 4-24 Comparison between the analytical model, Dharma's model and FE analysis (web thickness varies)

Figure 4-25 shows the second group of comparisons, for which the beam web thickness remains at 7.4mm, and the flange thickness varies between 10.0mm and 13.0mm to guarantee that the beam classification lies in the Class 1 to 2 range. It can be seen that the proposed analytical model compares well with beams within all the selected flange thicknesses, while Dharma's model over-estimates the capacity for beams with stocky flanges. This is possibly because the length of the buckling zone is related to the ratio between t_f and t_w according to Equation(4-1). Decreasing the web thickness or increasing the flange thickness can both increase this ratio. Dharma's model seems more sensitive to the flange-to-web thickness ratio, and therefore considerably over-estimates the capacity when this ratio increases.

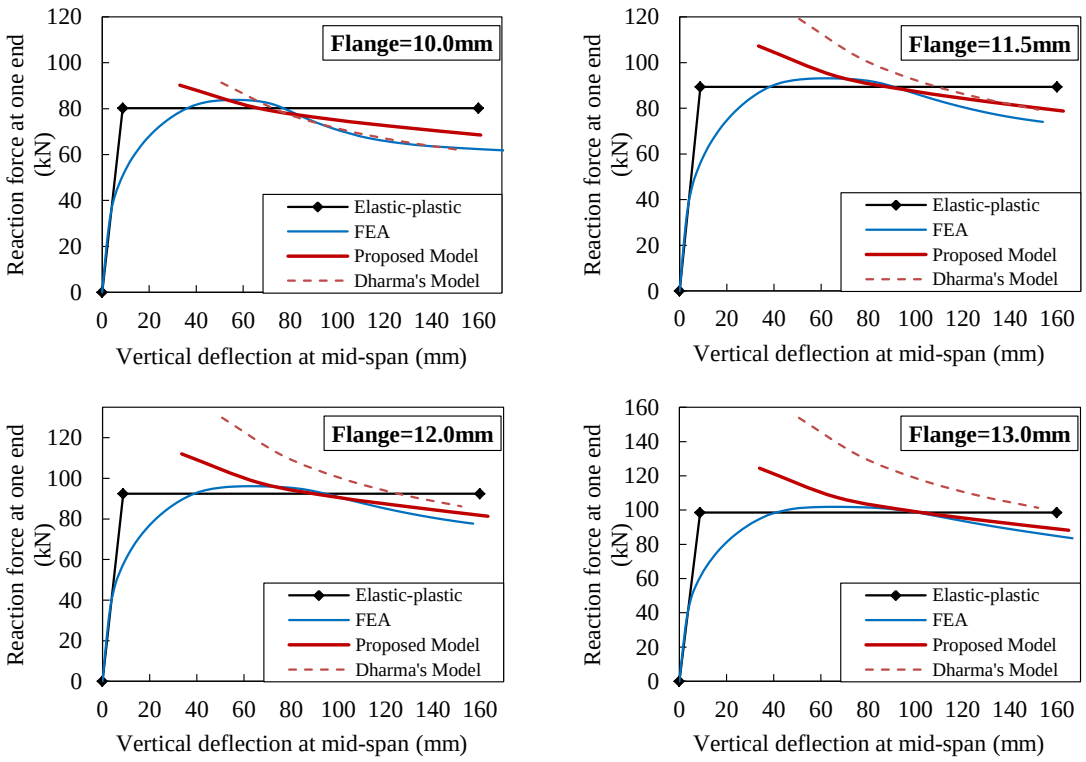

Figure 4-25 Comparison between the proposed analytical model and Dharma's model (flange thickness varies)

4.3.3 Integration into a full beam model

In this section, the validated beam-end model, as described in Section 4.3.2, has been integrated into a whole beam. The results of the integrated analytical model are compared with the results from ABAQUS modelling. A "whole curve" can be found to represent the force / mid-span deflection relationship of the beam including the beam-end buckling panel. A calculation example is given below.

In this example, the beam-end model of 8mm web thickness in Group FEA1 in Section 4.3.2 is selected and integrated into the full beam model. The length of the beam model is 5m, given that a beam depth to length ratio of 1/20 is commonly used in design practice. A vertical point load is applied at the mid-span of the beam. The beam is fully fixed against rotation at both ends, with one end being free to move axially to allow thermal expansion. The beam is heated to 615°C, the same as for the corresponding beam-end model. One half of the beam is modelled in ABAQUS, using symmetry boundary conditions. The contours of out-of-plane deflection are shown in Figure 4-26 (a). In the hand-calculating analytical model, the deformed shape is shown in Figure 4-26 (b). For this loading condition, the hogging moment at the beam end is identical to the sagging moment at the mid-span. Therefore, top-flange buckling at the mid-span occurs simultaneously with bottom-flange buckling at the beam end. Beam-web buckling occurs at both the beam end and mid-span. The mid-span deflection (Δd) consists of twice the sum of (1) the deflection Δd_1 due to the beam-end rotation caused by bottom-flange buckling, (2) the transverse drift Δd_2 due to shear buckling and (3) the deflection Δd_3 due to normal bending curvature of one quarter of the beam.

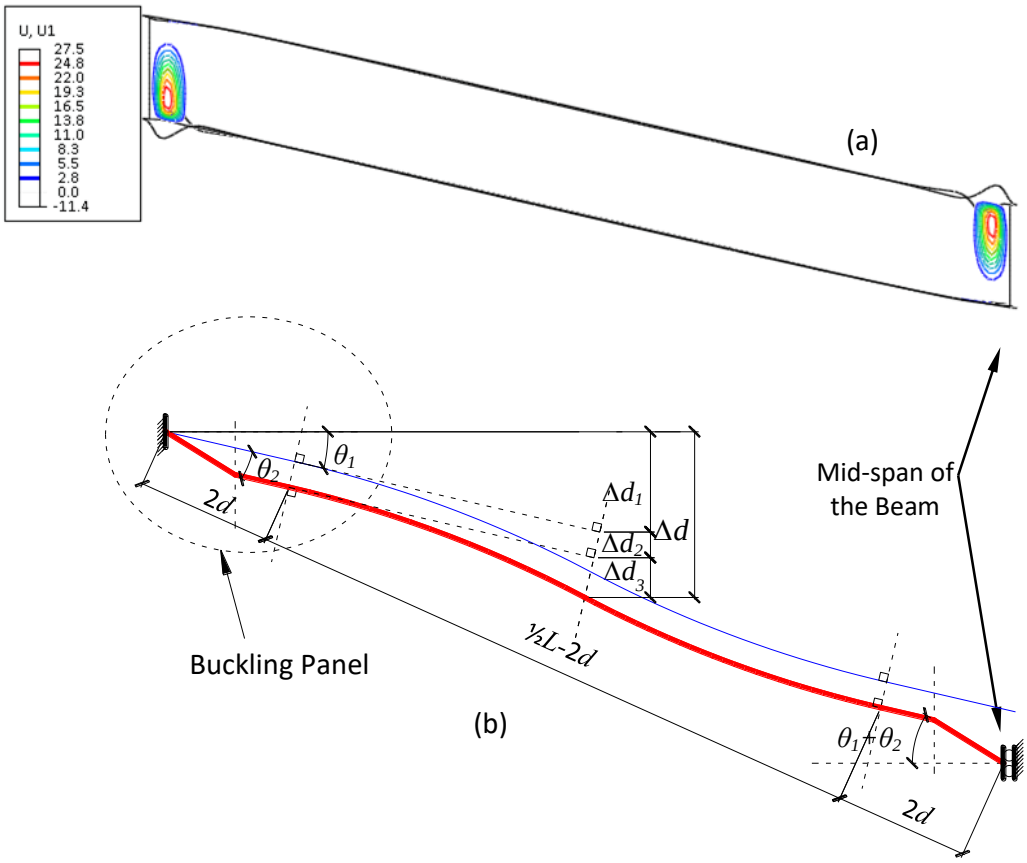

Figure 4-26 Deformed shape: (a) ABAQUS contour; (b) Simplified theoretical deformed shape

The force-deflection relationships given by the FEA and the analytical models are shown in Figure 4-27. The curve with triangular markers plots the results given by the analytical model which was developed to simulate the post-buckling behaviour, and the dashed line represents the FE results. The comparison shows that the proposed analytical model provides reasonably accurate and upper-bound results for a whole beam in the post-buckling stage. In the analytical model, a flat line has been drawn as the relationship between the vertical beam-end reaction force and mid-span deflection in the plateau stage. The force value corresponding to the plateau is the beam-end reaction force at which the beam-end plastic moment is reached. In the post-buckling stage the result from the analytical model is used. In the pre-buckling

stage, the result from FE analysis is used, as the pre-buckling stage is not the object of this analysis. Therefore, the thick line indicates the whole force-deflection relationship of the example beam with buckling zones, covering all three stages.

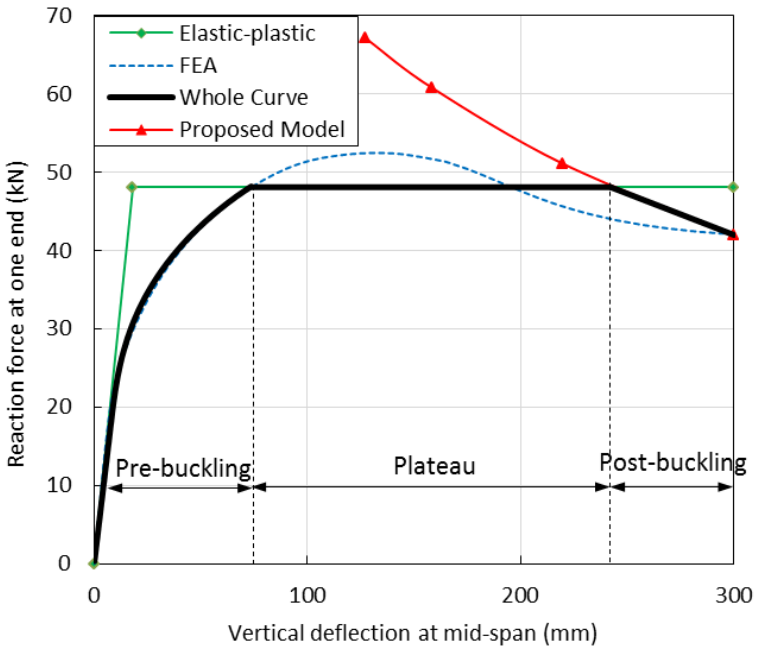

Figure 4-27 Force-deflection relationship of the example beam

4.4 CONCLUSION

The buckling behaviour of the beam-end bucking zone of a steel beam exposed to elevated temperatures involves three stages: non-linear pre-buckling, plateau and post-buckling. The behaviour of the non-linear pre-buckling stage is identical to normal beams. In the plateau stage, the ultimate load capacity of the beam-end buckling zone is assumed to be identical to its plastic bending moment resistance. This chapter presents a new analytical model to predict the post-buckling behaviour so that a complete force-deflection relationship of the beam-end bucking zone can be achieved.

The proposed analytical model considers both the beam-web shear buckling and bottom-flange buckling. The interaction between these two buckling modes is accounted for by ensuring compatibility between the out-of-plane deflections of the beam web caused by these two modes. A range of finite element models has been created using ABAQUS. These models were firstly validated against test data, and subsequently used to validate the analytical model. The analytical model has also been compared with Dharma's analytical model and FEA. Two comparison cases, considering both with and without uniformly distributed load on top of the buckling panel were discussed. The comparisons have shown that the proposed model provides a reasonably accurate and conservative prediction of the force-deflection relationship for Class 1 and 2 sections, whereas Dharma's model tends to overestimate the post-buckling capacity for beams with slender webs.

A calculation example of the validated beam-end buckling panel integrated into a whole beam was given. This example indicated that the analytical model is of sufficient accurate to be implemented into whole-beam analysation.

5.

A PARAMETRIC INVESTIGATION OF THE TRANSITION LENGTH BETWEEN BEAM-WEB SHEAR BUCKLING AND BOTTOM - FLANGE BUCKLING AT ELEVATED TEMPERATUR

5.1 INTRODUCTION

Analytical models have been proposed to track the force-deflection behaviour when pure shear buckling behaviour of the beam web occurs (Chapter 3), or beam-web shear buckling and flange buckling occur simultaneously (Chapter 4) at elevated temperatures. It has been pointed out in Chapter 3 that as beam length increases, the 'failure' mode switches from beam-web shear buckling to bottom-flange buckling. Therefore, a transition criterion is needed in order to justify whether beam-web shear buckling or a combination of beam-web shear buckling and bottom-flange buckling will actually occur according to the structural information of a particular case. The purpose of this criterion is to find the transition beam length, below which shear buckling will occur; a combined buckling mode will occur if the actual beam length is longer than the transition length defined by the transition criterion. The transition criterion is that, as beam length increases, the lesser resistance of the two buckling modes will be reached first. For the beam-web buckling mode the resistance is the plastic shear resistance, while for the combined buckling mode the resistance is the plastic bending resistance. The buckling mode corresponding to the lower of these is the real buckling mode.

In this section, the transition criterion of the occurrence between shear buckling and the combination of beam-web shear buckling and bottom-flange buckling has been proposed for beams without axial restraint. The cross-section dimension from Section 4 Group FEA1 will be verified against the criterion.

5.2 CALCULATION PROCEDURE TO DETECT THE TRANSITION LENGTH

It has been proved based on a number of investigations (in Chapter 3) that the real structural resistance is very close to plastic shear capacity when shear buckling occurs plastically for Class 1 to Class 2 sections. The bottom-flange buckling theory can be constant to the real structural resistance when bottom-flange buckling occurs. Therefore, either shear buckling or bottom-flange buckling occurs when the real load reaches plastic shear resistance or plastic bending moment resistance first. The calculation procedure to detect the transition from beam-web shear buckling to bottom-flange buckling is shown in Figure 5-1.

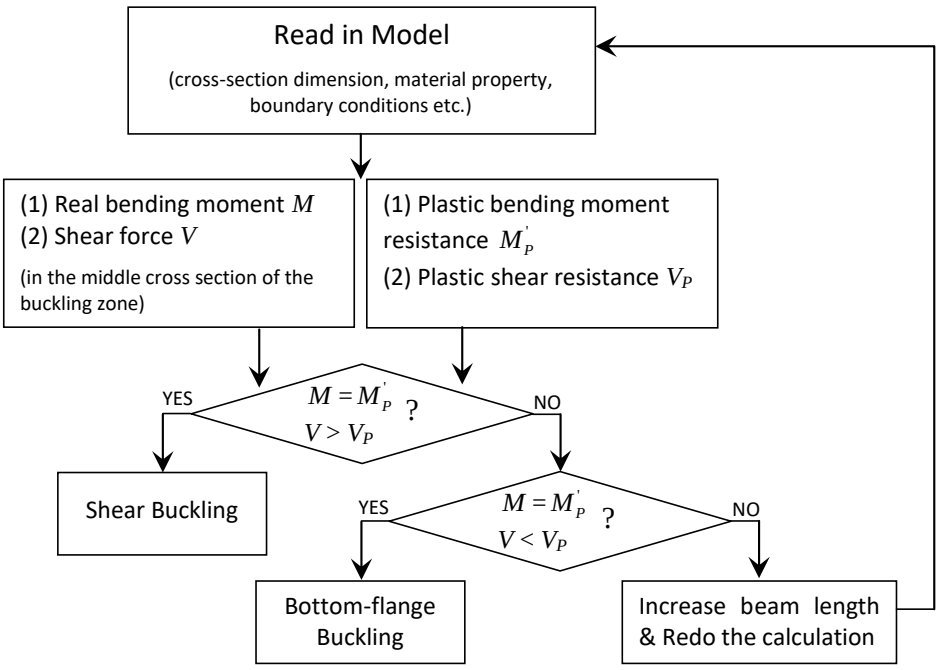

Figure 5-1 Flowchart of calculation procedure of the buckling transition criterion

It is worth noticing that in the flowchart, the plastic bending moment resistance $M_p^{'}$ considers the effect of shear force on the moment resistance if the shear force is more than half of the plastic shear resistance, according to Eurocode 3 (CEN, 2006).

According to the calculation procedure, the plastic shear resistance is given as Equation (5-1),

$$V_p = A_v(\sigma_{y,\theta} / \sqrt{3}) / \gamma_{M0} \quad (5\text{-}1)$$

Where A_v is the shear area.

The plastic bending moment resistance considering the effect of then shear force is,

$$M_p^{'} = (1-\rho)M_p \quad (5\text{-}2)$$

Where M_p is the normal plastic bending moment capacity of the cross section. ρ can be expressed as Equation (5-3) according to Eurocode 3 (CEN, 2005a).

$$\rho = \left[2V_{Ed} / V_p - 1\right]^2 \quad (5\text{-}3)$$

Where V_{Ed} is the elastic shear resistance of the cross section.

5.3 VALIDATION AGAINST ABAQUS MODELS

Two groups of ABAQUS models were developed in order to verify the beam-web shear buckling model, bottom flange buckling model as well as the transition length between these two buckling phenomena at 415°C. A summary of cross-section dimensions and material properties of both groups are shown in Table 5-1.

Table 5-1 Cross-section dimensions of the beams analysed

Group No.	*d*	*b*	t_w	t_f
A&B	275.5	163	7	10
Group No.	$\sigma_{y,\theta}$ (N/mm^2)	$\varepsilon_{y,\theta}$ (%)	$\varepsilon_{t,\theta}$ (%)	$\varepsilon_{u,\theta}$ (%)
A&B	267.96	2	15	20

For Group A, cantilever beams with the lengths from 750mm to 2000mm were analysed. For Group B, fully restrained beam with lengths from 2000mm to 6000mm were analysed. Only the part from one end to the point of inflection for both Group B were modelled in order to avoid the influence of the bending moment curvature. Uniformly distributed load was applied to both the two Groups. For Group B, an additional shear force, which was transferred from the other connected part of the beam, was applied to the end of the ABAQUS model. The ABAQUS image, the loading conditions and boundary conditions for Group A and B are shown in Figure 5-2. The ABAQUS models were firstly heated to 415^{o}C uniformly, and then load was applied to the beams until buckling phenomena occurs. Static-riks approach was carried out in the post-buckling stage to track the post-buckling descending force-deflection relationship.

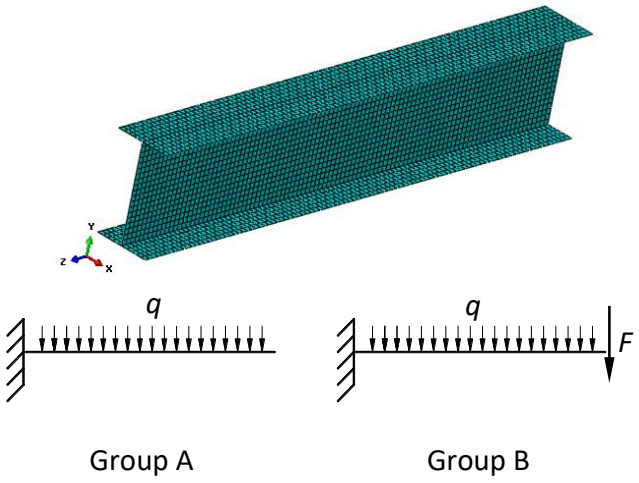

Figure 5-2 ABAQUS image, loading conditions and boundary conditions of Group A&B

5.3 COMPARISON WITH THE ANALYTICAL MODEL AND TRANSFER CRITERION

The calculation was carried out on the beam-web shear buckling analytical model and bottom-flange buckling model for Group A and Group B. The results for Group A are shown in Figure 5-3.

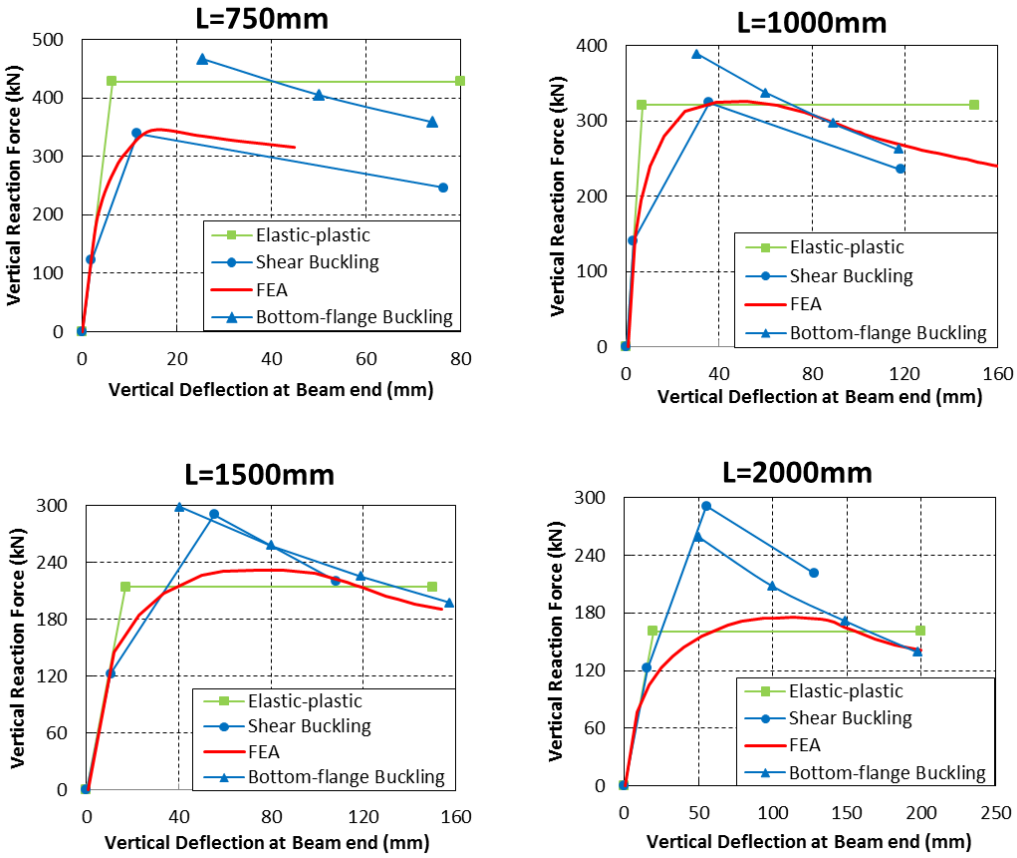

Figure 5-3 Comparison between the analytical and FE models for Group A

Four lengths from 750mm to 2000mm with the same cross-section dimension were analysed on cantilevers. The square-marked line, which is called Elastic-plastic, represents the force-deflection relationship when plastic bending moment resistance is reached at the middle line of the buckling zone. The length of the buckling zone is always considered to be identical to beam depth as this assumption largely simplifies

the calculation without influencing much of the accuracy. The smooth line without any marker represents the result of finite element modelling. The lines with round markers and triangle markers are the results from pure shear buckling theory and bottom-flange buckling theory respectively. The finite element result can be regarded as the real situation. It can be found that for 750mm beam, the shear buckling curve compares well with the FEA result. They are both below the elastic-plastic curve. The bottom-flange buckling result is far above the FEA modelling. As the shear buckling curve is below the bottom-flange buckling result, it is indicated that beam-web shear buckling is the actual buckling mode, as the plastic shear resistance will be reached before the actual bending moment reaches the plastic moment resistance. The good comparison between the force / deflection curves for the analytical beam-web shear buckling mode and FEA modelling indicates that the analytical model is accurate enough to represent the shear buckling behaviour. This is an extra validation of the approach presented in Chapter 3. As the cantilever length goes to 1000mm, both the shear buckling result and FEA result start to approach the Elastic-plastic curve meeting with the bottom-flange buckling analysis. This is the transition phase when the buckling mode transfers from beam-web shear buckling to bottom-flange buckling. For cantilevers with the length of 1500mm and 2000mm, both the FE results and bottom-flange buckling theoretical results remains around the Elastic-plastic curve. The two results compare to each other well, while the shear buckling analytical result starts to go above the FEA and bottom-flange buckling curve. This indicates that bottom-flange buckling is the buckling mode for the 1500mm and 2000mm cantilevers. For this cantilever cross-section dimension, the transition length should be around 1000mm

according to the results comparison. This conclusion can also be proved by the ABAQUS result visualizations shown in Figure 5-4.

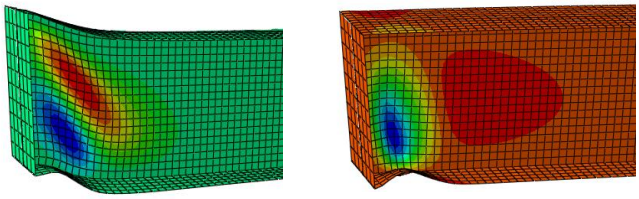

(a) L=750mm (b) L=2000mm

Figure 5-4 ABAQUS result visualization of Group B (a). L=750mm; (b). L=2000mm

According to the transition criterion, the calculating transition length from this procedure is 1036mm. This is consistent to that achieved from the FE analysis visualization and the comparison between the analytical models and the FE analysis.

The other group (Group B) of full-restrained beam examples were analysed. The results are shown in Figure 5-5. Similar observation to Group A was carried out on Group B results. It can be seen that the transition length of this group is around 3000mm. The ABAQUS result visualizations shown in Figure 5-6. The ABAQUS visualization of shear buckling mode of 2000mm beam in Group B is shown in Figure 5-6 (a); the visualization of combination buckling mode of 6000mm beams if shown in Figure 5-6 (b).

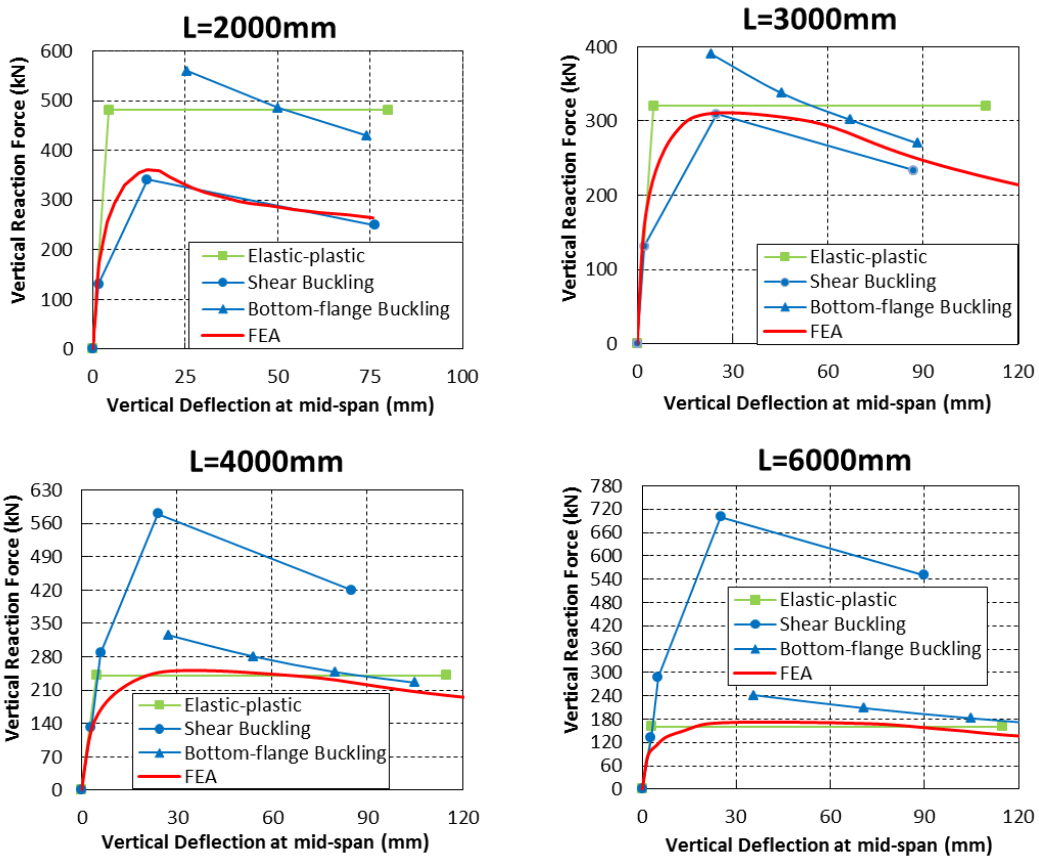

Figure 5-5 Comparison between the analytical and FE models for Group B

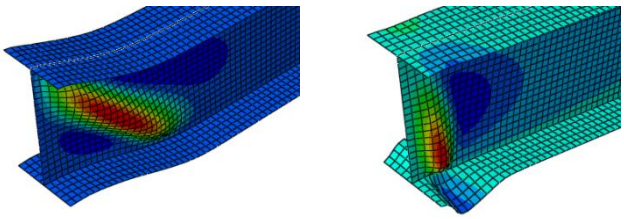

(a) L=2000mm (b) L=6000mm

Figure 5-6 ABAQUS result visualization for Group B (a). L=2000mm; (b). L=6000mm

The transition length calculated from the calculating procedure is 3485mm, which compares well with the FE analysis and the analytical models again. According to the three group of examples analysed, it can be suggested that the proposed transition

criteria is an easy and effective way to detect the transition length of the beams given the structural information.

5.4 CONCLUSION

The primary goal of this chapter is to create a transition criteria and the corresponding calculation procedure to detect the transition length between pure beam-web shear buckling and the combination of beam-web shear buckling and bottom-flange buckling effectively.

Two groups of beams with analysed using the finite element software ABAQUS and the existing analytical model for beam-web shear buckling and bottom-flange buckling respectively. It was observed in the result comparison that when beam length is shorter than the transition length, shear buckling is the dominant buckling mode. The bottom-flange buckling analytical results are above the shear buckling curve and the FE results, indicating that bottom-flange buckling cannot occur. When the beam length is longer than the transition length, bottom-flange buckling is the dominant buckling mode. The bottom-flange buckling analytical results compare well with the FE analysis. The shear buckling analytical result is above the other two curves. For the beams with length around the transition criteria, the FEA, shear buckling and bottom-flange buckling results tend to be identical. The transition lengths observed from the FE modelling and the comparison between the analytical models to the FE models show consistency to the transition length according to the calculation criteria for the two groups of beams analysed. Therefore, the calculation criteria can be a simplified and effective way to detect the transition length between beam-web shear buckling and bottom-flange buckling of the beams given structural information.

After the buckling mode and the transition length have been determined, it is possible to decide analytically the overall behaviour of the buckling panel. If the buckling mode is shear buckling, the force-deflection path follows the trilinear curve representing the beam-web shear buckling behaviour from the pre-buckling stage to the post-buckling stage. If the buckling mode is the combined mode, the force-deflection path is linearly elastic until the vertical reaction force at which the plastic bending moment resistance occurs is reached. The elastic range is followed by a plateau stage, and finally by the post-buckling stage, for which the force-deflection path is determined by the analytical model introduced in Chapter 4.

6.

THE BEHAVIOUR AND EFFECTS OF BEAM-END BUCKLING IN FIRE USING A COMPONENT-BASED METHOD

6.1 INTRODUCTION

Previous work conducted has led to the development of an analytical model which can consider the combination and interaction of flange buckling and beam-web shear buckling. Further parametric studies have indicated that this model is sufficiently accurate to reflect the most important aspects of the buckling zones in the vicinity of beam-to-column-face connections at elevated temperatures. In this chapter, a component-based model of the buckling zone has been created on the basis of this analytical model. Each nonlinear spring in the buckling element is able to deal with the reversal of spring deformation, to simulate strain reversal, which very often happens within a heated structure and must therefore be considered during modelling. The component-based buckling element has been implemented into Vulcan. It has been verified against ABAQUS modelling on isolated beams. The influence of the buckling element on the bolt-row force redistribution within the connection has then been investigated in isolated beam case and a two-storey two-span plane frame.

6.2 CREATION OF THE COMPONENT-BASED MODEL

According to the analytical model, the force-deflection characteristics of the buckling element can be divided into three stages, described as pre-buckling, plateau and post-buckling. In the pre-buckling and plateau stages, the buckling element performs as an ordinary beam element. In the post-buckling stage, the deflection of the buckling zone is the sum of the deflection due to beam-web shear buckling and that caused by bottom-flange buckling. The bottom-flange buckling causes an additional rotation of the whole beam-end about its support (due mainly to local shortening of the bottom flange in buckling), as shown in Figure 6-1 (a). It is assumed that the centre of rotation is at the top corner of the beam-end (Point A in Figure 6-1 (a)), since the resistance of

the bottom flange decreases after buckling. Beam-web shear buckling can cause transverse drift of the shear panel, as shown in Figure 6-1 (b). Therefore, the combined effect of flange buckling and beam-web shear buckling on the overall vertical deflection of the beam is as illustrated in Figure 6-1 (c).

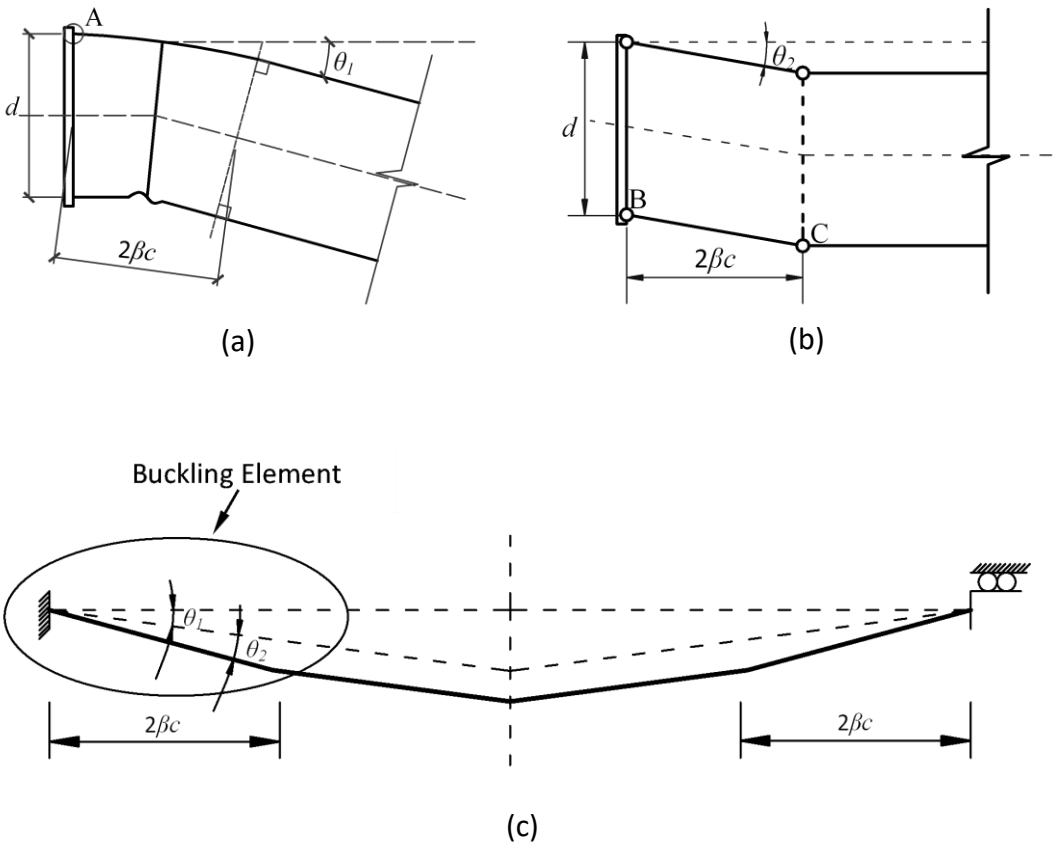

Figure 6-1 The effects of (a) bottom-flange buckling, (b) shear buckling and (c) total deflection on beam vertical deflection.

The component-based buckling element is illustrated in Figure 6-2. The flange-buckling element is composed of four nonlinear horizontal springs at the flange positions. Two springs, one to act in tension and one to act in compression, are located at each flange, representing its resistance. For the set of springs at either location, only one spring will be activated at any instant, depending on the sense of the spring force. The beam-web shear buckling is represented by the shear-buckling component (the vertical spring of

the buckling element in Figure 6-2). The length of the component-based buckling element is calculated according to Equation (6-1) on the basis of elastic buckling theory (Timoshenko and Gere, 2009), which has been modified to consider the effects of temperature and steel grade. In most fire tests only one shear-buckling wave has been observed, and this is usually aligned at around 45° to the horizontal. Therefore, the shear-buckling panel is not usually longer than the beam depth *d*, and the flange buckling wave lies between the two plastic hinges (Points B and C in Figure 6-1 (b)) on the bottom flange. Hence, it has been assumed that the flange-buckling wavelength L_p, calculated by Equation (6-1), is limited not to be longer than the beam depth *d*. The connection element shown in Figure 6-2 is a typical component-based flush end-plate connection. The compression springs in the connection element represent column flange and end-plate in compression due to bending. The tension springs in the connection element represent bolt rows in tension.

$$L_p = 2\beta c = 2\times 0.713\sqrt{\frac{275}{\sigma_{y,\theta}}}\left(d/b\right)^{1/4}\left(t_f/t_w\right)^{3/4}\left(k_E/(0.7k_y)\right)\times d/2 \qquad (6\text{-}1)$$

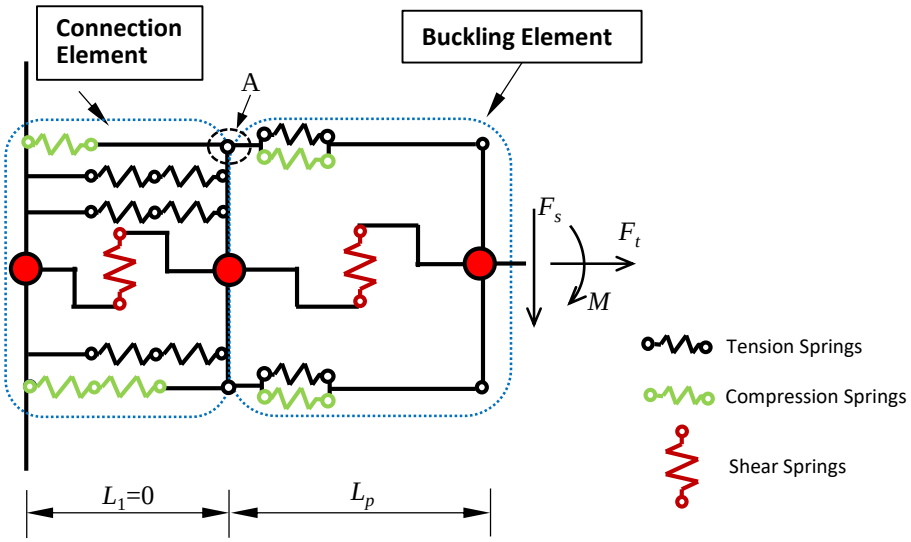

Figure 6-2 Component-based column-face connection and beam-end buckling elements

6.3 LOADING AND UNLOADING PATHS OF THE BUCKLING ELEMENT

During the course of a fire, the beam-end buckling zones can experience complex combinations of internal forces caused by high material nonlinearity and expansions due to temperature variation, interacting with end-restraint conditions. In the model, these forces will be resisted by the horizontal springs at the flanges. These springs can be subject to either compression or tension at different stages of loading/heating. For example, the bottom spring may be in compression during the initial heating phase, and in tension in the high-temperature catenary stage. Therefore, it is essential to establish a robust loading-unloading-reloading approach to deal with deformation reversal at both constant and transient temperatures. The vertical shear spring does not need a reversal path, as reversal of shear does not usually occur.

The Masing Rule (Chiang, 1999) was initially created to model the dynamic force-deflection relationships of structural members under intensive cyclic seismic loading, when the members were loaded into the nonlinear range. It has been widely applied to deal with other engineering problems when the material is highly nonlinear and when residual strains are highly affected by the load-deformation history. Researchers (Block et al., 2007, Gerstle, 1988) have suggested that the Masing Rule could be used to model semi-rigid connections in heating and cooling. In this research, the Masing Rule is incorporated into the characteristic curve of each flange spring of the buckling element, to enable modelling of the buckling panel under any possible loading-unloading-reloading sequence during either constant or transient heating. The Masing Rule has been modified for the post-buckling stage (after bottom-flange buckling

occurs) to ensure that the hysteresis cycles are able to return to their initial points of unloading.

6.3.1 At constant temperature

Based on the Masing Rule, the component characteristics of a spring can be represented by the combination of a "skeleton" curve and a "hysteresis" curve. A schematic illustration of the Masing Rule is shown in Figure 6-3. The hysteresis curve is the skeleton curve scaled by a factor of two and rotated by 180°.

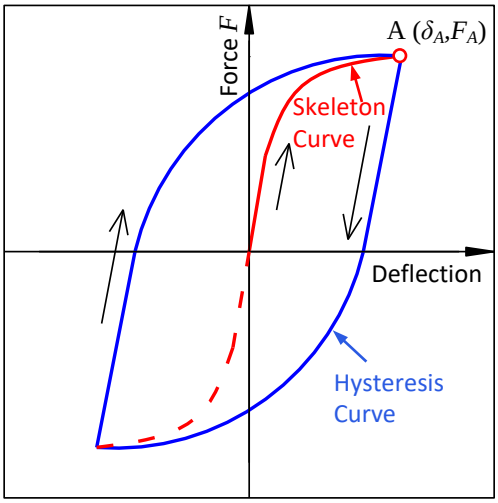

Figure 6-3 A schematic illustration of application of the Masing Rule

If the skeleton curve is described as,

$$\delta = f(F) \tag{6-2}$$

Then the hysteresis curve can be described as,

$$(\delta_A - \delta) = 2f((F_A - F)/2) \tag{6-3}$$

where F_A is the force at which unloading starts and δ_A is the deformation at F_A.

The compression and tension springs at the same location (Figure 6-2) can work in turn, depending on the sense of the spring force, to follow the complete loading-unloading-reloading path.

Compression Spring

In the post-buckling stage, vertical force-deflection relationships for the buckling element, due to the combined effects of bottom flange buckling and shear buckling, has been derived based on the yield-line theory introduced in Chapter 4. Deducting the effect of shear buckling from the total vertical deflection, the moment-rotation relationship of the buckling element due to flange buckling alone is as illustrated in Figure 6-4. This relationship is based on the assumption that the beam is axially unrestrained, and therefore has no net axial force.

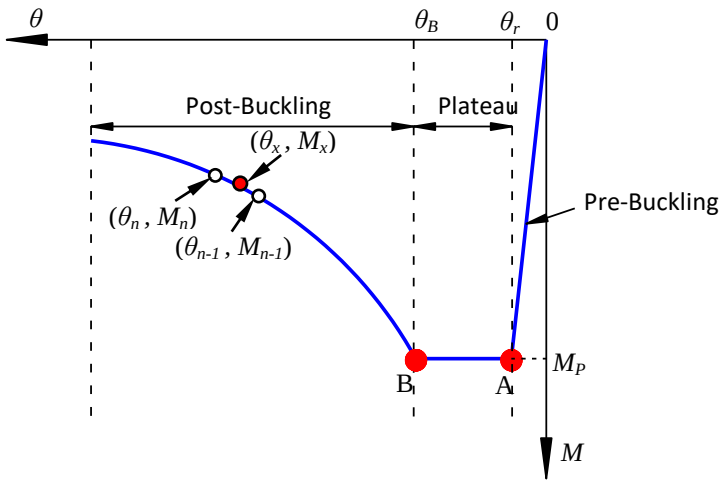

Figure 6-4 Moment-rotation relationship of the buckling element

The force-deformation relationship of the compression spring at the buckling flange, including the three stages (pre-buckling, plateau and post-buckling), is shown in Figure 6-5 (a). The pre-buckling stage ends when the spring force reaches F_R. The stiffness of the compression spring in the pre-buckling stage follows the elastic stiffness. The value of F_R can be calculated using Equation (6-4).

$$F_R = \sigma_{y,\theta} \times (b_f \times t_f + d \times t_f / 2) \quad (6\text{-}4)$$

The axial force remains constant until the initiation of plastic local buckling (Point B). Figure 6-5 (c) shows the yield line pattern in the post-buckling stage.

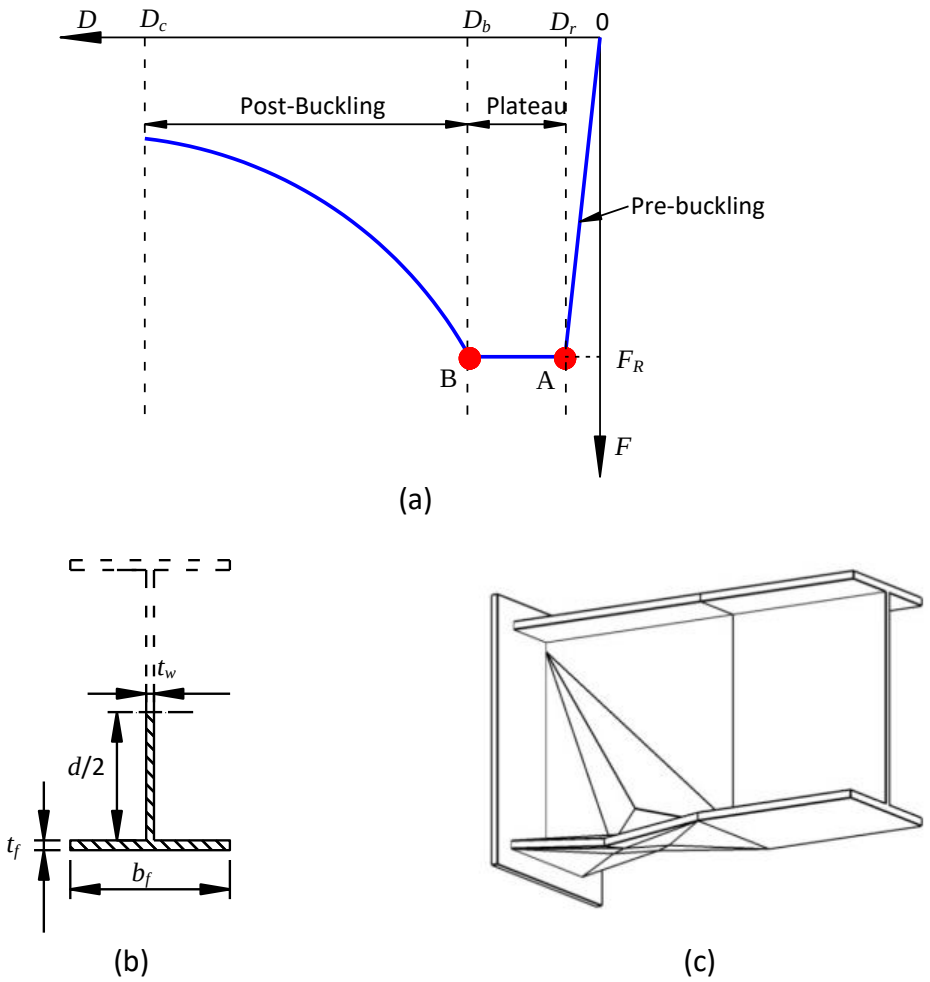

Figure 6-5 Schematic characteristics of the compression spring on the buckling flange

It is assumed that, in the post-buckling stage, the stiffness of the bottom spring is a reduction of that of half the I-section, as shown in Figure 6-5 (b). The stiffness of the bottom spring representing the buckled flange is so low compared to that of the tension spring that the deformation of the non-buckling flange can be neglected. Therefore, the centre of rotation of the buckling element is assumed to be at the top

flange, where the buckling element is connected to the connection element (Point A in Figure 6-2). The compression spring deformation can be represented as:

$$\Delta_B = \theta d \tag{6-5}$$

For this axially unrestrained case, only the shear force and bending moment from the connected beam are transferred to the buckling element. Therefore, the force equilibrium within the buckling element gives:

$$F_{UB} + F_B = 0 \tag{6-6}$$

$$(F_{UB} - F_B) \times 0.5d = M \tag{6-7}$$

where Δ_B is the axial deformation of the buckled flange, M is the moment about the centre-line of the I-section, and F_{UB} and F_B are the forces in the unbuckled (top for this case) and buckled (bottom for this case) springs, respectively.

The analytical model in Chapter 4 can be used to determine the moment-rotation relationship (Equation (6-8)) of the buckling element:

$$M = f(\theta) \tag{6-8}$$

Substituting Eqs. (6-5) - (6-7) into Equation (6-8), the axial force-deformation relationship of the buckled spring is:

$$F_B = f(\Delta_B) / d^2 \tag{6-9}$$

The curved descending part of the moment-rotation relationship of the buckling element has been simplified to a multi-linear relationship. The aim of the iteration procedure is to work out the force-displacement curve for each iteration in the post-buckling stage. The rotation θ at any given bending moment can be found through linear interpolation within each linear increment (Figure 6-4). For any given θ, the corresponding vertical movement D_x can be calculated. The compressive spring force can be derived based on Equation (6-9) as:

$$F_x = F_R + K_1 \times (D_{m\text{-}1} - D_B) + K_2 \times (D_x - D_{m\text{-}1}) \quad (6\text{-}10)$$

where

$$K_1 = (M_P - M_{n\text{-}1}) / (d^2 \times (\theta_B - \theta_{n\text{-}1})) \quad (6\text{-}11)$$

$$K_2 = (M_{n\text{-}1} - M_n) / (d^2 \times (\theta_{n\text{-}1} - \theta_n)) \quad (6\text{-}12)$$

Figure 6-6 (a)-(c) illustrate the various possibilities for re-loading curves, when unloading initiates at the different stages (pre-buckling, plateau and post-buckling) for the compression spring. The initiation point of unloading in a convergent time step is defined as the "Intersection Point" for the following time step. The loading curve prior to the plateau stage (at Point A in Figure 6-6) is composed of an initial linear part followed by a nonlinear part. It is assumed that the heights of the linear and nonlinear parts are identical. When unloading starts from the plateau stage, since the hysteresis curve (the thick line) is the skeleton curve (the thin line) scaled by a factor of two and rotated by 180° following the Masing Rule, the linear part of the unloading curve finishes exactly at the point where it meets the horizontal axis; their intersection is defined as the "Reference Point". The Intersection Point and the Reference Point update at every convergent time step. In order to simplify the calculation, it is assumed that the linear part of the unloading path always stops at the Reference Point; the linear path is followed by a curved part, which is the nonlinear part of the initial loading curve scaled by a factor two and rotated 180°. In other words, the unloading path will stop its linearity when it hits the X axis, and be followed by a nonlinear curve for which the tension spring is activated. The force resistance of the tension spring is F_R. At the end of the unloading curve, the tensile force in this spring is equal to the magnitude of the compressive resistance F_R of the compression spring.

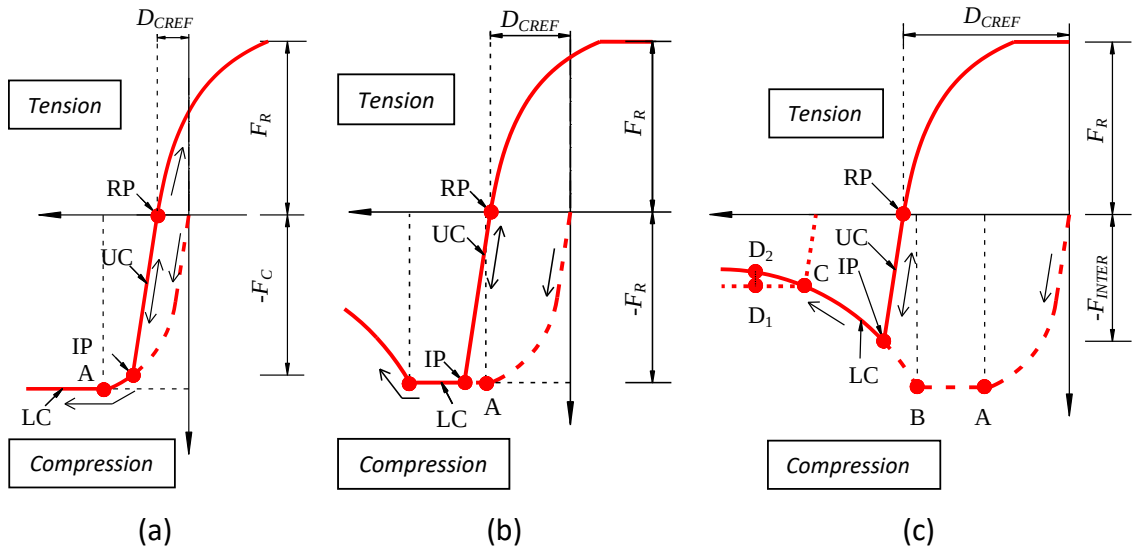

RP = Reference Point; IP = Intersection Point
LC = Loading Curve; UC = Unloading Curve

Figure 6-6 New unloading-loading curves at different stages: (a) pre-buckling stage; (b) plateau; (c) post-buckling stage

Once reloading occurs, if the compressive deformation of the compression spring is larger than the recorded position of the Intersection Point, the load path will follow the initial loading curve.

The coordinate of the Reference Point is determined by Equation (6-13).

$$D_{CREF} = D_C - F_C / K_{IC} \tag{6-13}$$

where D_{CREF} is the coordinate of the Reference Point, K_{IC} is the initial elastic stiffness of the compression spring. The compressive deformation D_C and force F_C are absolute values (always positive).

If the total spring deformation at the end of an arbitrary iteration is smaller than that of the pre-existing Intersection Point, deformation reversal will occur, following the thick line between the Intersection Point and Reference Point (the existing unloading

path). The slope of the unloading path is equal to the initial elastic stiffness K_{IC} at the relevant temperature. The compression force on the unloading curve is:

$$F_C = F_{INTER} + (D_{INTER} - D_C)K_{IC} \quad (6\text{-}14)$$

For an arbitrary iteration, the spring force can be calculated based on the spring deformation of the previous iteration. In the post-buckling stage, the spring stiffness on the loading path is negative. This negative stiffness leads to the situation that one force corresponds to two possible deformations (one on the loading path, one on the unloading path). In order to avoid this numerical singularity, the following approach has been proposed. Point C is assumed to be the start of an arbitrary iteration (Figure 6-6 (c)). For the loading path, a 'zero' stiffness (instead of a negative stiffness) is assumed to define the start of the next iteration. The unloading path remains unchanged. The loading and unloading paths become the dashed lines starting from Point C. When the internal force is larger than the external, the iteration will follow the unloading path. Otherwise, the loading path is adopted, in which case Point D_1 is assumed to be the end of this iteration. The position of D_1 depends on the size of the iteration step. In the next iteration Point D_2, which has the same deformation as that of Point D_1, will be used as the starting point, but the spring force is calculated based on the descending post-buckling curve. At the end of each iteration, the difference between the internal and external forces is checked; this iterative process stops when a balance between the external and internal forces is found.

The deformation of the compression spring D_C can be calculated according to the differential displacement of the two nodes of the buckling element. When the spring deformation is on the unloading path above the Reference Point (Point RP in Figure

6-6 (a, b, c)), the spring will be under tension. The compression spring is deactivated; the tension spring at the same location will be activated instead.

The model has been developed on the basis of the assumption that there is no restraint to thermal expansion. The model is also valid for restrained cases, since the buckling criterion (the bottom spring experiences a certain amount of compressive squash) is calculated from a yield line mechanism, which is not affected by the restraint conditions. The only difference between the restrained and unrestrained cases is that the bottom spring force is larger in the former case than in the latter, and the model is capable of adjusting the spring force level to achieve equilibrium.

Tension Spring

The characteristics of the tension spring for the initial loading stage are similar to those of the compression spring, but lack the post-buckling phase (Figure 6-7). The unloading procedure follows rules similar to those for the compression spring described above.

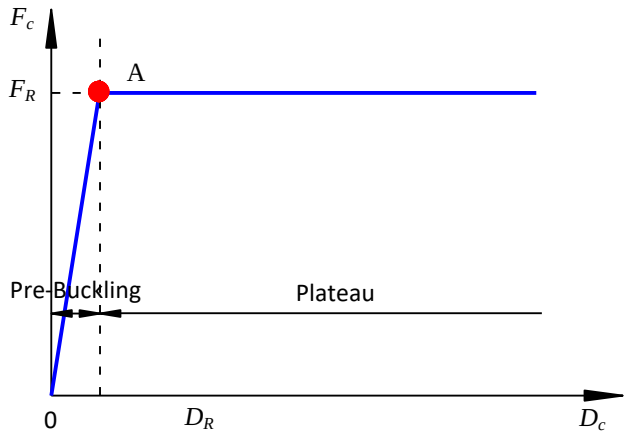

Figure 6-7 Schematic characteristics of the tension spring

Shear Spring

It has been shown in Chapter 4 that the beam-web shear buckling and flange buckling modes can be separated in the post-buckling stage of the combined buckling mode.

Their angles of rotation ϑ_1 and ϑ_2 can be calculated using displacement compatibility. Therefore, the behaviour of the individual springs (the shear spring and the top and bottom flange springs) can be determined. In the pre-buckling and plateau stages, the shear buckling spring is assumed to be rigid. In the post-buckling stage the behaviour of the shear spring is proportional to the overall behaviour of the flange springs, as shown in Figure 6-4. The moment-vertical displacement relationship caused by shear buckling can be calculated according to the shear panel's moment-rotation relationship. The loading-unloading-reloading path has not been applied to the shear spring, as displacement reversal never occurs to this spring. The effect of the beam-web shear buckling on deflection in the combined buckling mode is actually an increase of the transverse drift of the buckling panel due to bending.

6.3.2 During transient heating

At elevated temperatures, the material stress-strain characteristic is temperature-dependent. The essential assumption for deformation reversal at increasing temperatures is that the permanent deformation of a spring is unaffected by change of temperature, and so the Reference Point of the unloading curve does not change between two adjacent temperature steps. The new unloading path will still be linear, following the initial slope of the force-deformation relationship at the new temperature, and so the Intersection Point (at which unloading initiates) relocates. Taking the compression spring at plateau stage as an example, Figure 6-8 shows the loading and unloading procedure when the spring's temperature increases.

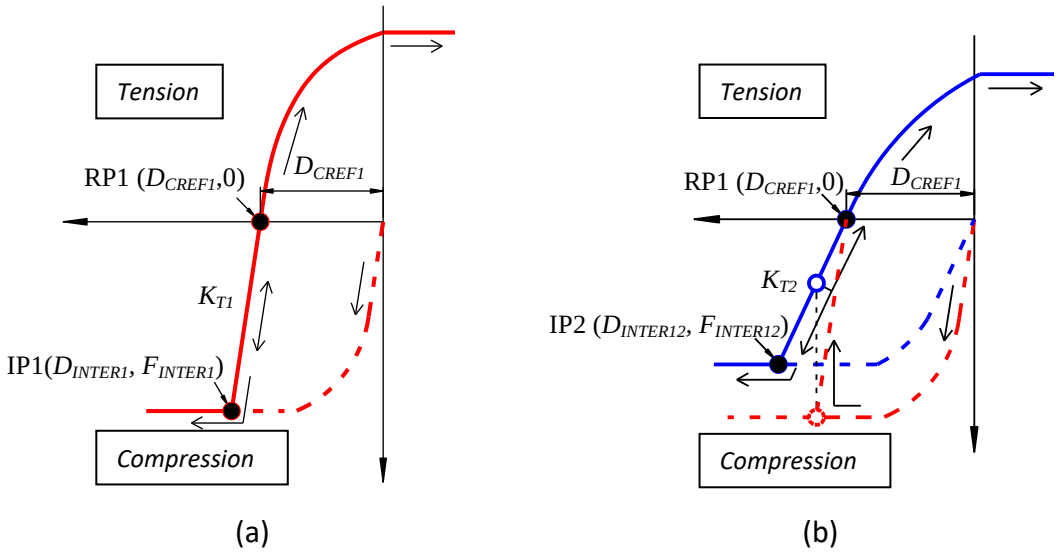

Figure 6-8 Loading and unloading procedure when temperature increases: (a) at temperature T_1; (b) at temperature T_2 ($T_2 > T_1$)

The loading and uploading paths at the initial temperature T_1 are shown in Figure 6-8 (a). The deformation at the Reference Point can be calculated using,

$$D_{CREF1} = D_C - F_C / K_{T1} \tag{6-15}$$

When the temperature increases to T_2 the Reference Point remains identical, while a new Intersection Point can be found using the new initial elastic stiffness K_{T2}. The spring deformation of the new Intersection Point is,

$$D_{INTER2} = D_{CREF1} + F_{R2} / K_{T2} \tag{6-16}$$

The deformation of the compression spring remains identical between adjacent iterations within the same temperature step. Therefore, when the temperature increases to T_2, the Intersection Point falls onto the unloading path of the new force-deformation relationship where K_{T2} is greater than K_{T1}, as shown in Figure 6-8 (b). This sudden jump disturbs the force equilibrium, and so in the following iterations the spring deformation is adjusted until a balance between the internal and external forces is found. The spring will follow the loading path if its deformation is larger than

that of the Intersection Point ($D_C > D_{INTER2}$), where D_C and D_{INTER2} are absolute values (always positive) of the spring deformation. Otherwise, the spring follows the unloading path. The spring force is calculated using Equation (6-17):

$$F_C = F_{INTER2} + (D_C - D_{INTER2})K_{T2} \quad (6\text{-}17)$$

When the spring follows the unloading path above the Reference Point, it will be subject to tension. The characteristics of the tension spring follow the same rules described in Section 6.3.1. A flowchart of the procedure for modelling the compression spring is shown in Figure 6-9.

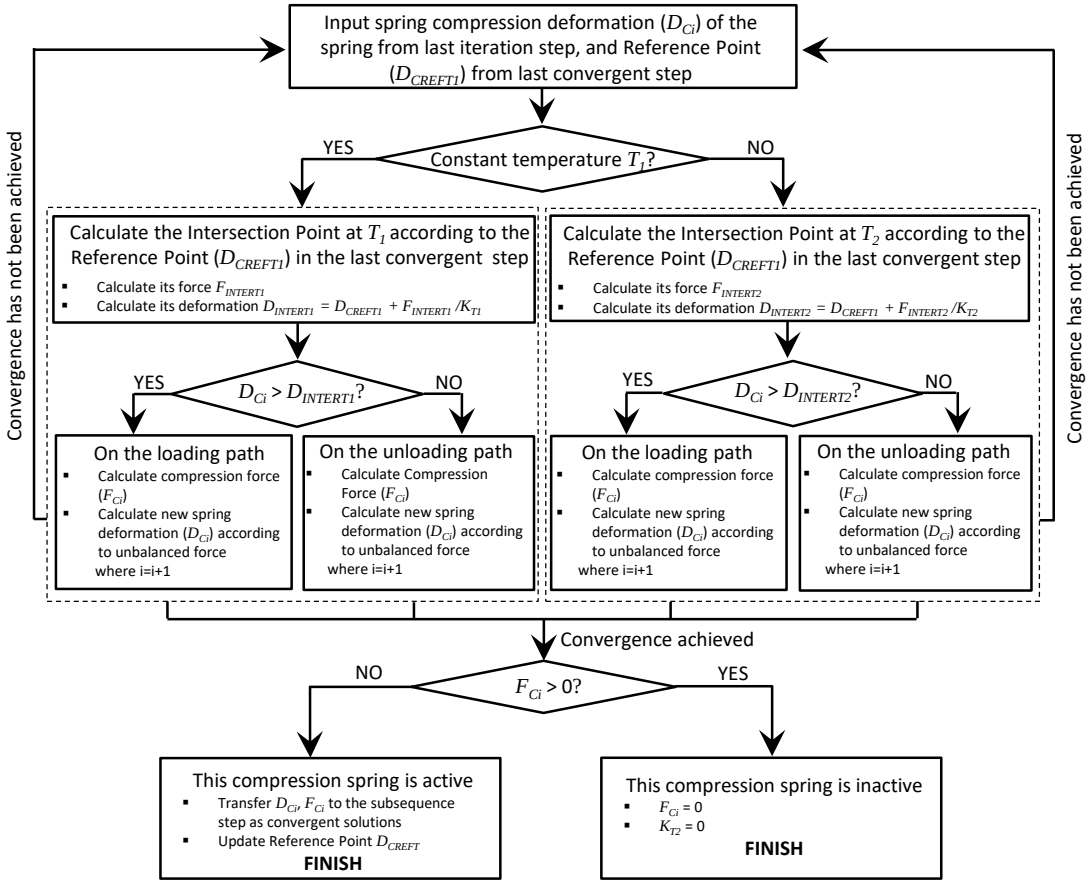

Figure 6-9 Flowchart of the developed procedure for modelling the compression spring

6.3.3 An example of implementing the analytical model into Vulcan

In this section, a step-by-step calculation example of implementing the analytical model demonstrated in Chapter 4 will be presented. The example is an isolated beam, 6m fixed-ended beam with one buckling element on each side. The beam section is UB356x171x51. The beam was firstly uniformly loaded at ambient temperature up to the load ratio reaches 0.4 (26.8kN/m), and was subsequently be heated to 750°C following standard fire curve.

Step 1:

At ambient temperature, the stiffness of both the top and bottom springs is

$$\begin{aligned} KINI &= E_{\alpha,\theta} \times (b \times t_f + 0.5 \times d \times t_w) \\ &= 210000 \times (171.5 \times 11.5 + 0.5 \times 343.5 \times 7.4) = 681072000 N / mm \end{aligned} \quad (6\text{-}18)$$

The shear spring is assumed to be rigid. The stiffness of the shear spring is defined to be 1.0×10^{20}.

An iteration procedure is applied to the program to calculate the force-deflection curve of the buckling element of each step, given that the stiffness of each flange spring is given in Equation (6-18). The ambient-temperature calculation is always within the pre-buckling stage.

Step 2:

At elevated temperatures, both the material Young's Modulus and the Yield Stress have been reduced. Axial force is created due to the restraint of thermal expansion. The axial force, as well as the bending moment at the end of the buckling element, creates large compression force on the bottom compressive spring. When the compression force reaches the value shown in Equation (6-19), the compression spring enters the plateau stage.

$$F_R = M / d = \sigma_{y,\theta} \times (0.25 \times t_w \times d^2 + b \times t_f \times (t_f + d)) / d$$
$$= k_{y,\theta} \times 246.51 \times (0.25 \times 7.4 \times 343.5^2 + 171.5 \times 11.5 \times (11.5 + 343.5)) / 343.5 \quad (6\text{-}19)$$
$$= k_{y,\theta} \times 659107N$$

where $k_{y,\theta}$ is the reduction factor of the yield stress due to temperature at the corresponding iteration step. In this example, the initial temperature of the plateau stage of the compressive spring is 90°C. The reduction factor $k_{y,\theta}$ equals to 1.

In the plateau stage, F_R is always calculated following Equation (6-19) except that $k_{y,\theta}$ keeps decreasing with the increase of temperature. The stiffness of the compressive spring is zero. The end of the plateau stage is the point of intersection between the plateau and the post-buckling descending curve described in Chapter 4. For this example, the plateau stage ends at 261°C.

In the post-buckling stage, when the compression spring is on the loading curve, its stiffness is 0; its compression force at each iteration step can be calculated following Equation (6-10). When the compression spring is on the unloading curve, its stiffness can be calculated according to Equation (6-18), and its compression at each iteration step can be calculated according to Equation (6-17). The detailed outputs of this example are shown in the Appendix.

6.4 RESULTS

6.4.1 Verification of the Vulcan models

In order to verify the newly created component-based element in Vulcan, example beams were modelled using both Vulcan and ABAQUS. A sketch of the Vulcan model using buckling elements is shown in Figure 6-10 (a). The beam element in Vulcan is actually a line element, and the end zones of the beam are simulated by the new component-based buckling elements.

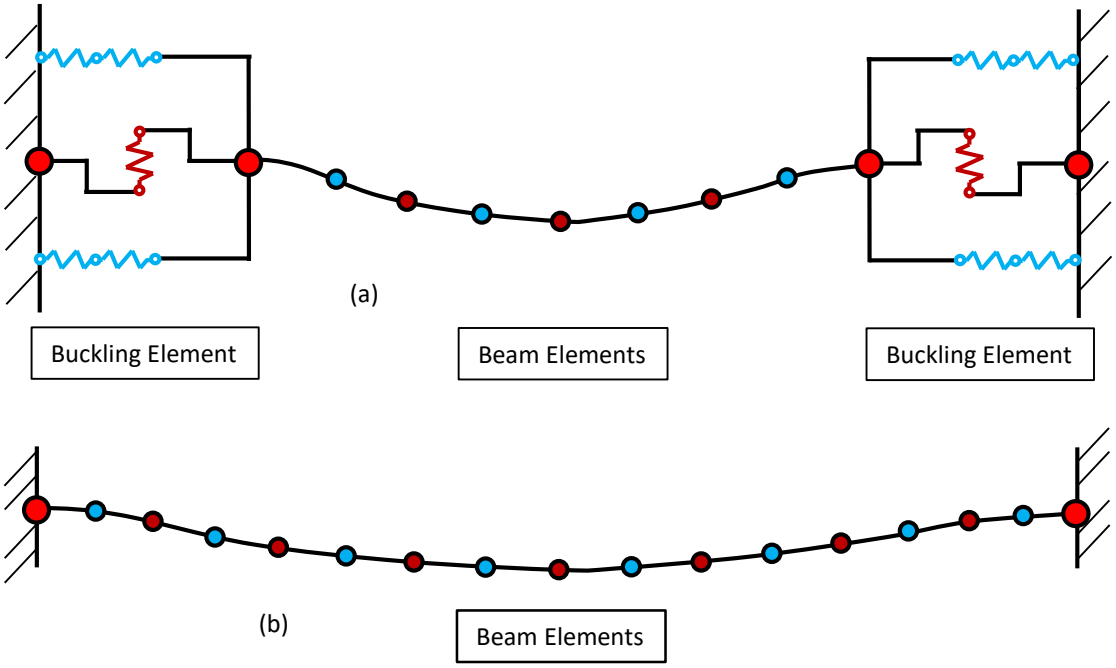

Figure 6-10 Comparison of Vulcan models: (a) beam with buckling elements; (b) beam with beam elements only

In order to allow reasonable comparison, the ABAQUS models also consist of three parts: two beam ends modelled by shell elements and the rest of the beam simulated using wire elements. The images of ABAQUS models are shown in Figure 6-11 (a). Example beams without the buckling elements at the beam ends were also built up in Vulcan (Figure 6-10 (b)) and in ABAQUS (Figure 6-11 (b)) to investigate the effects of the buckling elements by comparing results from the models with and without the buckling elements.

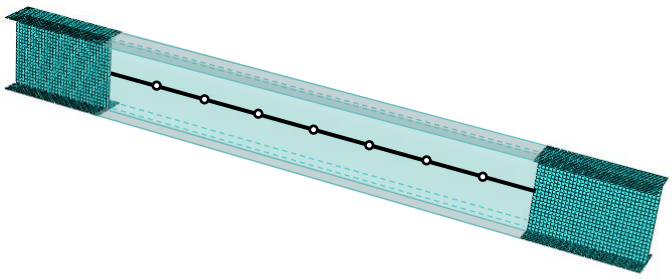

(a)

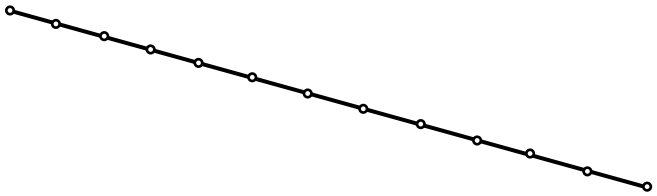

(b)

Figure 6-11 Comparison of ABAQUS models: (a) beam with shell elements; (b) beam with line elements only

For the shell elements in the ABAQUS models, the four-noded shell element (S4R), which is capable of simulating buckling behaviour with reasonable accuracy, was adopted. A mesh sensitivity analysis was conducted, which indicated that elements of size 15mm x 15mm provided an optimum between accuracy and computing efficiency. For the wire element a mesh size of 250mm was adopted after a mesh sensitivity analysis. Material properties, including the thermal expansion coefficient of steel given by EC3, were used. The models were subject to full axial restraint at both ends, and were restrained from out-of-plane deflection so that no overall buckling across the weak axis could occur. Two beams, spanning 6m and 9m, were modelled. The beam section was UB356x171x51 for the 6m beams, and UB457x191x98 for the 9m beams. In order to achieve different combinations of axial force and bending moment the 6m beams were loaded with uniformly distributed load of intensity 26.8N/mm (load ratio = 0.4), 33.5N/mm (load ratio = 0.5) and 40.2N/mm (load ratio = 0.6). The 9m beams were loaded with uniformly distributed load of intensity 29.6N/mm (load ratio = 0.4), 37.0N/mm (load ratio = 0.5) and 44.4N/mm (load ratio = 0.6). The beams were uniformly heated beyond 700°C.

The force-deformation relationships of the springs in the buckling element are shown in Figure 6-12. In Figure 6-12 (a) the dashed curve represents the deformation-

temperature relationship of the bottom spring. The thin solid curve shows the force-deformation response of this compression spring. It has been shown that, after the bottom flange buckles (when the deformation is around 6mm), the compressive force decreases with increase of compressive deformation. The thick solid curve is the fully-yielded force-deformation relationship of this spring, for which the decrease in the axial force would only be due to the degradation of the material as temperature rises (according to EC3). The difference between these curves illustrates the reduction in strength due to buckling. Deformation reversal occurs when the spring deformation is around 34mm. During this reversal, the spring force and its compressive deformation reduce together. After the spring force has changed to tension the compression spring is disabled and the tension spring becomes active. The response of this spring is represented by the dotted curve. The deformation (34mm) of the compression spring before it enters tension, representing the permanent deformation of the bottom flange, will be taken forward by the tension spring.

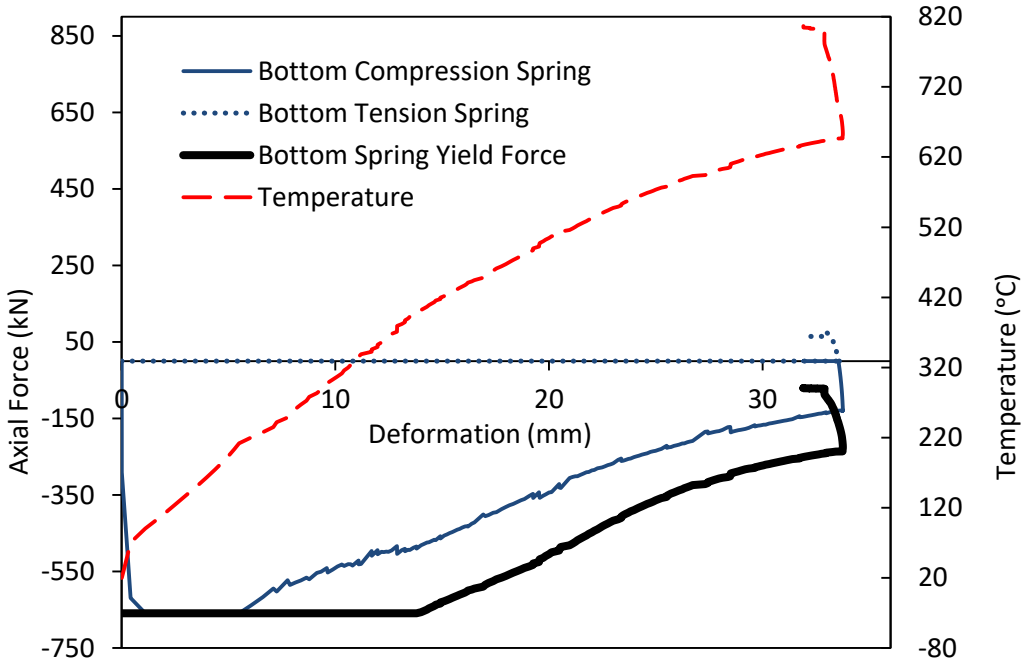

(a)

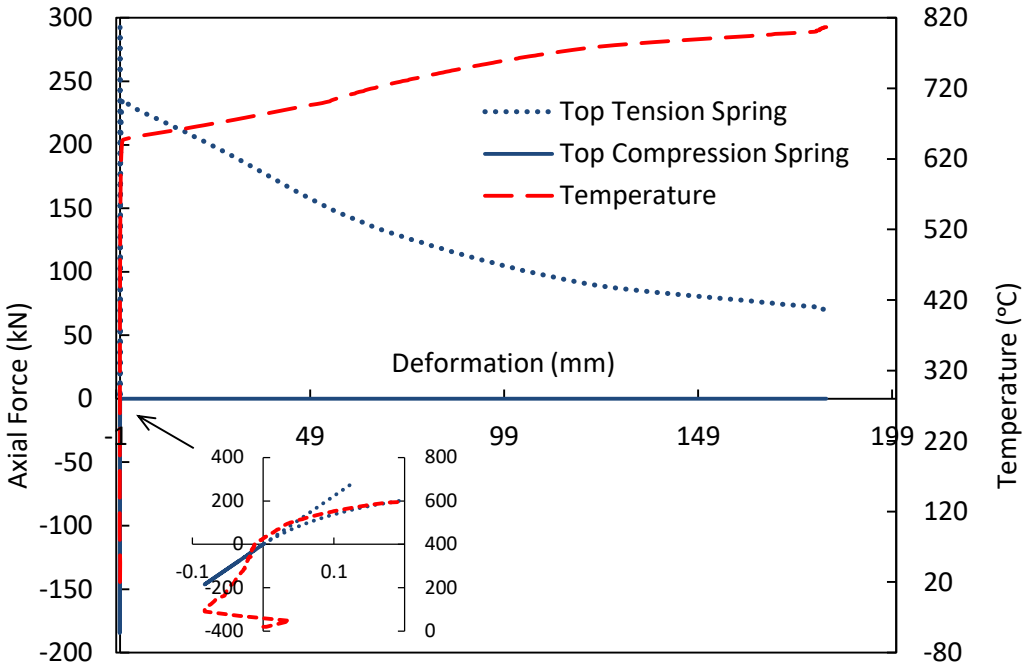

(b)

Figure 6-12 Force-deformation relationship of the springs in the buckling element: (a) bottom spring; (b) top spring

Comparisons of the results from the ABAQUS and Vulcan models, in terms of beam mid-span deflection, axial net force and beam-end moment, against temperature, are shown in Figure 6-13 - Figure 6-18. Figure 6-13 and Figure 6-14 show the temperature-deflection relationships for two beams (those modelled in ABAQUS, as described in Section 6.4.1) under the same load ratios (0.4, 0.5 and 0.6). Figure 6-15 - Figure 6-16 show the temperature-axial force relationships. Figure 6-17 and Figure 6-18 show the temperature-moment relationships. The thick solid lines represent the results from the Vulcan models with buckling elements, whilst the thick dotted lines are for the equivalent ABAQUS models (with shell elements at the beam ends). The thin lines show results from the Vulcan and ABAQUS models without buckling/shell elements.

It can be seen from Figure 6-13 - Figure 6-18 that the results from Vulcan and ABAQUS compare well for beams with and without the buckling elements, for all load ratios.

Figure 6-13 and Figure 6-14 show that the use of the buckling element in Vulcan can improve the accuracy of prediction of mid-span deflection. Models with the buckling elements show the greater deflections, due to the additional beam-end rotations caused by bottom-flange buckling.

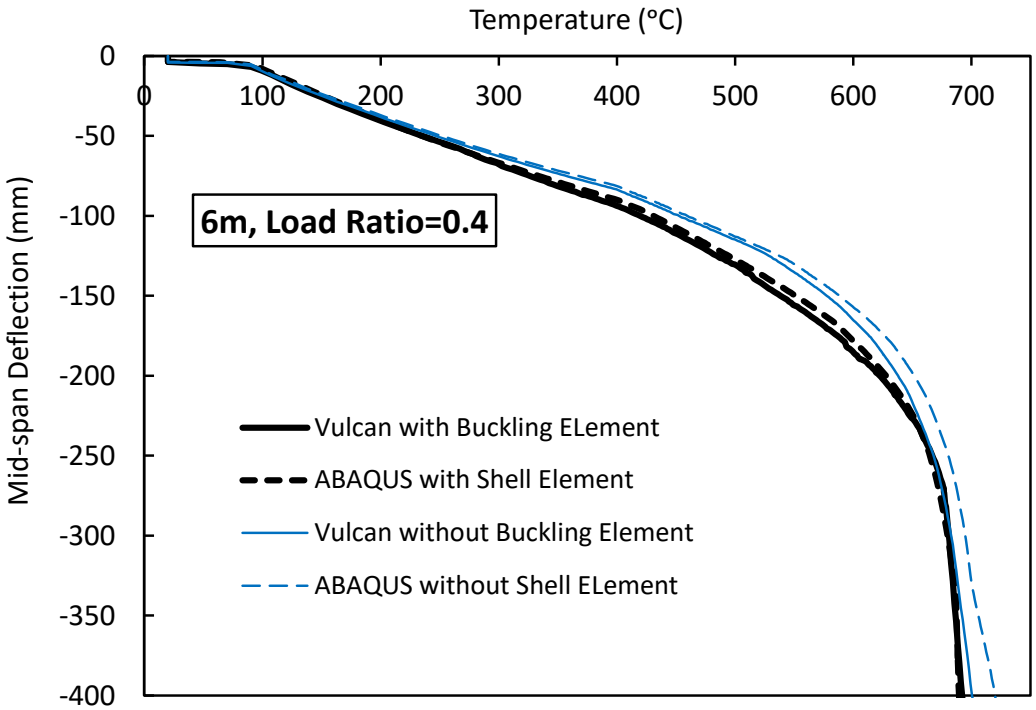

(a)

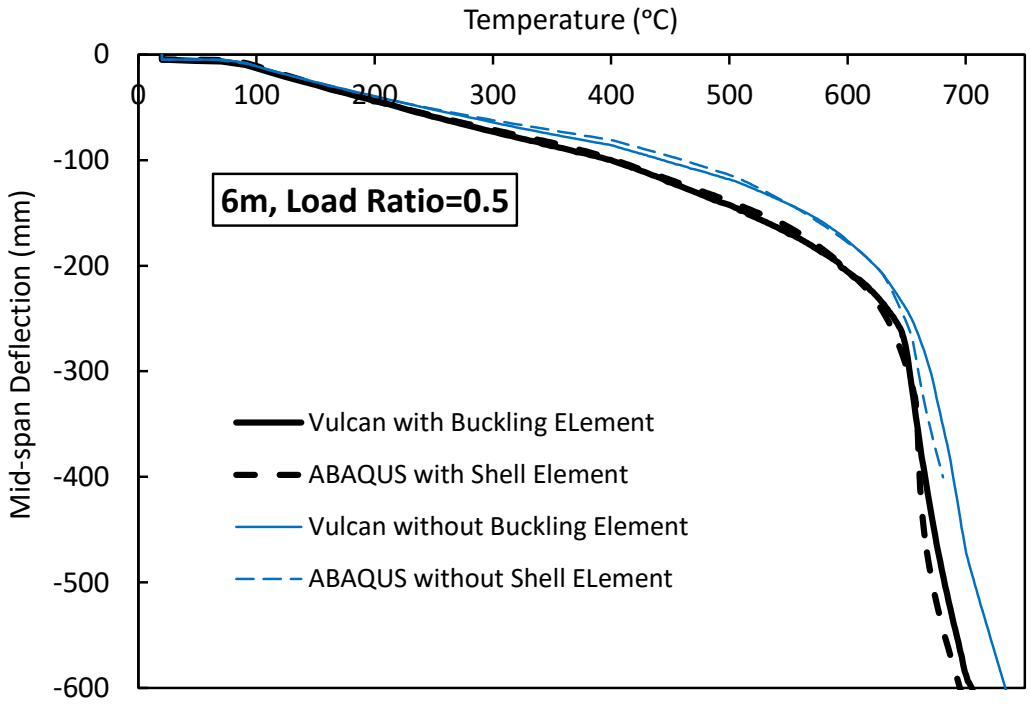

(b)

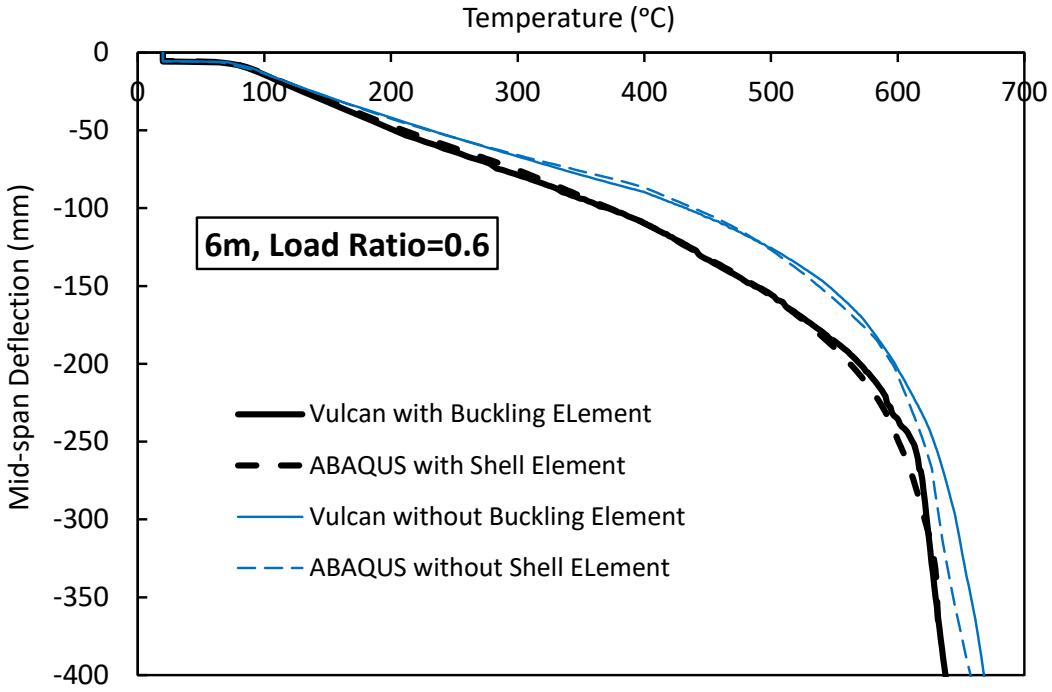

(c)

Figure 6-13 The development of mid-span deflection as temperature rises for 6m beams: (a) for load ratio = 0.4; (b) for load ratio = 0.5; (c) for load ratio = 0.6

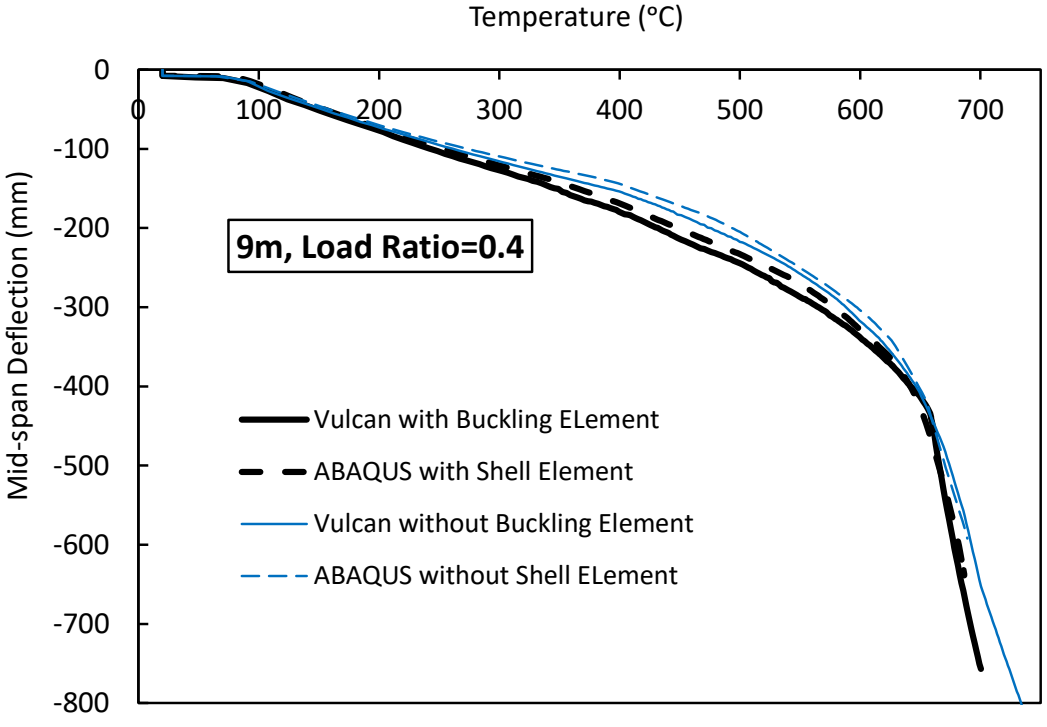

(a)

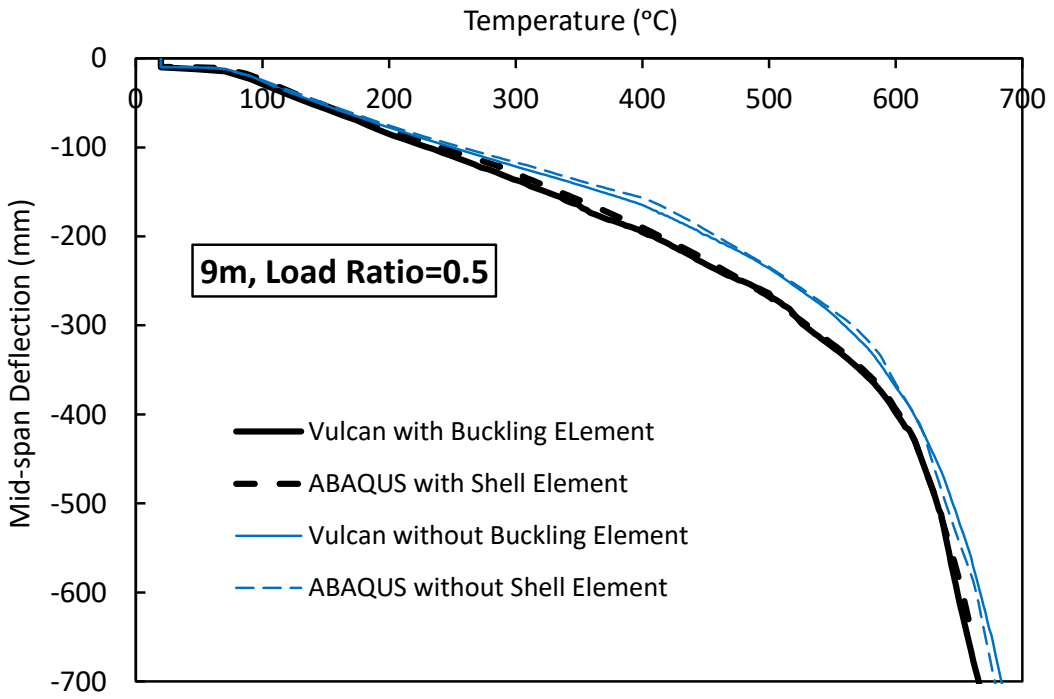

(b)

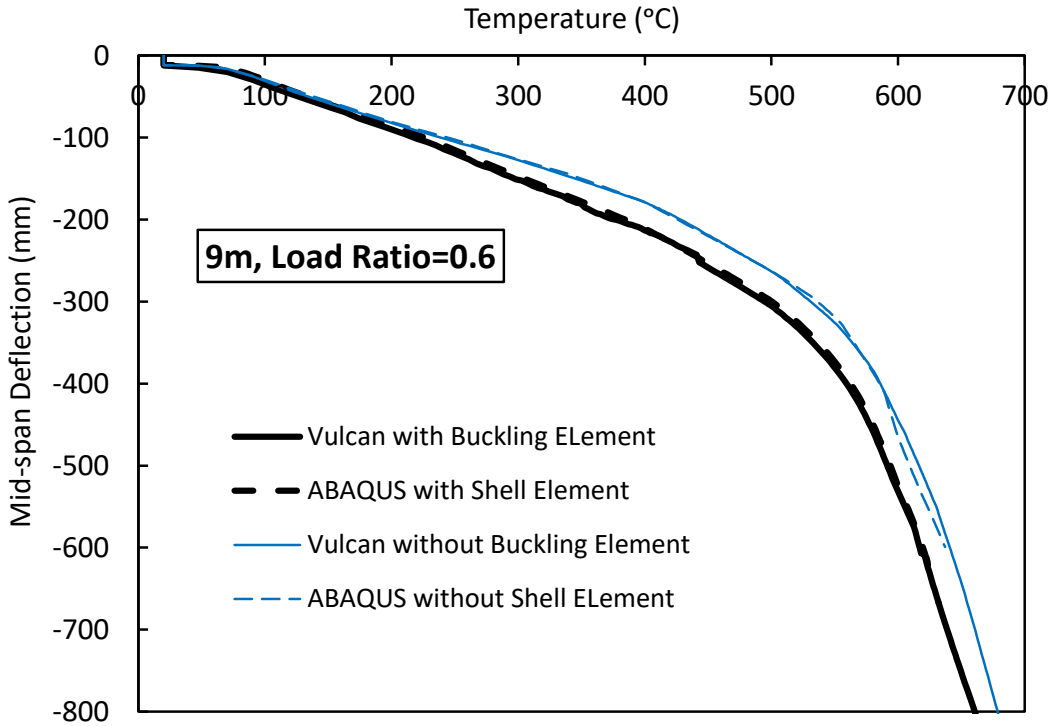

(c)

Figure 6-14 The development of mid-span deflection as temperature rises for 9m beams: (a) for load ratio = 0.4; (b) for load ratio = 0.5; (c) for load ratio = 0.6

Figure 6-15 and Figure 6-16 show that the net compression force at the beam-end decreases when the bottom flange buckles. The beam-end bottom-flange buckling can relieve the axial compression force caused by restraint to thermal expansion, and therefore transfers less compression force onto the adjacent connection element. Beams with the buckling elements initiate their catenary tension phase sooner than those without buckling elements.

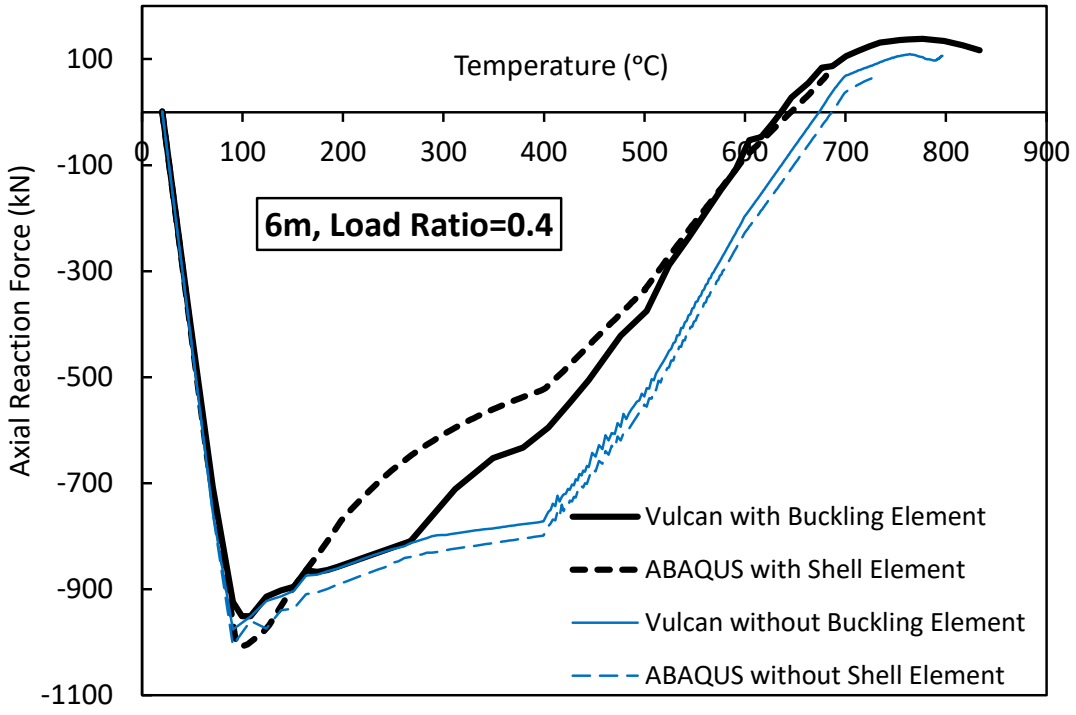

(a)

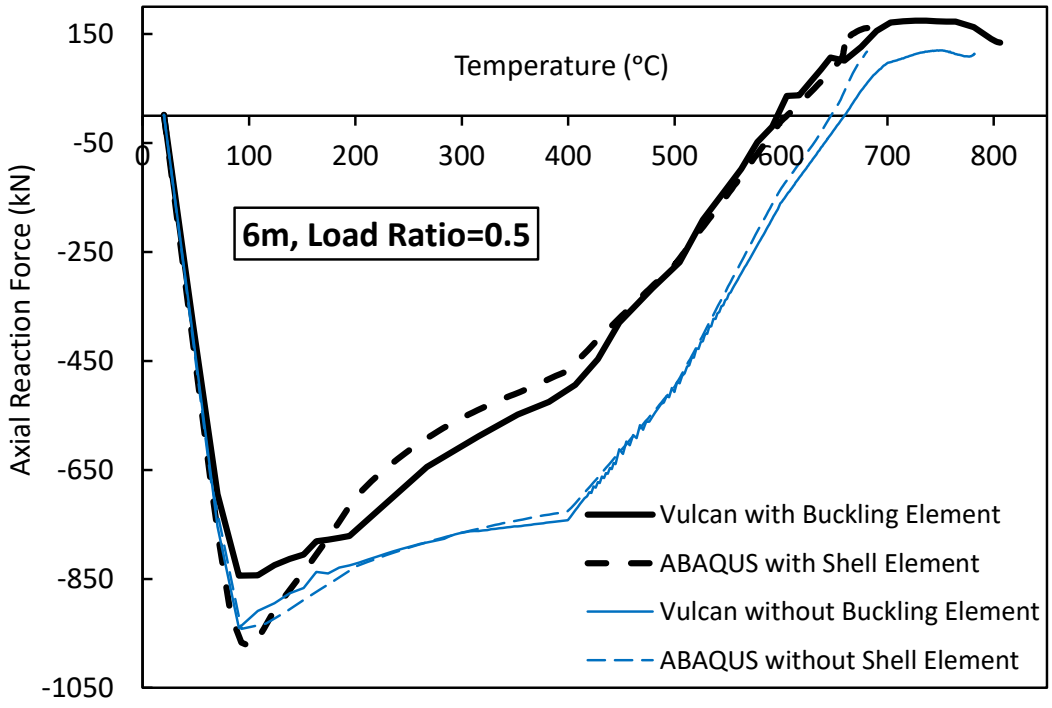

(b)

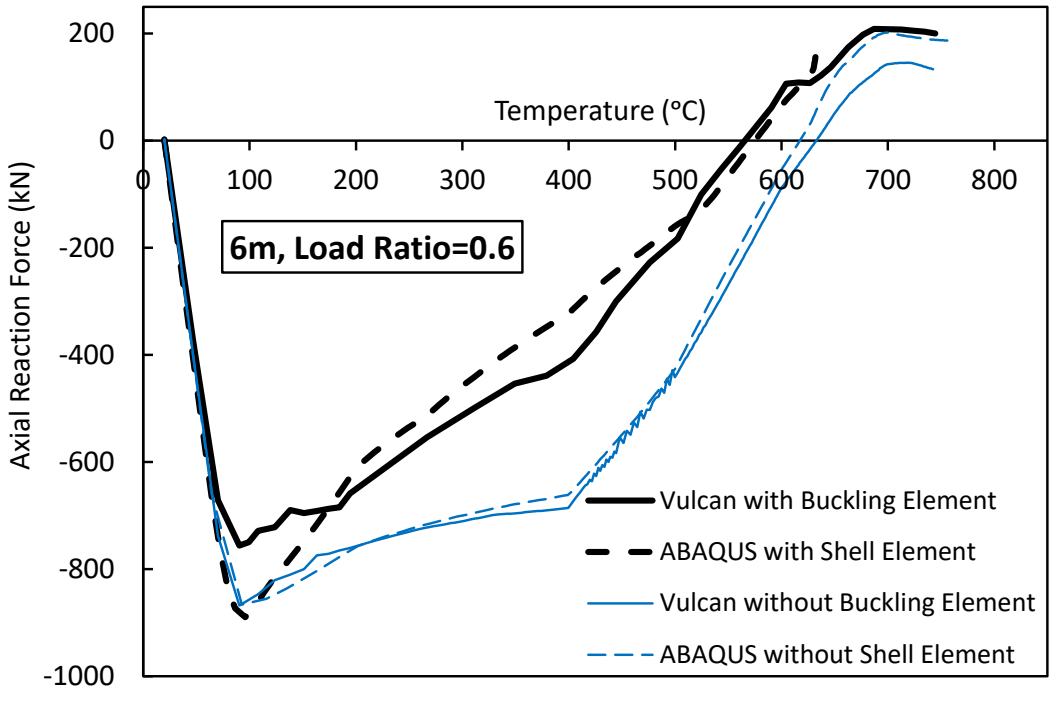

(c)

Figure 6-15 Comparisons of axial net force against temperature for 6m beams: (a) for load ratio = 0.4; (b) for load ratio = 0.5; (c) for load ratio = 0.6

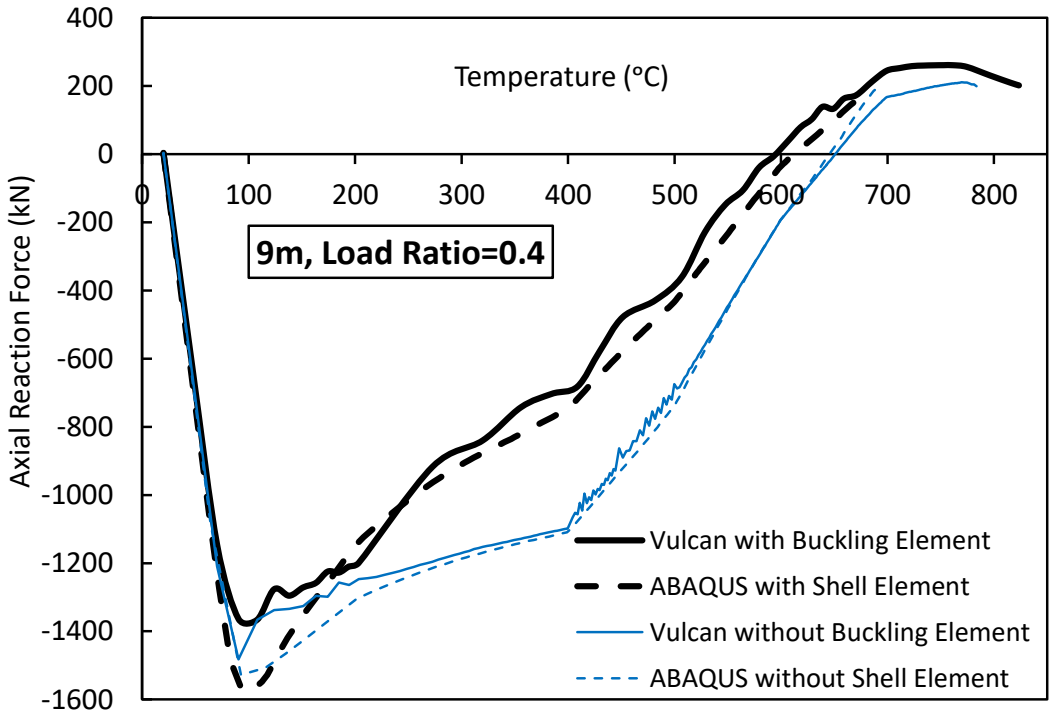
Temperature (°C)
Axial Reaction Force (kN)
9m, Load Ratio=0.4
Vulcan with Buckling Element
ABAQUS with Shell Element
Vulcan without Buckling Element
ABAQUS without Shell Element

(a)

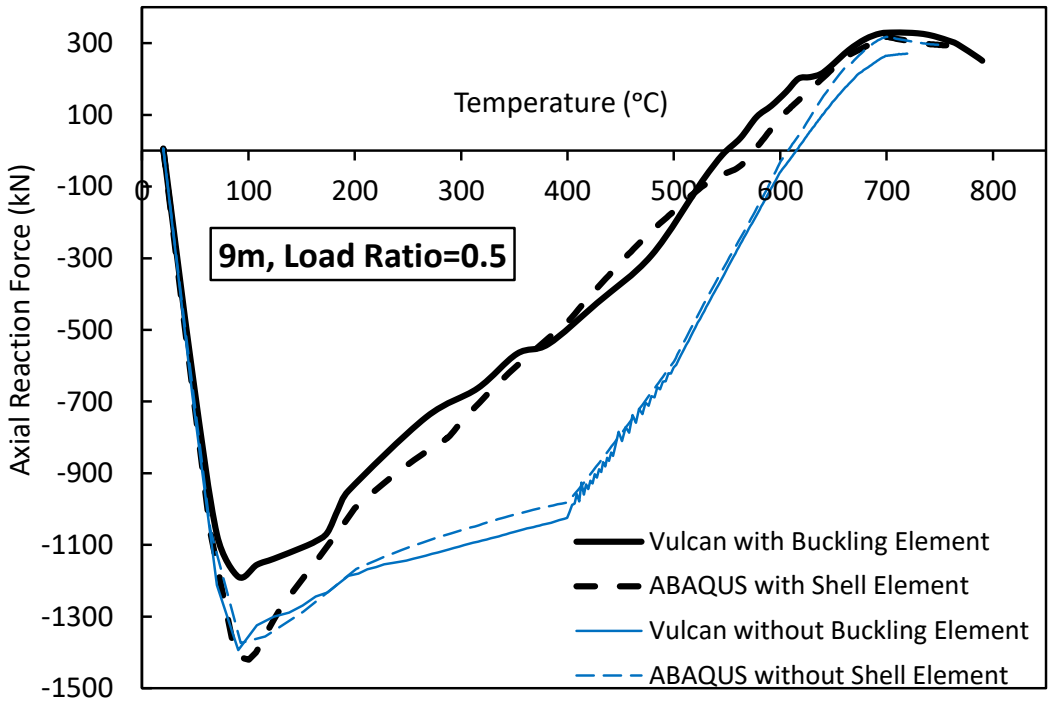
Temperature (°C)
Axial Reaction Force (kN)
9m, Load Ratio=0.5
Vulcan with Buckling Element
ABAQUS with Shell Element
Vulcan without Buckling Element
ABAQUS without Shell Element

(b)

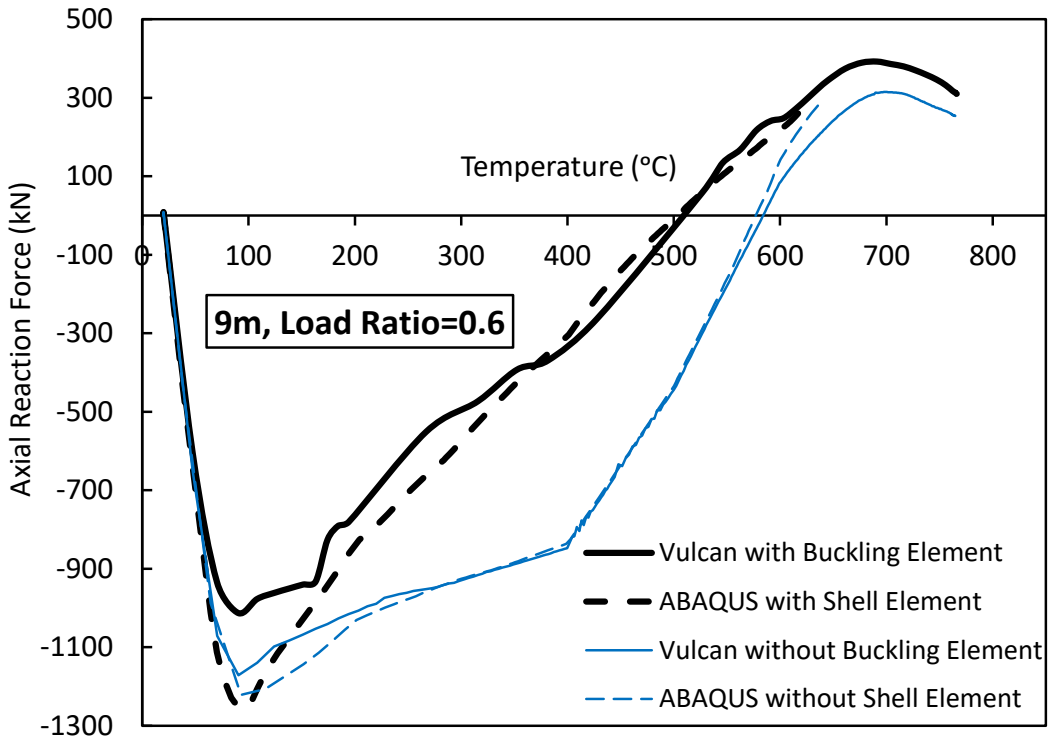

(c)

Figure 6-16 Comparisons of axial net force against temperature for 9m beams

Figure 6-17 and Figure 6-18 show the development of the beam-end major-axis moment as temperature increases. It can be seen that, for beams without the buckling element, the beam-end moment increases from 100°C to 400°C. This is because both the restraint to thermal expansion and the stiffness reduction of the beam induce an increase in the curvature at its ends, while the steel strength remains unchanged up to 400°C. The end-moment starts to decrease when the temperature reaches 400°C, due to the progressive reduction of steel strength above that temperature. For beams with the buckling elements the rotational stiffness of the steel beam-ends is reduced due to the occurrence of bottom flange buckling, resulting in less moment being transferred to the adjacent connections. On the other hand, as the applied load increases the beam-end curvatures increase, causing an increase in the beam-end moment. Therefore, the variation of beam-end moment depends on which of these two is more

dominant. It can be observed from Figure 6-17 and Figure 6-18 that in most cases the beam-end moment decreases between 100°C and 400°C after bottom-flange buckling has occurred at around 100°C. However, for the 6m beam subject to a high load ratio of 0.6, and the 9m beams under load ratios of 0.5 and 0.6, the beam-end moment tends to increase slightly between 300°C and 400°C.

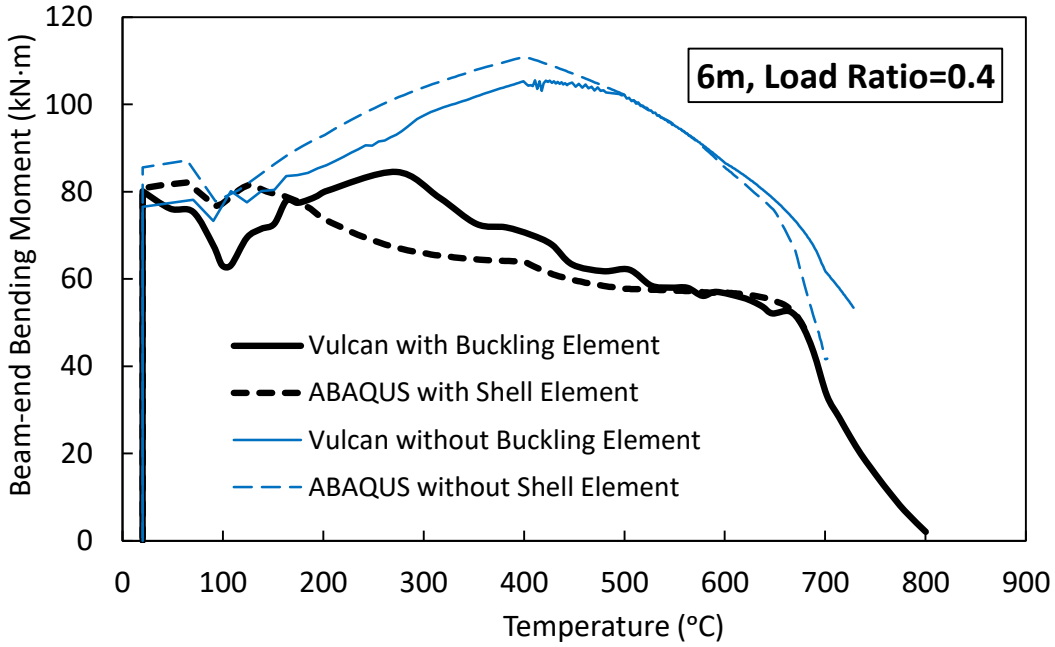

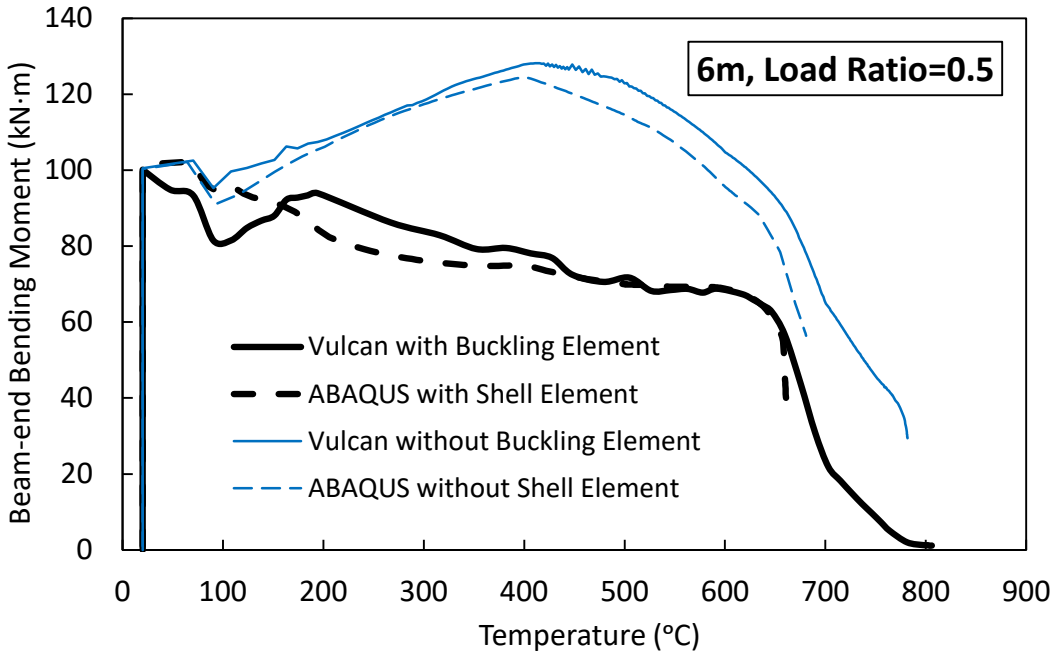

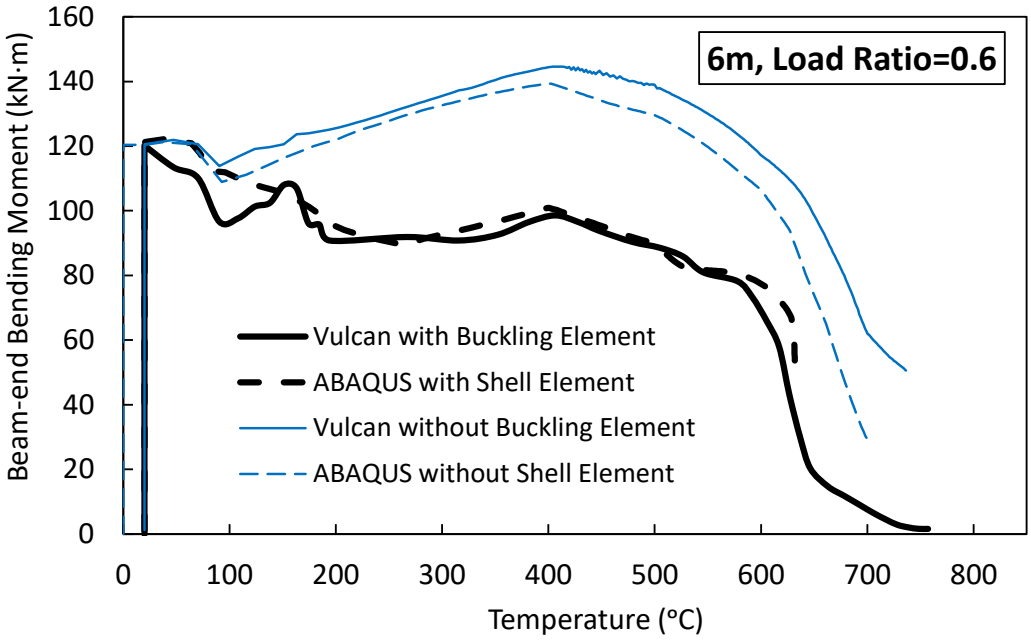

Figure 6-17 Comparisons of beam-end bending moment against temperature for 6m beams

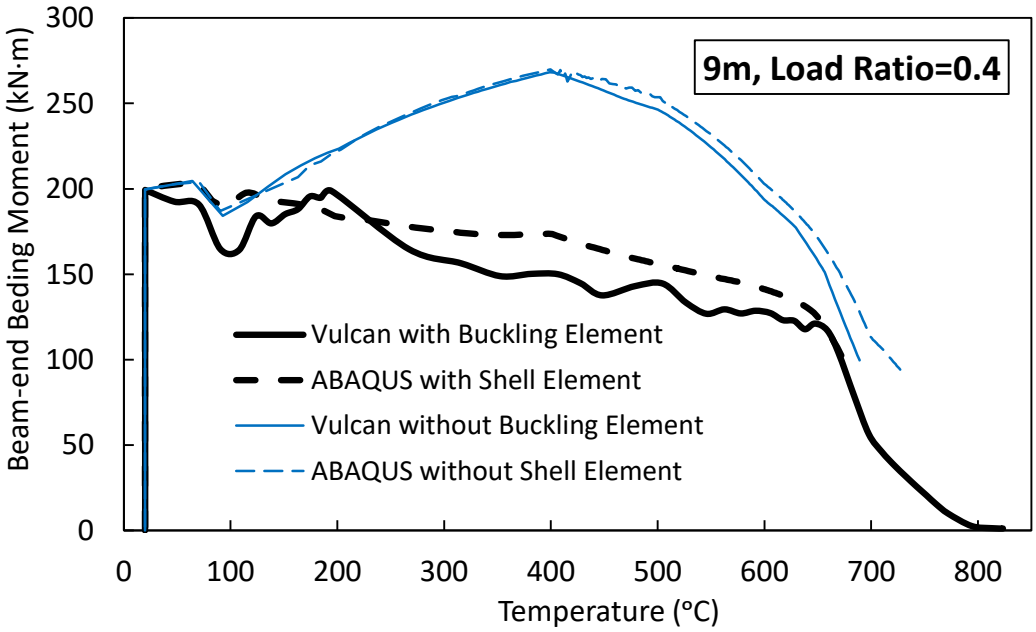

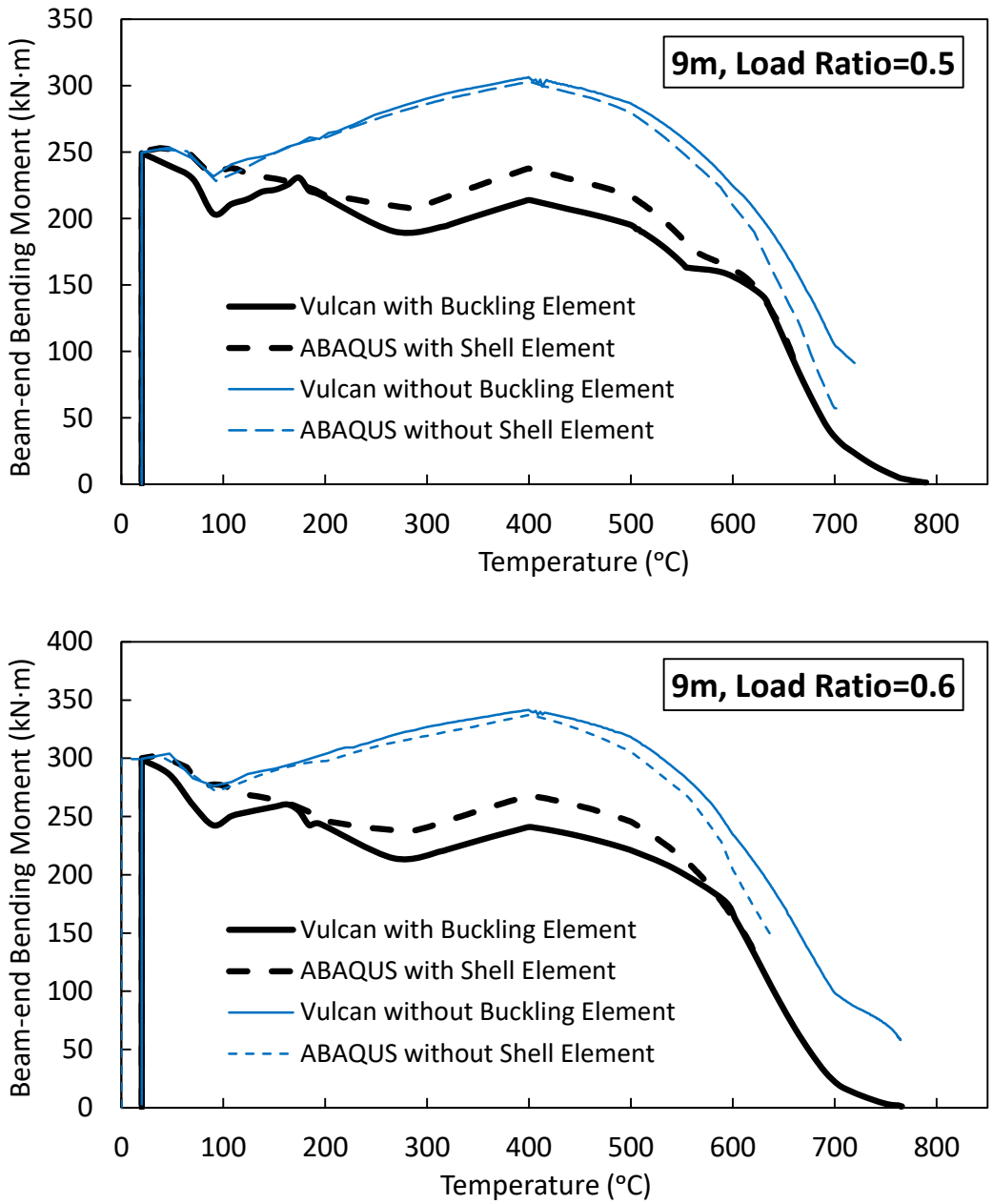

Figure 6-18 Comparisons of beam-end bending moment against temperature for 9m beams

It has been indicated in the Figure 6-12 - Figure 6-17 that the newly created buckling element is capable of accurately modelling the combined effects of beam-end shear buckling and bottom-flange buckling of steel beams at elevated temperatures. The good match between the Vulcan and ABAQUS modeling results confirms that the

buckling element is able to account for the major structural effects of the net axial compression due to restraint to thermal expansion.

The differences between the Vulcan models with and without the buckling elements and between the ABAQUS models with and without shell elements, as shown in Section 6.4.1, have indicated the importance of considering the beam-end buckling phenomena. This is true only if such differences are not caused by the adoption of different element types, especially for the ABAQUS models. This section examines the sensitivity of the ABAQUS modelling results to the element types adopted. Two ABAQUS models, one using wire elements to model the entire beam and one using shell elements which are restrained against buckling, were used to model the beam ends, retaining the wire elements for the rest of the beam, and results were compared as shown in Figure 6-11.

The same mesh size, element type and temperature curve used for the ABAQUS models described in Section 6.4.1 were used. The beam was of section UB356x171x51 and 3m length; this is short enough to avoid bottom-flange buckling. The beam web was fully restrained against out-of-plane deformation, and therefore no beam-web shear buckling was allowed. The two ABAQUS models resulted in indistinguishable deflection and axial force, as shown in Figure 6-19. This confirms that the differences in behaviour between models with and without shell elements at beam-ends are entirely due to beam-end buckling, and are not caused by the use of different element types.

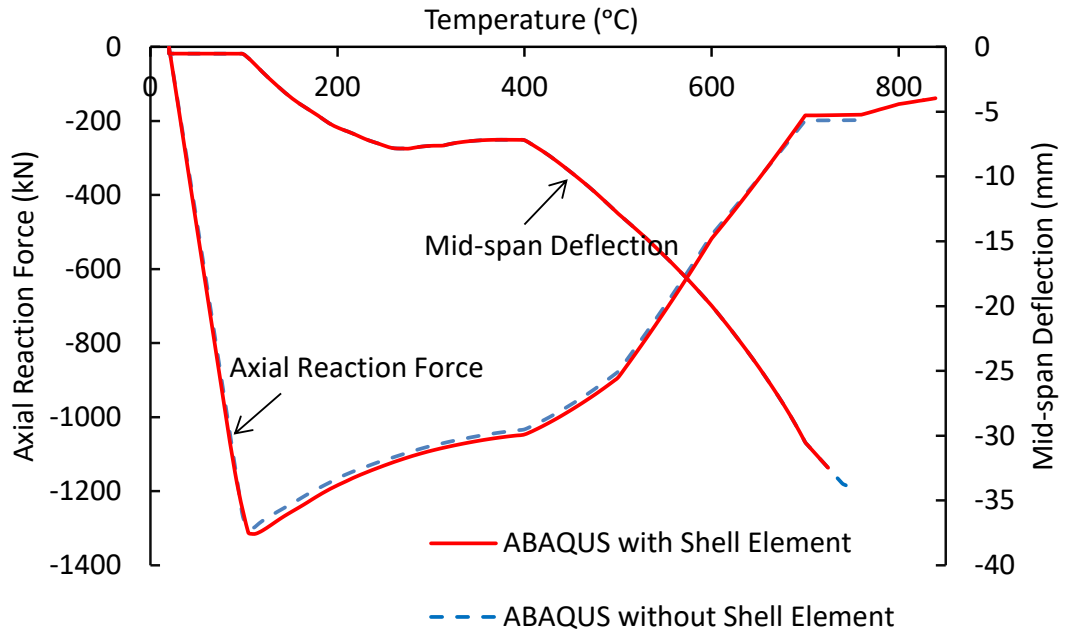

Figure 6-19 Comparison of the ABAQUS results

6.4.2 Illustrative examples of beams with buckling and connection elements

The component-based buckling element has been verified, and the influence of the buckling element on the behaviour of a beam has been demonstrated in Section 6.4.1. In this section the buckling element is used together with the existing component-based connection element of Vulcan to model isolated beams. Models with and without the buckling elements are compared. The influence of the buckling elements on the beam deflection, and on the internal force distribution among the bolt rows of the adjacent connections, are investigated.

The models are of the same dimensions previously used for the 6m and 9m beams described in Section 6.4.1. End-plate connections, designed to be moment resistant in accordance with BS EN 1993-1-8 and its accompanying National Annex, are used. The connection details are shown in Figure 6-20. Grade 8.8 M20 bolts and 15mm thick endplates are used. One purpose of this research is to investigate the influence of the

buckling element on the force distribution within the bolt rows of the adjacent connection. To focus on this, the stress area of all bolts is assumed to be 500mm^2 (instead of the usual nominal value 245mm^2 for M20 bolts) to avoid bolt fracture.

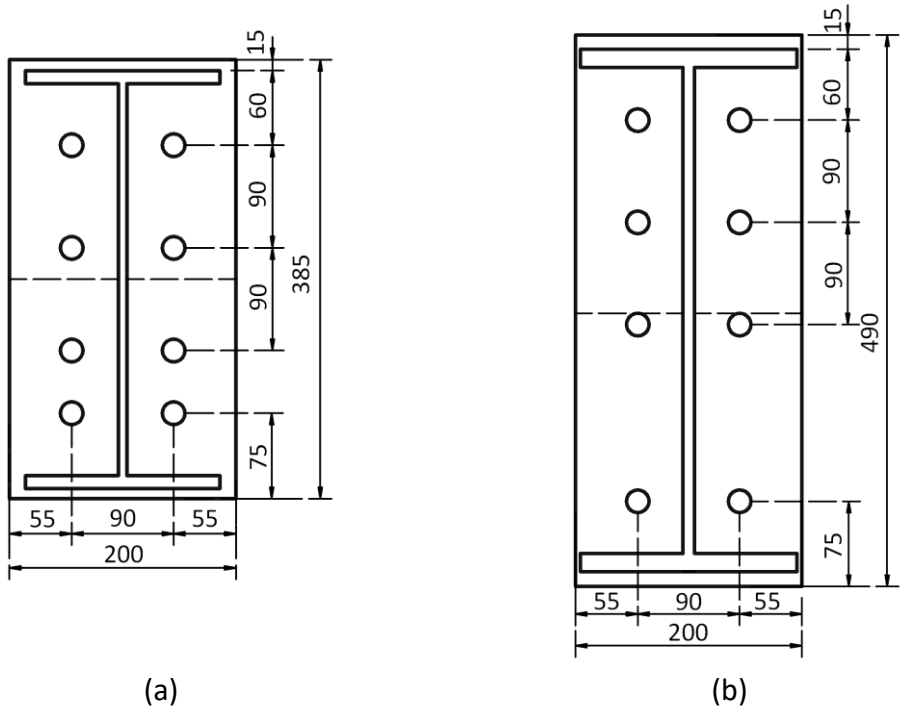

Figure 6-20 Details of the analysed endplate connections: (a) for 6m beams; (b) for 9m beams

Figure 6-21 and Figure 6-22 show comparisons of the force distribution between connection bolt-rows, for beams of different spans (6m and 9m) subject to various load ratios (0.4, 0.5 and 0.6) with and without the buckling element. The component-based connection element is composed of six horizontal springs (two compression springs, representing the top and bottom flanges and four tension springs, representing the bolt rows). The bolt-row springs can only transfer tension force. The general trend is that, in the initial ambient-temperature loading stage, the top three tension bolt-row springs and the bottom flange spring are mobilized to resist the beam-end rotation caused by the external load. After heating starts, the beam starts

to expand and the connections are subjected to a combination of compression and bending. At this stage all the four tension bolt rows are progressively deactivated due to the compression caused by the restraint to thermal expansion. Once all the tension bolt rows are deactivated, the top compression spring starts to work. The deflection of the beam increases dramatically when its temperature increases further, and the four tension bolt rows are progressively re-activated; the top compression spring is switched off. At around 700°C the beams start to develop catenary tension, and the bending action is reduced. Eventually all the four tension bolt rows are again activated, and both compression springs are deactivated.

In Figure 6-21 and Figure 6-22 results for models with and without the buckling element are distinguished by line thickness (thick lines for models with buckling element; thin ones for those without). Colours and marker shapes are used to distinguish different bolt rows. When the tension springs (representing bolt rows) are activated at high temperatures, the thick lines are all below the thin lines. In other words, the tension forces at the bolt rows of a connection are lower when buckling is allowed, compared to the equivalent case without buckling elements. This is reasonable, given the lower rotational stiffness at the beam-end in the presence of local buckling. Therefore, the adjacent connection rotates less, resulting in lower forces in each bolt row. Without buckling elements (thin lines), the forces in the upper bolt rows reach their maximum values at lower temperature. This is because, in this case, the peak spring force corresponds to the yielding of a bolt row, and the upper bolt rows yield earlier than the lower ones as temperature rises. After the upper bolt rows have yielded, more load is distributed to the lower bolt rows, accelerating the yielding of those bolt rows. The decrease in the spring forces after their peak values are due to the reduction of yield strength as temperature increases. On the other

hand, in the cases with buckling elements, the tension forces in all four bolt-rows reach their peaks at the same temperature. The inclusion of the buckling element allows the consideration of the reduction of bending moment at beam-ends at the post-buckling stage. This causes a reversal of the beam-end rotation, resulting in a decrease in the bolt force.

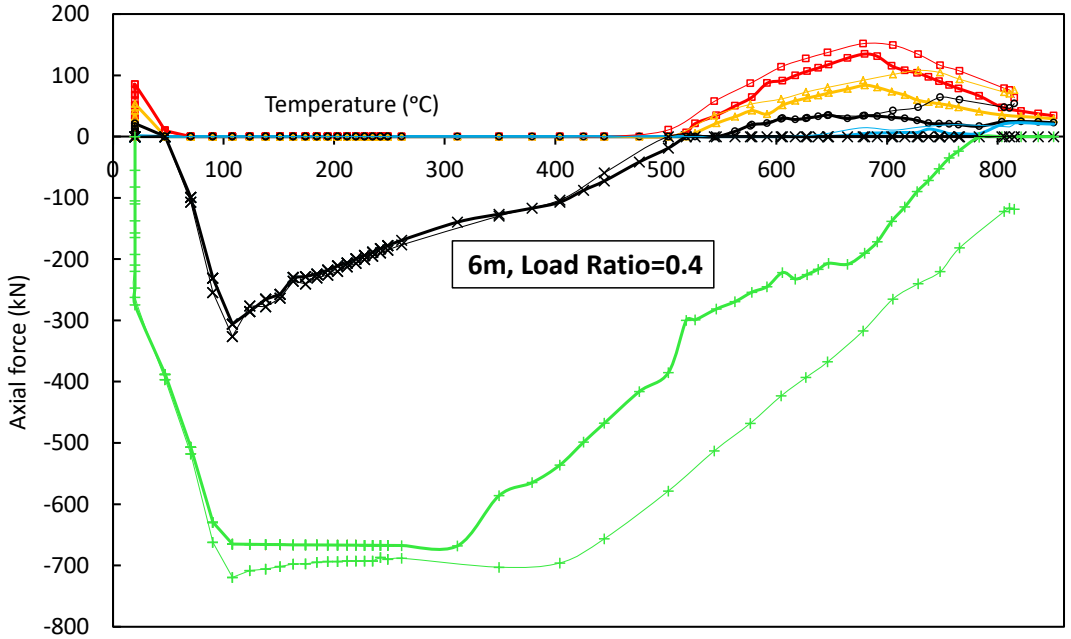

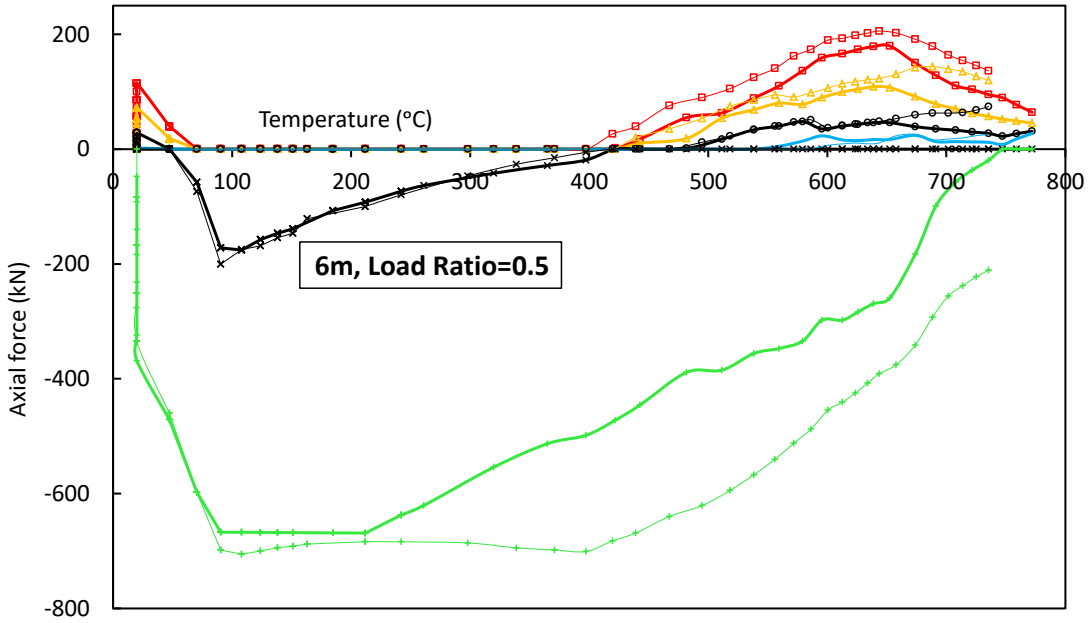

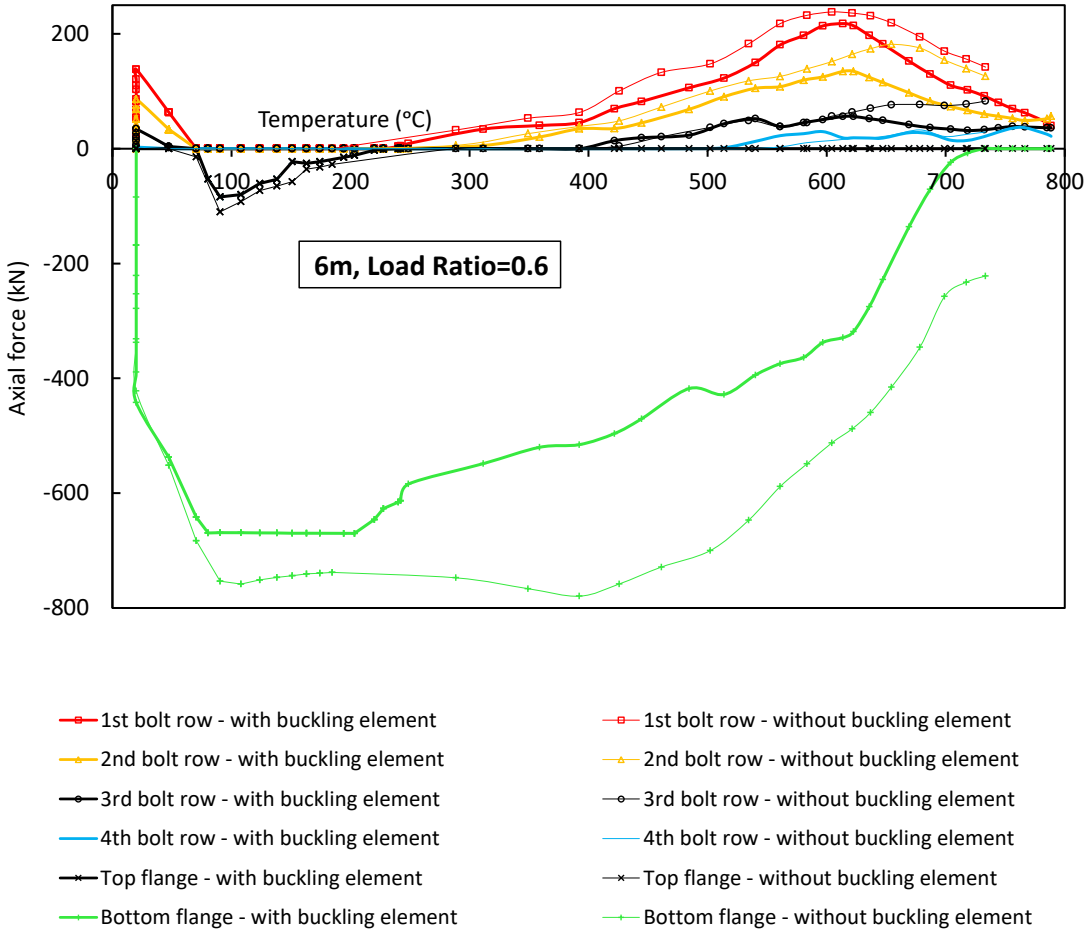

Figure 6-21 Bolt row force distribution for 6m beams

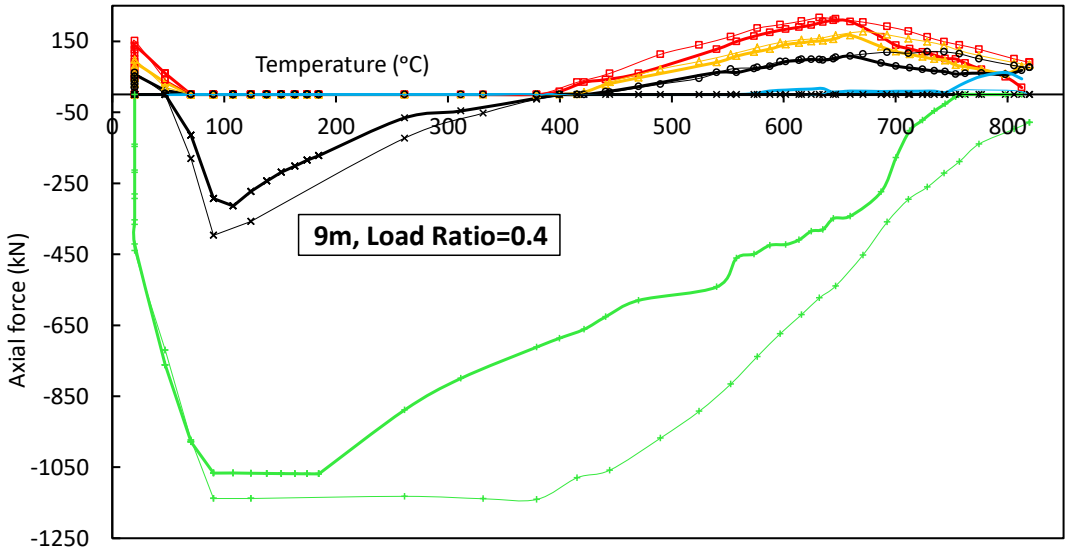

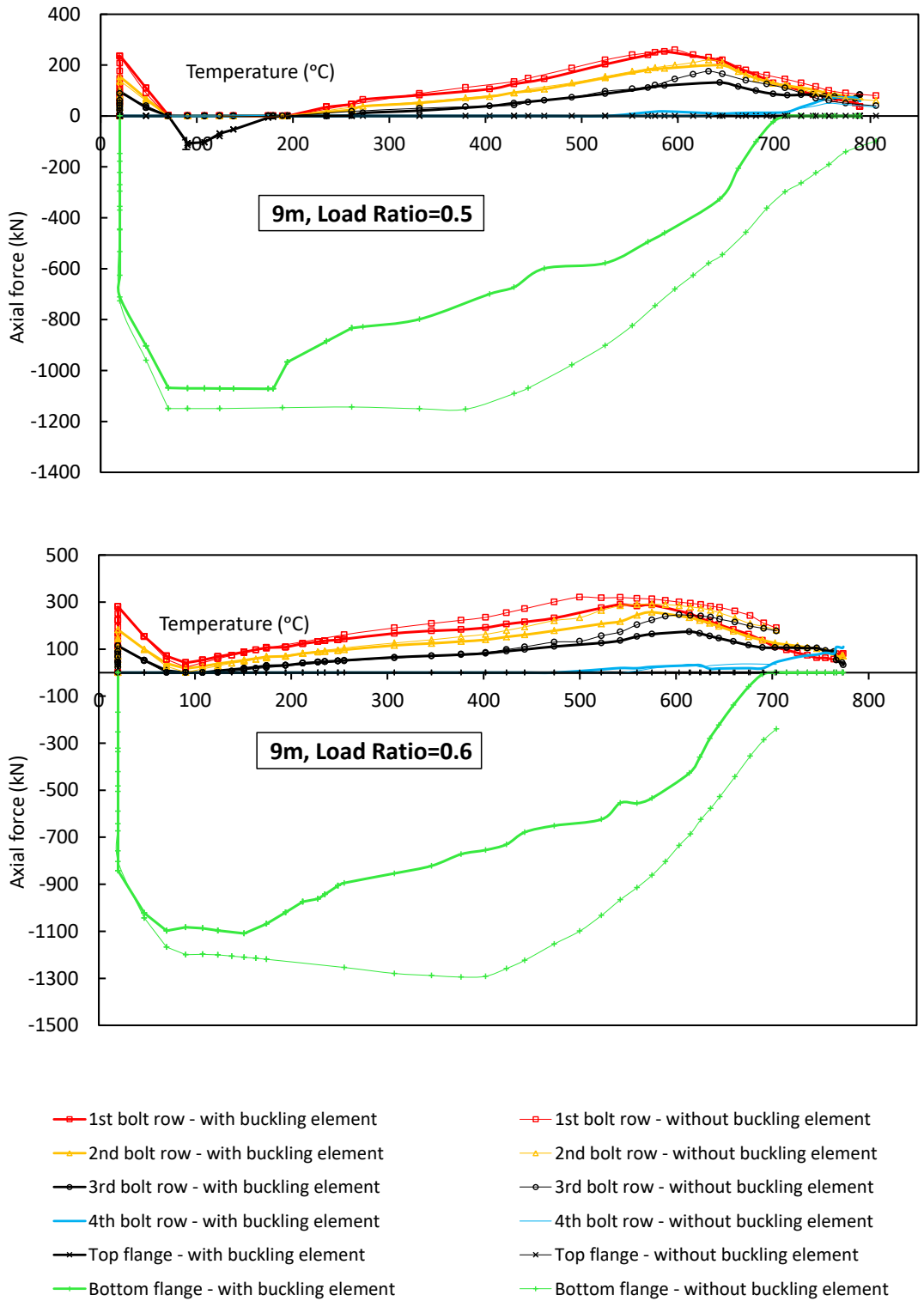

Figure 6-22 Bolt row force distribution for 9m beams

6.4.3 Frame analysis

In order to demonstrate the potential to carry out performance-based analysis considering the buckling element in Vulcan, and to preliminary study the influence of the buckling element on its adjacent connection, a two-storey two-span plane frame model has been created. The dimension of the frame is shown in Figure 6-23. The cross-sections of columns and beams in the frame are UC254×254×73 and UB UB356x171x51 respectively. It is assumed that the fire occurs in the right-hand side bay of the lower storey, and that the beam and columns around this bay are uniformly heated by fire. The temperature of the left and right columns of this bay is 0.8 times the temperature of the beam. The uniformly distributed load applied to the beams is 26.8kN/m, giving them a load ratio of 0.4 for fixed-ended beam. The columns at ground floor level are loaded with a load ratio of 0.15. Flush end-plate connections with the same dimensions as shown in Figure 6-20 (a) are located at the ends of each beam. The stress area of the bolts is set to be 245mm^2. Cases with and without the buckling element have been analysed. For cases with the buckling element, the buckling elements were located in between each connection element and its connected beam. In order to initiate beam-end flange buckling, fully axial restraint has been applied to the frame ends.

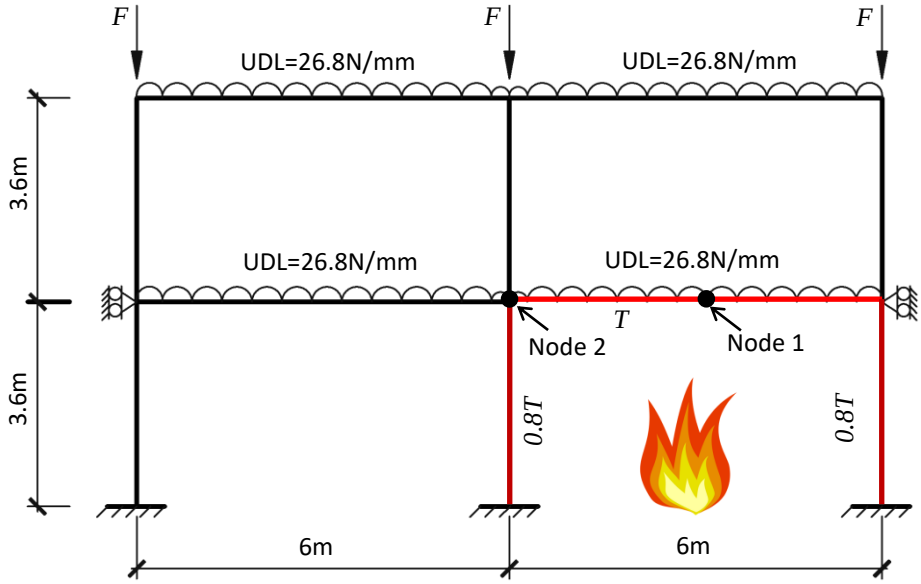

Figure 6-23 Studied frame dimension

Comparison of vertical mid-span deflection (Node 1 in Figure 6-23) has been shown in Figure 6-24. It can be for the frame with the buckling element at beam-ends, the beam deflection increases due to the beam-end local buckling. Beam "run-away" caused by fracture of beam-end connections occurs later for frames with the buckling element.

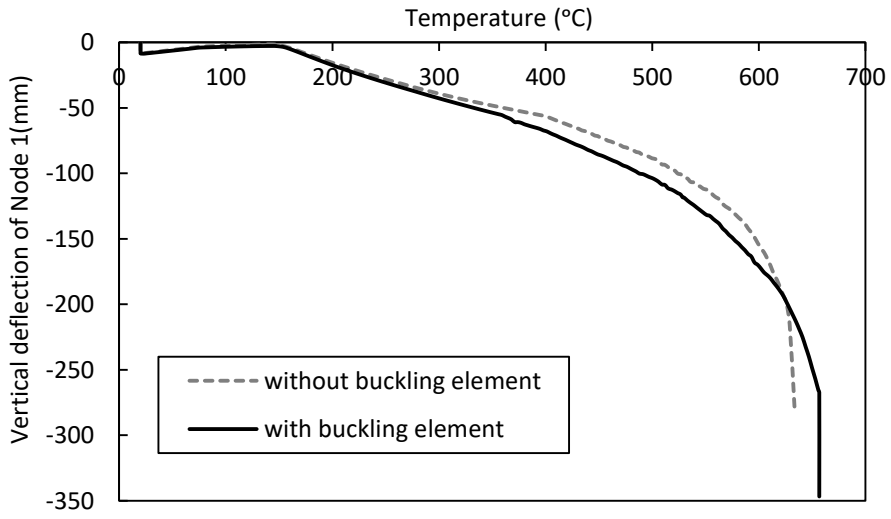

Figure 6-24 Deflections of Node 1 for cases with and without the buckling element

Figure 6-25 plots the the axial forces of different components within the connection at the left hand side of the heated beam. Figure 6-26 plots the detailed tension force within each bolt row. Comparisons of the axial component forces have been made for frames with and without buckling elements. It can been seen from Figure 6-26 that each bolt row with the adjacent buckling element fractures later than the bolt row at the same location but without the buckling element. The program ended when all the connection bolt rows fracture.

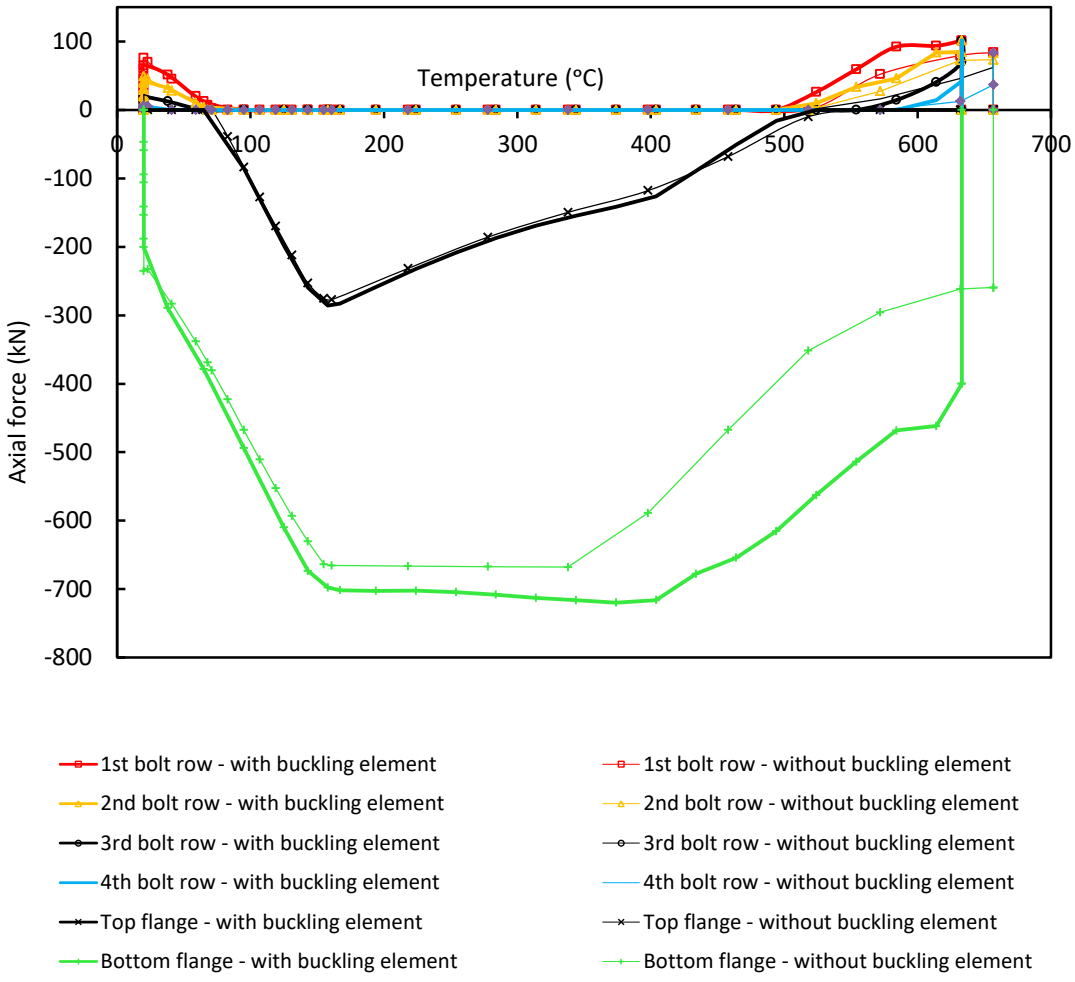

Figure 6-25 Axial forces in different components of the analysed connection

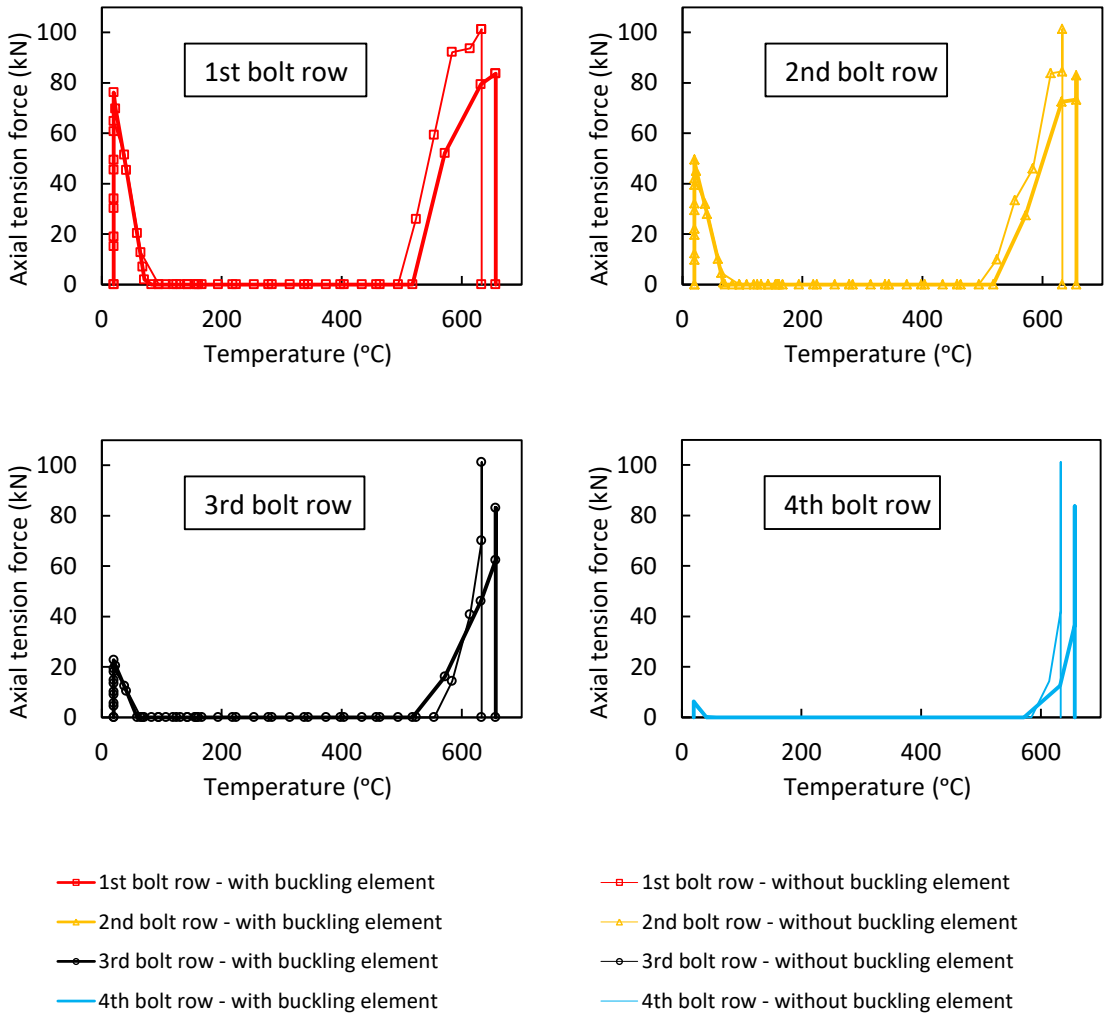

Figure 6-26 Detailed bolt-row forces at Node 2

The vertical and horizontal displacements of Node 2 are shown in Figure 6-27 and Figure 6-28. It can be seen that Node 2 has exactly the same vertical displacements for cases with and without the buckling element. While in the horizontal direction, the latter case has smaller displacement compared with the former case, as shown in Figure 6-28.

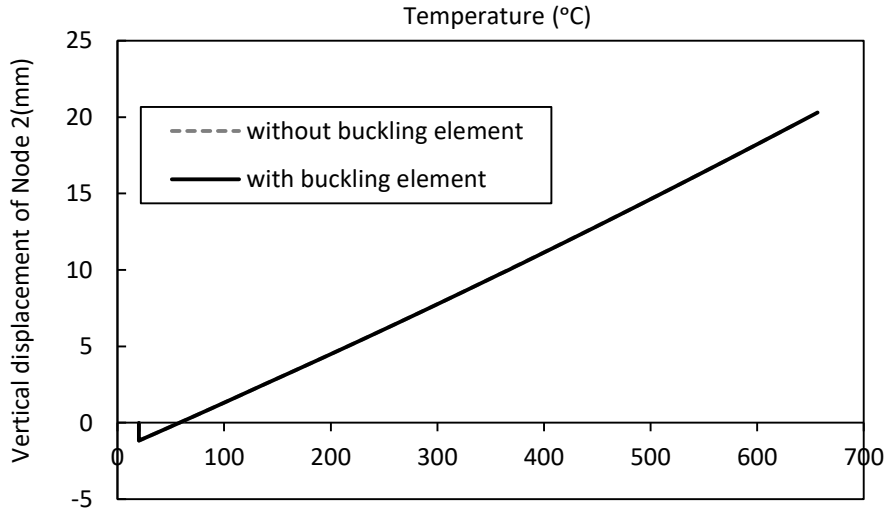

Figure 6-27 Vertical displacement of Node 2

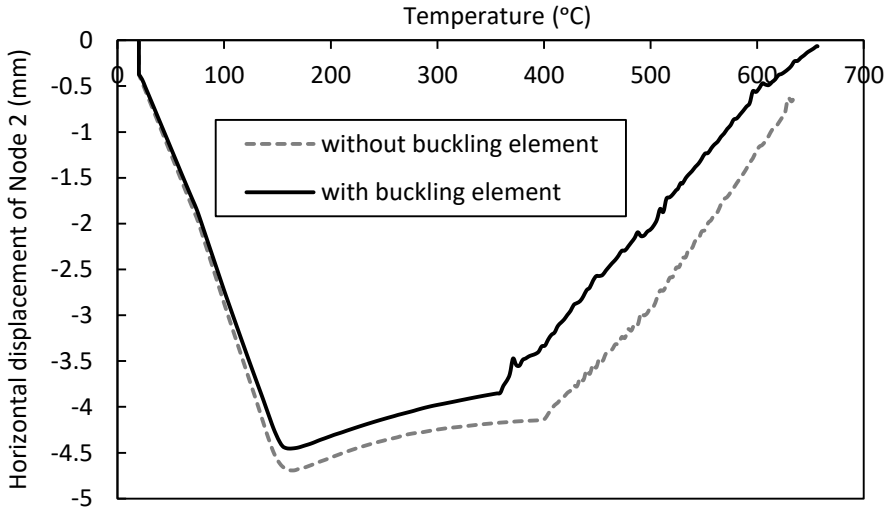

Figure 6-28 Horizontal displacement of Node 2

6.5 CONCLUSION

In this chapter a component-based beam-end buckling element, which considers beam-web shear buckling and bottom-flange buckling within the beam-end buckling zone, has for the first time been created for beams of Classes 1 and 2 sections. The component-based model is able to consider the post-buckling descending force-deflection relationship of its bottom spring, which simulates the bottom-flange

buckling behaviour. Each spring in the buckling element is able to deal with deformation reversal, which commonly happens at high temperatures. The buckling element has been implemented into the global frame analysis software Vulcan. The buckling element has been verified against ABAQUS models on isolated beams. After implementing the buckling element the Vulcan models agree better with the ABAQUS models, compared to the Vulcan models without the buckling elements. It has been observed that, with the buckling element, the temperatures at which the beams' axial forces change from compression to tension have decreased, for some cases by as much as 100°C, which is a considerable decrease in the context of steel beam fire analysis. These temperatures represent the initiation of the catenary stage, at which the beam has no net moment. In Eurocode 3, the beams' design moment resistances are their plastic moment resistances multiplied by reduction factors, considering the effects of high temperatures. It could be reasoned that the initiation temperature of the catenary stage is equivalent to its failure temperature under pure bending, when it forms a plastic mechanism. This mimics the design limit-state critical temperature for isolated beams designed to simple code-of–practice principles. However, it must be remembered that the net zero force condition has been arrived at after considerable plastic straining at different locations within the cross-section, and this has generated a range of different permanent strain values, and hence a stress distribution of a complex shape which simply happens to be in axial equilibrium. The influence of the buckling element on the adjacent connection has also been investigated in isolated beam and in a two-storey two-span plane frame. The results indicate that, by including the buckling element, the net axial compression force and moment transferred from beam to connection have been reduced. Hence, the stresses within the connection bolt rows are reduced when the beam-end buckling is taken into consideration.

Although the bolt forces adjacent to the buckling element are not reduced by a large amount, the trend is consistent for all the cases analysed. Therefore, the existence of the buckling elements tends to protect the adjacent connections, as they decrease the connection bolt-row forces.

7.

SUMMARY, DISCUSSION, CONCLUSIONS AND RECOMMENDATIONS FOR FURTHER WORK

7.1 SUMMARY

Structural analysis under fire conditions has become an essential part of the performance-based design approach. The progressive collapse of the WTC 7 building has emphasized that joints are among the most vulnerable components of structures under fire conditions. Fracture of joints may initiate either locally-contained failures or even progressive collapse of the whole building. Therefore it is necessary to be able to model the behaviour of connections, including their robustness, fracture sequences and survival times. In order to do this one of the most practical approaches is to use a component-based method. Beam-end buckling (including both beam-web shear buckling and bottom-flange buckling) has been widely observed in full-scale fire tests. It may influence the beam survival temperature, the forces transferred to the adjacent connection, as well as the deflection of the beam.

An analytical model was initially created to predict the shear capacity and vertical deflection of shear panels at both ambient and elevated temperatures. The analytical model is capable of predicting the formation of plastic hinges on flanges, the initiation of beam-web shear buckling and the limiting conditions for Class 1 and 2 sections. A tri-linear curve can be created for a particular beam section by linking these three points, in order to track the load-deflection route of the shear panel. For beams for which beam-web shear bucking is the main 'failure' mode, the proposed method provides satisfactory accuracy in terms of both shear capacity and mid-span vertical deflection. However, as beam lengths are increased, the 'failure' mode switches to bottom-flange buckling. However, bottom-flange buckling has not been involved in the beam-web shear buckling analytical model.

An analytical model was also proposed considering simultaneous beam-web shear buckling and bottom-flange buckling. The interaction between these two buckling modes is accounted for by ensuring compatibility between the out-of-plane deflections of the beam web caused by these two modes. Two comparison cases, both with and without uniformly distributed load on top of the buckling panel, were discussed. An example hand-calculation using the validated beam-end buckling panel model, integrated into a whole beam, has been given. The theoretical results have been validated against finite element modelling using ABAQUS over a range of geometries. The second analytical model was also compared with Dharma's analytical model. These comparisons have shown that the proposed model provides sufficiently accurate and conservative results for both Class 1 and 2 sections.

A transition length to distinguish between cases in which pure beam-web shear buckling occurs and those in which the instability is a combination of shear buckling and bottom-flange buckling has been proposed, including a calculation procedure to detect the transition length between these two buckling modes. This criterion was validated using two sets of beams analysed using ABAQUS. It has been observed from the results that, when the beam length is less than the transition length, shear buckling is the dominant buckling mode. The shear-buckling model then provides the best representation, and the analytical shear buckling curve provides the best fit to the FE results. In this range the analytical results for the model which includes bottom-flange buckling lie above both the shear buckling curve and the FE results, indicating that bottom-flange buckling is unlikely to occur. When the beam length is longer than the transition length, a combination including bottom-flange buckling dominates. The analytical results for the model which includes bottom-flange buckling then compare

well with the FE analysis, and the analytical results for the pure shear buckling model lie above the other two curves. For the beams with lengths in the vicinity of the transition length the FEA, shear buckling and bottom-flange buckling results tend towards being identical. The transition lengths observed from the FE modelling, and the comparison between the analytical and FE models, show consistency in transition length according to the calculation criteria for the two groups of beams analysed. Therefore, it is suggested that this calculation procedure (Figure 5-1) is a simplified and effective way to detect the transition length between pure beam-web shear buckling and a combination with bottom-flange buckling of a beam. This transition criterion is only available when the analysed beam is axially released. When the beam is axially restrained, it is assumed that a combination buckling mode will always occur.

For the first time a component-based beam-end buckling element, which considers beam-web shear buckling and bottom-flange buckling within the beam-end buckling zone, has been created for Class 1 and 2 sections. The component-based model is composed of two nonlinear springs. Each spring is able to deal with the reversal of spring deformation, to simulate the strain reversal which very often happens within a heated structure, and which is therefore essential to consider during modelling. The component-based buckling element has been implemented within Vulcan. It has been verified against ABAQUS models in isolated beam cases. A parametric study including both isolated-beam cases and sub-frame analyses with connections was then carried out. Results were compared for the same cases, but with and without the inclusion of buckling elements. The influence of the buckling element on the structural response, including the beam deflection and connection force transmission, have been analysed.

7.2 DISCUSSION AND CONCLUSIONS

This research was inspired by the fact that both beam-web shear buckling and bottom-flange buckling phenomena have been widely observed in full-scale fire tests, such as the Cardington Fire Tests, as well as in accidental fires. Before this research had been carried out, views on the effects of beam-end buckling on the connections adjacent to the buckling zone varied. One speculation was that, after the beam-end buckling occurred, the top bolt row would be seriously stretched due to the possibly large rotation of the beam-end, and therefore top bolt row fracture could be a key factor which might initiate member failure or even progressive collapse of a whole building. The influence of these occurrences of beam-end buckling in the vicinity of the beam-to-column connections of Class 1 and 2 steel sections under fire conditions include beam survival temperature, effects on the adjacent connection bolt-row force distribution, connection survival times and beam deflections.

It has been observed in experiments at a practical scale that bottom-flange buckling is invariably accompanied by beam-web shear buckling. The rotation of the bottom beam flange induces inevitable out-of-plane deflection of the beam web due to deformation compatibility between the beam web and flange. However, it is often assumed, particularly for plate-girders with thin webs, that beam-web shear buckling can occur without accompanying flange buckling, although there is some minor rotation of the bottom-flange. For steel beams at elevated temperatures, it is therefore possible that either beam-web shear buckling or a combination of beam-web shear buckling and bottom-flange buckling can occur. The occurrence of shear buckling is influenced by the beam-end shear force, while the combination of both can be triggered by compression force in the bottom flange, in combination with shear.

This compression force can be generated either by beam-end hogging moment or a combination of hogging moment and axial compression force due to restraint of thermal expansion. This indicates that the combination of both buckling phenomena tends to occur for steel beams with high axial restraint at high temperatures, because such cases tend to produce a large net compression force, of which the beam bottom flange force is usually a major component. The buckling type at the beam-end depends on factors including beam-web aspect ratio, flange aspect ratio, beam length, external load level, temperature and boundary conditions. This research has been limited to beams in steel-framed construction, which would normally imply structures with wind bracing around their perimeters. This bracing resists horizontal movements of the structure, and therefore constrains the beams, producing large axial compressive forces in the beams when they attempt to expand. For steel-framed beams without bracing (typically in buildings with bracing concentrated into a central core), the edge columns can be pushed out without applying much restraint to beam thermal expansion. In such cases, bottom-flange buckling may not be initiated.

When a combination of beam-web shear buckling and bottom-flange buckling occurs, the axial resistance of the bottom flange decreases as it deforms. This decrease leads to reductions in the net beam-end axial and rotational stiffness. The column-face connection is now located in series with a new rotational element, due to the compressive displacement of the lower beam flange, which tends to rotate about a centre near to the top bolt row. This leads to an increase of net beam-end rotation, and therefore increased mid-span deflection. The net axial compression force may be relieved due to the large compressive deformation of the buckling zone. The bending moment in the buckling zone decreases because of the reduction of rotational stiffness

at the beam-end. This implies lower forces to be resisted by the connection itself. Hence, the stresses within the connection bolt rows tend to decrease when the buckling element is taken into consideration. In general, by ignoring the buckling element near to the beam-to-column connections in structural fire analysis, the results tend to be on the safe side in terms of connection forces. In practical design based on the Eurocode 3, the beam survival temperature is the temperature at which the beams' axial forces change from compression to tension, when beams' plastic moment resistance decrease to zero. It could be reasoned that the initiation temperature of the catenary stage is equivalent to its failure temperature under pure bending, when it forms a plastic mechanism. This mimics the design limit-state critical temperature for isolated beams designed to simple code-of–practice principles.

7.3 RECOMMENDATIONS FOR FURTHER WORK

Within the duration of a PhD project it is inevitable that some desirable further developments of the research become apparent. A component-based beam-end buckling model has been created in the form of a buckling element, as reported above. This model has been applied to steel-framed structures. The following issues relate to the PhD research done, and should be considered in future research work.

7.3.1 Behaviour of connections in fire

Several types of connections, such as fin plates, web cleats, flush, extended and flexible end-plates, are commonly used in steel construction. The deformation types, bolt-row force distributions and failure mechanisms vary between these types, because of differences in their internal force distribution mechanisms. The current study has only been considered extended end-plate connections with a limited range of layouts and dimensions. The purpose of this has been to present examples which

combine the component-based buckling element and a practical component-based connection element in Vulcan, and to demonstrate the effects of the buckling element on their local loading in fire conditions. Analyses need to be carried out on other connection types, which have previously been shown to have very different characteristics under combined loading. Parametric studies need particularly to investigate different combinations of connection and beam-end flexibility. A general-purpose component-based connection model actually exists (Dong et al., 2015) within Vulcan, and this can be used with the component characterizations produced by various researchers (Sarraj, 2007, Yu et al., 2009c, Taib and Burgess, 2011) to represent connections of many different types. These can be combined with buckling elements derived from different beam section dimensions so that the relationship between connection ductility and beam buckling properties can be controlled quantitatively. It should be possible to investigate the robustness of such combinations and to attempt to develop principles to optimize this robustness.

7.3.2 Progressive collapse of buildings

It has been illustrated in the previous chapters that, by including component-based beam-end buckling elements, the survival times of adjacent connections will be influenced. In the time available for the work only two-span two-storey case studies have been carried out, attempting to analyse quantitatively the influence of the buckling elements on their adjacent connections. The analysis terminates when the connection bolt rows completely fracture. Surrounding structure has been modelled to simulate the constraint conditions of individual beams. It is clear that more complex models need to be analysed, with boundary conditions closer to real cases. Moreover, the progressive collapse of buildings can be historically-related. For instance, the

horizontal force transferred from the beam to its attached column can differ, with and without the bucking element, before the beam-to-column connections fracture. Therefore, the initial deflections of the columns can vary after an attached beam has fallen and frame stability has been regained. In the context of Vulcan analysis the component-based buckling element is expected to be used in combination with the static-dynamic procedure created by Sun (2012b). By involving the buckling element, it will be possible to carry out more accurate performance-based fire analysis using Vulcan.

7.3.3 Three-dimensional composite beam analysis at non-uniformly distributed temperatures

It has been stated in Chapter 6 that the component-based buckling element is able to deal with buckling problems considering different axial forces. In Chapter 6, the buckling element was applied to steel beams with axial restraint, and the results compared well with finite element analysis. This further showed that the buckling element is able to deal with axial force automatically, as axial restraint is actually providing a larger compressive force to the buckling element. Based on this premise, it is reasonable that the component-based buckling element should be expected to be applied to the analysis of composite floor systems at non-uniformly distributed temperatures.

For beams at non-uniformly distributed temperatures, one key effect is that non-uniformly distributed axial force across the beam depth will be produced. As the buckling springs are able to deal with different axial forces automatically, it is possible that the buckling element could consider non-uniformly distributed temperatures of the beam. However, as the horizontal springs are only located at the top and bottom

of the beam, it is only able to consider different temperatures at these two locations on the cross section of the buckling element.

In three-dimensional composite floors, the concrete slabs will restrain the steel beams from expansion. This is because on the one hand, most of the depth of the concrete slab will have much lower temperatures than the unprotected steel beam underneath; on the other hand, the thermal expansion of the concrete slab itself can be restrained by any surrounding cooler slabs. The restraint from the composite slab restrains the top flange of the steel beam from thermal expansion, and thus the net steel cross-section acquires an induced compressive force which is balanced by tension in the attached concrete slab; the lever arm between these two force resultants causes a bending moment which forces the beam into thermal bowing towards the fire. In a 3-dimensional slab, as against a simple composite beam, the thermal bowing is restrained by the continuity away from any one heated beam, as well as by restraint to thermal expansion, and therefore the compressive force in the bottom flange is increased. This large compressive force, together with weakening of the steel as its temperature rises, trigger bottom-flange buckling even though no strong bracing has been applied to the frame. Such beam-end bottom-flange buckling can be widely observed in photos (Newman et al., 2000) from the Cardington composite-framed Fire Tests.

The analytical models (including both pure beam-web shear buckling and the combination of beam-web shear buckling and bottom-flange buckling) are based on the principle of plastic work-balance, which is a variant of the principle of stationary potential energy for rigid-plastic systems. Therefore, selection of the appropriate yield line mechanism is a key factor. Any change of yield-line mechanism will induce a

change of the internal work, influencing the force-deflection relationship of the buckling element. In extending the analytical buckling models from steel to composite beams, it is necessary to check whether the yield-line mechanism is still applicable. For instance, for a composite beam-end subjected to hogging moment, the reinforcement within the concrete slab carries tension force instead of the top flange of the steel beam. Therefore, a new yield zone in the reinforcing mesh may replace the initial plastic zone in the beam top flange when creating the analytical model. It may be possible to establish an equivalent-section criterion so that the analytical model can be consistently applied to both steel and composite beams. The analytical results can be compared with the existing full-scale fire tests (eg. the Cardington Fire Tests) for further validation.

7.3.4 Buckling of cellular beams

A cellular beam is I-section beam with an array of holes along its web. It is currently widely used, due to its ability to achieve large-spans while accommodating building services within the structural depth of beam. The buckling behaviour of cellular beams under fire conditions has not been sufficiently investigated. Due to the natural relationship between cellular beams and I-section beams, it is reasonable to expect that any analytical buckling model should be applicable, with appropriate modifications, to cellular beams in the post-buckling stage.

The weakening of the webs of cellular beam makes it easier for beam-web shear buckling to occur compared with I-section beams. If a combined buckling mode occurs, the yield line mechanism may not change at the bottom flange, but significant differences can be expected on the web, since it is very possible that only a part of the beam web within the flange buckling zone. Therefore, the yield line mechanism for the

beam web has to be reconsidered for cellular beams. Both the criterion for its occurrence and the buckling region affected may be influenced by the distance between two adjacent holes (the width of a “web-post”), the positions of the holes and the height of the cellular beam.

A component-based buckling element has been created to simulate the plastic post-buckling behaviour of steel beams in fire. By implementing this element into the three-dimensional structural fire analysis software Vulcan, it enables to consider the effects of the buckling elements on the robustness design of their adjacent connections. Examples of isolated beams with the buckling element and the connection element have been illustrated in this research. It can be expected that the buckling element be involved in more complex performance-based frame analysis and be combined with explicit dynamic procedure to simulate local and progressive collapse of a whole building.

REFERENCES

AL-JABRI, K., BURGESS, I., LENNON, T. & PLANK, R. 2005. Moment–rotation–temperature curves for semi-rigid joints. *Journal of Constructional Steel Research,* 61**,** 281-303.

AL-JABRI, K. S. 2011. Modelling and simulation of beam-to-column joints at elevated temperature: a review. *Journal of the Franklin Institute,* 348**,** 1695-1716.

AL-JABRI, K. S., DAVISON, J. B. & BURGESS, I. W. 2008. Performance of beam-to-column joints in fire—a review. *Fire Safety Journal,* 43**,** 50-62.

ANDERSON, D. & NAJAFI, A. 1994. Performance of composite connections: major axis end plate joints. *Journal of Constructional Steel Research,* 31**,** 31-57.

ASFP 2010. *Fire Protection for Structural Steel in Buildings (The Yellow Book),* UK, The Steel Construction Institute.

ASIC 1963. *Specification for the design, fabrication and erection of structural steel for building*, American Institute of Steel Construction.

BAILEY, C. & MOORE, D. 2000a. The structural behaviour of steel frames with composite floorslabs subject to fire. Part. 1: theory. *Structural Engineer,* 78(11)**,** 19-27.

BAILEY, C. & MOORE, D. 2000b. The structural behaviour of steel frames with composite floorslabs subject to fire. Part. 2: design. *Structural Engineer,* 78(11)**,** 28-33.

BAILEY, C. G. 2004. Membrane action of slab/beam composite floor systems in fire. *Engineering structures,* 26**,** 1691-1703.

BASLER, K. 1961a. Strength of plate girder in shear. *Journal of the Structural Division ASCE,* 87(ST7)**,** 151-80.

BASLER, K. 1961b. Strength of plate girder under conbined bending and shear. *Journal of the Structural Division ASCE,* 87(ST7)**,** 181-97.

BASLER, K., YEN, B., MUELLER, J. & THURLIMANN, B. 1960. *Web buckling tests on welded plate girders*, Fritz Engineering Laboratory, Lehigh University.

BLOCK, F. M. 2006. *Development of a component-based finite element for steel beam-to-column connections at elevated temperatures.* PhD thesis, University of Sheffield.

BLOCK, F. M., BURGESS, I. W., DAVISON, J. B. & PLANK, R. J. 2007. The development of a component-based connection element for endplate connections in fire. *Fire Safety Journal,* 42**,** 498-506.

BRITISH STEEL TECHNICAL, 1987. *BS 476 Fire Tests on Building Materials and Structures*, London, UK.

BRITISH STANDARDS INSTITUTE, 1990. *BS 5950: Structural use of steel work in building: Part 8: Code of practice for fire resistant design*. London, UK

BURGESS, I. Connection modelling in fire. *Proceedings of COST C26 workshop urban habitat constructions under catastrophic events*, Prague, 2007. 25-34.

BURGESS, I. the Influence of Connections on the Robustness of Composite Structures in Fire. HKIE Fire Division one-day Symposium 2010: *Fire Engineering for a Sustainable Future*, 2010.

BURGESS, I., DAVISON, J. B., DONG, G. & HUANG, S.-S. 2012. The role of connections in the response of steel frames to fire. *Structural Engineering International,* 22**,** 449-461.

BURGESS, I., HUANG, S. & STAIKOVA, S. A re-examination of the mechanics of tensile membrane action in composite floor slabs in fire. *8th International Conference on Structures in Fire*, 2014.

CEN 2005a. *BS EN 1993-1-1: Design of steel structures. Part 1.1: General structural rules.* British Standards Institution.

CEN 2005b. *BS EN 1993-1-2. Design of steel structures. Part 1.2: General rules — Structural Fire Design.* British Standards Institution.

CEN 2005c. *BS EN 1993-1-8. Design of steel structures, Part 1.8: Design of joints.* European Committee for Standardization.

CEN 2005d. *BS EN 1994-1-2. Design of steel structures. Part 1.2: General rules — Structural Fire Design.* British Standards Institution.

CEN 2005e. *BS EN 1994-1-8. Design of steel structures, Part 1.8: Design of joints.* European Committee for Standardization.

CEN 2006. *BS EN 1993-1-5. Eurocode 3. Design of steel structures. Part 1.5: Plated structural elements.* British Standards Institution.

CLIMENHAGA, J. J. & JOHNSON, R. P. 1972. Moment-rotation curves for locally buckling beams. *Journal of the Structural Division,* 98**,** 1239-1254.

COOKE, G. & LATHAM, D. 1987. The inherent fire resistance of a loaded steel framework. *Steel Construction Today,* 1**,** 49-58.

DA SILVA, L. S., SANTIAGO, A. & REAL, P. V. 2001. A component model for the behaviour of steel joints at elevated temperatures. *Journal of Constructional Steel Research,* 57**,** 1169-1195.

DHARMA, R. & TAN, K. 2008. Experimental and numerical investigation on ductility of composite beams in the Hogging moment regions under fire conditions. *Journal of structural engineering,* 134**,** 1873-1886.

DHARMA, R. B. 2007. *Buckling behaviour of steel and composite beams at elevated temperatures.* PhD thesis, Nanyang Technological University.

DHARMA, R. B. & TAN, K.-H. 2007a. Rotational capacity of steel I-beams under fire conditions Part I: Experimental study. *Engineering structures,* 29**,** 2391-2402.

DHARMA, R. B. & TAN, K.-H. 2007b. Rotational capacity of steel I-beams under fire conditions Part II: Numerical simulations. *Engineering structures,* 29**,** 2403-2418.

DONG, G., BURGESS, I., DAVISON, B. & SUN, R. 2015. Development of a general component-based connection element for structural fire engineering analysis. *Journal of Structural Fire Engineering,* 6**,** 247-254.

ELGHAZOULI, A. & IZZUDDIN, B. Significance of local buckling for steel frames under fire conditions. *4th International Conference on Steel and Aluminium Structures*, 1999. 727-734.

FABIEN, Q., BURGESS, I. & HUANG, S.-S. Development and modification of yield line patterns in thin slabs subjected to tensile membrane action. *9th International Conference on Structures in Fire*, 2016.

FOSTER, S., BAILEY, C., BURGESS, I. & PLANK, R. 2004. Experimental behaviour of concrete floor slabs at large displacements. *Engineering structures,* 26**,** 1231-1247.

FRANSSEN, J. 2011. User's manual for SAFIR 2011 a computer program for analysis of structures subjected to fire. *University of Liege, Belgium*.

FUJII, T. On an improved theory for Dr. Basler's theory. *Proceeding of 8th Congress*, IABSE, New York, 1968. 477-487.

GALAMBOS, T. V. 1998. *Guide to stability design criteria for metal structures*, Structure Stability Research Council.

GANN, R. 2005. NIST NCSTAR 1: Final report of the national construction safety team on the collapse of the world trade center twin towers. *Federal Building and Fire Safety Investigation of the World Trade Center Disaster. Gaithersburg,(MD): National Institute of Standards and Technology (NIST)*.

GANN, R. G. 2008. Final Report on the Collapse of World Trade Center Building 7,Federal Building and Fire Safety Investigation of the World Trade Center Disaster. *The National Institute of Standards and Technology (NIST)***,** 130.

GERSTLE, K. H. 1988. Effect of connections on frames. *Journal of Constructional Steel Research,* 10**,** 241-267.

GIONCU, V. & MAZZOLANI, F. 2003. *Ductility of seismic-resistant steel structures*, CRC Press.

GIONCU, V. & PETCU, D. 1995. Numerical investigations on the rotation capacity of beams and beam-columns. *Proceedings of International Colloquim Stability of Steel Structures. Further Direction in Stability Research and Design, European Session,* 1**,** 163-174.

GIONCU, V. & PETCU, D. 1997. Available rotation capacity of wide-flange beams and beam-columns Part 1. Theoretical approaches. *Journal of Constructional Steel Research,* 43**,** 161-217.

GUO, S. 2012. Experimental and numerical study on restrained composite slab during heating and cooling. *Journal of Constructional Steel Research,* 69**,** 95-105.

HANTOUCHE, E. G., ABBOUD, N. H., MOROVAT, M. A. & ENGELHARDT, M. D. 2016. Analysis of steel bolted double angle connections at elevated temperatures. *Fire Safety Journal,* 83**,** 79-89.

von Mises, R. 1913. Mechanik der festen Körper im plastisch deformablen Zustand. Göttin. Nachr. Math. Phys., vol. 1, pp. 582–592.

HIBBIT, D., KARLSSON, B. & SORENSON, P. 2005. ABAQUS reference manual 6.7. *Pawtucket: ABAQUS Inc*.

HUANG, S.-S., DAVISON, B. & BURGESS, I. W. 2013. Experiments on reverse-channel connections at elevated temperatures. *Engineering structures,* 49**,** 973-982.

HUANG, Z., BURGESS, I. & PLANK, R. 1999a. Three-dimensional modelling of two full-scale fire tests on a composite building. *Proceedings of the Institution of Civil Engineers. Structures and buildings,* 134**,** 243-255.

HUANG, Z., BURGESS, I. W. & PLANK, R. J. 1999b. The influence of shear connectors on the behaviour of composite steel-framed buildings in fire. *Journal of Constructional Steel Research,* 51**,** 219-237.

HUANG, Z., BURGESS, I. W. & PLANK, R. J. 2000. Three-dimensional analysis of composite steel-framed buildings in fire. *Journal of structural engineering,* 126**,** 389-397.

HUANG, Z., BURGESS, I. W. & PLANK, R. J. 2003a. Modeling membrane action of concrete slabs in composite buildings in fire. I: Theoretical development. *Journal of structural engineering,* 129**,** 1093-1102.

HUANG, Z., BURGESS, I. W. & PLANK, R. J. 2003b. Modeling membrane action of concrete slabs in composite buildings in fire. II: Validations. *Journal of structural engineering,* 129**,** 1103-1112.

ISO834 1975. *International Standard 834: Fire Resistance Test - Elements of building construction*, International Organization for Standardization, Geneva, Switzerland.

CHIANG, D.-Y. 1999. The generalized Masing models for deteriorating hysteresis and cyclic plasticity. *Applied Mathematical Modelling*, 23, 847-863.

JUNIOR, V. S. & CREUS, G. 2007. Simplified elastoplastic analysis of general frames on fire. *Engineering structures,* 29**,** 511-518.

KATO, B. 1965. Buckling strength of plates in the plastic range. *Publications of IABSE,* 25.

KOUVELIS, P. & YU, G. 2013. *Robust discrete optimization and its applications*, Springer Science & Business Media.

KUHLMANN, U. 1986. *Rotationskapazität biegebeanspruchter I-Profile unter Berücksichtigung des plastischen Beulens*, Inst. für Konstruktiven Ingenieurbau, Ruhr-Univ.

LEE, S. C., LEE, D. S. & YOO, C. H. 2008. Ultimate shear strength of long web panels. *Journal of Constructional Steel Research,* 64**,** 1357-1365.

LEE, S. C. & YOO, C. H. 1998. Strength of plate girder web panels under pure shear. *Journal of Structural Engineering,* 124**,** 184-204.

LENNON, T. & MOORE, D. 2004. Results and observations from full-scale fire test at BRE Cardington, 16 January 2003. *BRE, Watford, UK*.

LI, G.-Q. & GUO, S.-X. 2008. Experiment on restrained steel beams subjected to heating and cooling. *Journal of Constructional Steel Research,* 64**,** 268-274.

LIEN, K., CHIOU, Y., WANG, R. & HSIAO, P. 2010. Vector form intrinsic finite element analysis of nonlinear behavior of steel structures exposed to fire. *Engineering structures,* 32**,** 80-92.

LIEW, J. R. & CHEN, H. 2004. Explosion and fire analysis of steel frames using fiber element approach. *Journal of structural engineering,* 130**,** 991-1000.

LIU, T., FAHAD, M. & DAVIES, J. 2002. Experimental investigation of behaviour of axially restrained steel beams in fire. *Journal of Constructional Steel Research,* 58**,** 1211-1230.

LTD, V. E. 2015. Sheffield. Available: http://www.vulcan-eng.com/ 2015].

MALHOTRA, H. L. 1980. Fire resistance versus fire behaviour. *Fire Prevention,* 134**,** 4.

MCALLISTER, T. & CORLEY, G. 2002. *World Trade Center Building performance study: Data collection, preliminary observations, and recommendations*, Federal Emergency Management Agency.

NAJJAR, S. & BURGESS, I. 1996. A nonlinear analysis for three-dimensional steel frames in fire conditions. *Engineering structures,* 18**,** 77-89.

NEWMAN, G. 2000. A NEW APPROACH TO MULTI-STOREY STEEL FRAMED BUILDINGS Large-Scale fire tests have shown that the fire performance of real buidings is much better than expected. *FIRE SAFETY ENGINEERING,* 7**,** 14-19.

NEWMAN, G. M., ROBINSON, J. T. & BAILEY, C. G. 2000. *Fire safe design: A new approach to multi-storey steel-framed buildings*, Steel Construction Institute Ascot.

NIST 2008. Federal Building and Fire Safety Investigation of the World Trade Centre Disaster: Structural Response and Probable Collapse Sequence of World Trade Centre Building 7. Gaithersburg: NIST Report NCSTAR 1-9(2).

O'CONNOR, M. & MARTIN, D. 1998. Behaviour of a multi-storey steel framed building subjected to fire attack. *Journal of Constructional Steel Research,* 1**,** 295.

PEARSON, C. & DELATTE, N. 2005. Ronan point apartment tower collapse and its effect on building codes. *Journal of Performance of Constructed Facilities,* 19**,** 172-177.

PORTER, D., ROCKEY, K. & EVANS, H. 1987. *The collapse behaviour of plate girders loaded in shear*, University College Department of Civil and Structural Engineering.

ROCKEY, K., EVANS, H. & PORTER, D. A design method for predicting the collapse behaviour of plate girders*. ICE proceedings*, 1978. Ice Virtual Library, 85-112.

ROCKEY, K. & SKALOUD, M. Influence of flange stiffness upon the load carrying capacity of webs in shear. *8th Congress of IABSE, Final Report*, New York, 1968.

ROCKEY, K. & SKALOUD, M. 1972. The ultimate load behaviour of plate girders loaded in shear. *Struct. Eng,* 50**,** 29-47.

ROTTER, J., SANAD, A., USMANI, A. & GILLIE, M. Structural performance of redundant structures under local fires. *Proceedings of Interflam*, 1999.

SAAB, H. & NETHERCOT, D. 1991. Modelling steel frame behaviour under fire conditions. *Engineering structures,* 13**,** 371-382.

SARRAJ, M. 2007. *The behaviour of steel fin plate connections in fire.* University of Sheffield.

SLOTINE, J.-J. E. & LI, W. 1991. *Applied nonlinear control*, prentice-Hall Englewood Cliffs, NJ.

SPYROU, S., DAVISON, J., BURGESS, I. & PLANK, R. 2004a. Experimental and analytical investigation of the 'compression zone'component within a steel joint at elevated temperatures. *Journal of Constructional Steel Research,* 60**,** 841-865.

SPYROU, S., DAVISON, J., BURGESS, I. & PLANK, R. 2004b. Experimental and analytical investigation of the 'tension zone'components within a steel joint at elevated temperatures. *Journal of Constructional Steel Research,* 60**,** 867-896.

STANDARD, B. B. 1990. Structural use of steelwork in building, Part 8: Code of practice for fire resistant design. *British Standard Institution*.

STAROSSEK, U. & HABERLAND, M. 2010. Disproportionate collapse: terminology and procedures. *Journal of Performance of Constructed Facilities,* 24**,** 519-528.

SÜLI, E. & MAYERS, D. F. 2003. *An introduction to numerical analysis*, Cambridge university press.

SUN, R., BURGESS, I. W., HUANG, Z. & DONG, G. 2015. Progressive failure modelling and ductility demand of steel beam-to-column connections in fire. *Engineering structures,* 89**,** 66-78.

SUN, R., HUANG, Z. & BURGESS, I. W. 2012a. The collapse behaviour of braced steel frames exposed to fire. *Journal of Constructional Steel Research,* 72**,** 130-142.

SUN, R., HUANG, Z. & BURGESS, I. W. 2012b. Progressive collapse analysis of steel structures under fire conditions. *Engineering structures,* 34**,** 400-413.

TAIB, M. & BURGESS, I. W. 2011. A Component-Based Model for Fin Plate Connections in Fire. *Proc., Applications of Structural Fire Engineering, Czech Technical Univ., Prague, Czech Republic***,** 225-230.

TAN, K.-H. & HUANG, Z.-F. 2005. Structural responses of axially restrained steel beams with semirigid moment connection in fire. *Journal of structural engineering,* 131**,** 541-551.

TIMOSHENKO, S. P. & GERE, J. M. 1961. Theory of elastic stability. 1961. McGraw-Hill, New York.

TIMOSHENKO, S. P. & GERE, J. M. 2009. *Theory of elastic stability*, Courier Corporation.

TORIĆ, N., SUN, R. R. & BURGESS, I. W. Testing the acceptability of different creep strain calculation models in structural fire analysis. 8th International Conference on Structures in Fire, 2014. 11-13.

TSCHEMMERNEGG, F., TAUTSCHNIG, A., KLEIN, H., BRAUN, CH.HUMER, CH. 1987. Zur Nachgiebigkeit von Rahmenknoten (Semi-rigid joints of frame structures Vol. 1– in German). *Stahlbau 56 Heft 10***,** 299-306.

USMANI, A., DRYSDALE, D., ROTTER, J., SANAD, A., GILLIE, M. & LAMONT, S. 2000. Behaviour of steel framed structures under fire conditions. *University of Edinburgh, Edinburgh*.

USMANI, A., ROTTER, J., LAMONT, S., SANAD, A. & GILLIE, M. 2001. Fundamental principles of structural behaviour under thermal effects. *Fire Safety Journal,* 36**,** 721-744.

VIMONSATIT, V., TAN, K.-H. & TING, S.-K. 2007a. Shear strength of plate girder web panel at elevated temperature. *Journal of Constructional Steel Research,* 63**,** 1442-1451.

VIMONSATIT, V., TAN, K. & QIAN, Z. 2007b. Testing of plate girder web panel loaded in shear at elevated temperature. *Journal of Structural Engineering,* 133**,** 815-824.

WAGNER, H. 1931. *Flat sheet metal girder with very thin metal web*, National Advisory Committee for Aeronautics.

WALD, F., DA SILVA, L. S., MOORE, D., LENNON, T., CHLADNA, M., SANTIAGO, A., BENEŠ, M. & BORGES, L. 2006. Experimental behaviour of a steel structure under natural fire. *Fire Safety Journal,* 41**,** 509-522.

WANG, Y., DAI, X. & BAILEY, C. 2011. An experimental study of relative structural fire behaviour and robustness of different types of steel joint in restrained steel frames. *Journal of Constructional Steel Research,* 67**,** 1149-1163.

WILSON, J. M. 1886. On specifications for strength of iron bridges. *Transactions of the American Society of Civil Engineers,* 15**,** 389-414.

YIN, Y. & WANG, Y. 2004. A numerical study of large deflection behaviour of restrained steel beams at elevated temperatures. *Journal of Constructional Steel Research,* 60**,** 1029-1047.

YIN, Y. & WANG, Y. 2005. Analysis of catenary action in steel beams using a simplified hand calculation method, Part 1: theory and validation for uniform temperature distribution. *Journal of Constructional Steel Research,* 61**,** 183-211.

YOO, C. H. & LEE, S. C. 2006. Mechanics of web panel postbuckling behavior in shear. *Journal of Structural Engineering,* 132**,** 1580-1589.

YU, H., BURGESS, I., DAVISON, J. & PLANK, R. 2009a. Development of a yield-line model for endplate connections in fire. *Journal of Constructional Steel Research,* 65**,** 1279-1289.

YU, H., BURGESS, I., DAVISON, J. & PLANK, R. 2009b. Tying capacity of web cleat connections in fire, Part 1: Test and finite element simulation. *Engineering structures,* 31**,** 651-663.

YU, H., BURGESS, I., DAVISON, J. & PLANK, R. 2009c. Tying capacity of web cleat connections in fire, Part 2: Development of component-based model. *Engineering structures,* 31**,** 697-708.

APPENDIX

ccccccccccccccccccccccccccccccccccccccccccccccccccccccccccccccccccccccccccccccccccccccccccccccccccccccccc

%% The Axial Force of the Bottom Compressive Spring

Temp (°C)	Displacement (mm)	Force (N)
20	0.00E+00	0.00E+00
20	-1.71E-06	-1167.488074
20	-3.42E-06	-2332.342904
…		
47.32	-1.93E-01	-414990.9609
70.41	-3.38E-01	-572911.2856
90.42	-7.67E-01	-659107.0365

% The initiation of the Plateau Stage

108.07	-894.6942701	0.00E+00
123.86	-2.155697864	-659107.0365
138.14	-2.709968563	-659107.0365
151.17	-3.223751766	-659107.0365
…		
255.03	-5.288862559	-659107.1322
261.14	-5.347105732	-659107.1322

% The end of the Plateau Stage

272.68	-5.592833806	-637949.3168
278.12	-5.746748902	-641291.606
280.75	-6.015719843	-613967.6826
288.46	-6.148246805	-610770.2471
293.38	-6.364762833	-612527.9996
298.13	-6.669393988	-615211.0043
302.74	-7.033595959	-583766.0762
307.22	-7.212611382	-584091.7757
315.78	-7.374532478	-584745.605
319.88	-7.785005219	-571336.1667
323.88	-7.928091346	-572270.0517
327.77	-8.088997523	-570154.7663
331.57	-8.248150731	-568078.3834
338.88	-8.570414125	-562935.4489
342.4	-8.86638842	-535983.5795
349.21	-8.973590679	-542020.3917
352.51	-9.267675901	-536777.965

355.73	-9.412503184	-533249.5237
361.97	-9.555128787	-530222.5922
365	-9.766866767	-534676.0695
367.97	-9.957780972	-522186.9863
373.73	-10.13856431	-530546.8868
379.28	-10.24177926	-529659.1959
381.98	-10.49865706	-522305.5201
384.63	-10.61857801	-519903.9014
389.8	-10.86044593	-513932.9986
394.79	-10.92410958	-519483.692
397.23	-11.1372007	-515277.8874
401.99	-11.28751609	-504075.3282
404.31	-11.50548656	-499418.2427
408.85	-11.57176787	-499471.7186
411.07	-11.77334763	-494013.1814
415.41	-11.88534219	-488032.3572
417.54	-12.07496457	-484059.3472
421.7	-12.1793867	-478393.6699
423.74	-12.36612613	-474577.1902
427.74	-12.45682816	-469985.8132
429.69	-12.65010763	-465669.8302
431.63	-12.71976402	-465857.7994
435.42	-12.80860389	-462292.1138
437.28	-12.97916779	-458139.7809
439.12	-13.0813893	-453726.1753
442.73	-13.25886092	-447965.0027
444.5	-13.35369756	-445104.1194
451.39	-13.73909954	-429991.9827
454.72	-13.87234082	-425648.6333
461.17	-14.03178071	-416404.9989
464.29	-14.37873332	-410298.4918
467.35	-14.55102928	-404752.0297
473.28	-14.73044155	-397161.0525
476.17	-15.00772656	-393027.0856
478.99	-15.18268817	-386711.3485
484.49	-15.54683945	-374651.9636
487.17	-15.69141698	-369176.9453
492.38	-15.91648312	-368508.6796
497.42	-15.92220819	-375766.7651
499.87	-16.09716945	-375584.1462
502.29	-16.22989879	-371276.5867
507.01	-16.54686738	-358875.0982
509.31	-16.84535563	-340571.678
513.82	-16.9258777	-351677.3689
516.02	-17.29290201	-324960.2157
520.34	-17.55344285	-319358.2388
522.45	-17.66330013	-318113.6636
526.58	-17.9103224	-311316.2574
528.6	-18.06299069	-306958.4386

532.57	-18.16354016	-302774.3382
534.52	-18.40259315	-299188.2762
538.34	-18.52638009	-294891.9613
540.21	-18.73343037	-292084.6157
543.89	-18.93364439	-288109.58
545.69	-19.07720086	-283276.8683
549.24	-19.34305128	-271632.6476
550.98	-19.46860121	-271538.078
554.41	-19.58825232	-273165.9103
556.09	-19.68832168	-271274.695
559.4	-19.90530862	-266517.5339
562.64	-20.02264766	-261253.7001
564.23	-20.21663443	-259183.0986
567.37	-20.43277855	-253895.394
570.45	-20.53648102	-249005.3726
571.96	-20.75629492	-245986.2755
574.94	-20.86236895	-242206.9969
576.41	-21.05508051	-239638.2775
579.31	-21.26502883	-235898.774
582.15	-21.33699038	-232949.9049
583.55	-21.53513575	-230905.4335
586.31	-21.63856777	-227624.2479
587.67	-21.82726248	-225632.1321
590.36	-22.03847815	-221172.0978
591.68	-22.14780582	-218710.1398
594.3	-22.72136021	-194322.7782
596.87	-22.81657866	-192322.2645
599.4	-23.06609863	-193867.5549
601.89	-23.29684195	-189394.0493
603.12	-23.40005368	-189377.387
605.54	-23.73896732	-179955.5126
607.93	-23.75141178	-187643.6763
610.28	-23.76209497	-194044.9555
612.6	-23.86418785	-190823.0797
613.74	-24.04970285	-188087.3408
616	-24.20963426	-186193.7451
618.23	-24.37726993	-184149.2161
619.33	-24.64776207	-175287.4761
621.51	-24.74468698	-177612.1342
623.66	-24.9362864	-174788.8133
624.72	-25.03476689	-173818.2974
626.82	-25.23683515	-171236.8867
628.9	-25.36291765	-167531.4722
629.92	-25.58856943	-166325.222
631.96	-25.79970907	-163023.4535
632.96	-25.92953917	-161665.7542
634.95	-26.28241096	-153264.3438
636.92	-26.37904141	-155030.7178
638.86	-26.51350759	-151830.9795

639.82	-26.74374681	-150204.0343
641.72	-26.98168855	-146691.7921
643.6	-27.08729774	-143091.866
644.53	-27.30986037	-142772.2535
646.37	-27.57228092	-138704.9997
647.29	-27.72180899	-136229.1565
650.89	-27.90399566	-140531.3428
652.66	-28.03049132	-140307.8153
656.13	-28.26350492	-138973.6337
657.84	-28.73215212	-132431.8939
659.53	-28.99669744	-129492.8234
662.85	-29.44646912	-125105.2374
664.48	-29.62524617	-125502.7462
667.69	-30.24154061	-117623.8762
669.27	-30.43719874	-117219.9282
672.39	-30.77601879	-110456.0437
673.92	-31.38666974	-106841.785
675.44	-31.58470872	-106587.3303
676.19	-31.77096186	-103391.0775
676.565	-31.84030033	-104299.39
676.7525	-32.00262448	-100907.4557
676.94	-32.22103807	-101305.6083
677.685	-32.29314508	-99678.70964
678.43	-32.62857849	-99699.29757
679.9	-33.41501939	-97524.24201
681.36	-33.96552705	-93667.51271
682.8	-34.29907822	-92576.41035
684.23	-34.29706636	-89964.08906
687.05	-34.29421898	-84874.00528
688.44	-34.29158189	-81958.33691
689.82	-34.28602104	-78037.64228
692.54	-34.29101631	-76246.07471
693.88	-34.26839924	-66697.95979
695.21	-34.26013936	-62362.49003
697.83	-34.24250551	-53805.53343
699.13	-34.23241306	-49359.74288
701.68	-34.23033272	-47455.86703
702.94	-34.21286067	-41833.01184
704.2	-34.20539044	-39288.5012
705.44	-34.20189375	-37965.29355
707.89	-34.20065228	-37060.99004
709.1	-34.18509492	-32261.47747
710.3	-34.17717648	-29740.54391
711.49	-34.17140109	-27870.39873
712.67	-34.16568507	-26042.72978
715.01	-34.16562102	-25660.08078
716.16	-34.15021325	-21174.97272
717.31	-34.14176343	-18681.63742
718.45	-34.13578176	-16902.82106

720.7	-34.12538614	-13843.77346
721.81	-34.11744738	-11605.43764
722.91	-34.11174444	-9996.938221
725.1	-34.10247051	-7407.719466
726.18	-34.09651884	-5794.138327
727.25	-34.08842427	-3643.497197
728.31	-34.08273413	-2144.776373
730.42	-34.0839769	-2433.304885

% The bottom spring goes into tension

731.46	-34.06431774	0
732.5	-34.05777491	0
734.55	-34.0552123	0
735.56	-34.04236292	0
736.57	-34.03116571	0
738.56	-34.02637352	0
739.55	-34.01711621	0
740.53	-34.011734	0
742.47	-34.00881056	0
743.43	-34.00183908	0
744.39	-33.99567735	0
746.28	-33.99081302	0
747.22	-33.98221695	0
748.15	-33.97681155	0
749.08	-33.97179623	0
750	-33.96659584	0

cccccccccccccccccccccccccccccccccccccccccccccccccccccccccccccccccccccccccccc

%% The Axial Force of the Bottom Tension Spring

Temp (°C)	Displacement (mm)	Force (N)
20	0.00E+00	0.0000
47.32	-3.42E-03	0.0000

…

% The bottom tension force starts to be activated

730.42	-34.07079902	929.6488432
731.46	-34.0646232	2471.137639
732.5	-34.05775442	4145.439403
733.52	-34.05517914	4751.935725
734.55	-34.05055009	5837.205119
735.56	-34.04201453	7808.653645
736.57	-34.03954034	8348.027493
736.57	-34.03119859	10236.65254
738.56	-34.02940311	10561.36037

738.56	-34.01739443	13183.94034
739.55	-34.01710786	13197.1187
740.53	-34.01171865	14292.75878
741.5	-34.00999228	14602.79438
742.47	-34.00550788	15479.42646
743.43	-34.00203406	16134.1537
744.39	-33.99907335	16674.2921
745.34	-33.99568189	17292.32725
745.34	-33.99081299	18258.15276
746.28	-33.98617742	19097.71281
747.22	-33.98162676	19904.60184
748.15	-33.97700714	20709.64641
749.08	-33.9723629	21503.47588
750	-33.97179632	21529.25817

ccccccccccccccccccccccccccccccccccccccccccccccccccccccccccccccccccccccccccccc

%% The Axial Force of the Top Tension Spring

Temp (°C)	Displacement (mm)	Force (N)
20	0.00E+00	0
20	1.71E-06	1167.488075
20	3.42E-06	2332.589756
20	6.85E-06	4665.17947

…

20	3.43E-03	233863.3059
47.32	3.43E-03	7654.946373
70.41	1.27E-02	28308.40344

% The top tension spring goes into compression

90.42	-6.02E-02	0
108.07	-1.19E-01	0

…

% The top tension spring goes into tension again

507.01	0.001077085	1820.733029
509.31	0.002845702	4765.218823
511.58	0.004025214	6677.202861
513.82	0.006451142	10601.57211
516.02	0.005594065	9108.031108
516.02	0.010493704	17085.42543

518.2	0.011500229	18550.94832
520.34	0.013069555	20889.12789
522.45	0.013587999	21519.61965
522.45	0.015002171	23759.27635
524.53	0.016903518	26527.49863
526.58	0.017140564	26656.66929
526.58	0.018863326	29335.87447
528.6	0.020839281	32117.92466
530.6	0.021071895	32185.18356
532.57	0.023893237	36169.20331
532.57	0.024426987	36977.18443
534.52	0.026280135	39428.29282
536.44	0.028171322	41891.85387
538.34	0.02961273	43646.44646
538.34	0.030085656	44343.49664
540.21	0.032158048	46982.41806
542.06	0.033995723	49232.59326
543.89	0.034380768	49355.40559
543.89	0.035426486	50856.58979
545.69	0.038299483	54504.49624
547.48	0.040187021	56693.53892
549.24	0.039995459	55936.82405
550.98	0.04195013	58166.14146
550.98	0.043763665	60680.7065
552.7	0.045554761	62622.65538
554.41	0.04849548	66092.06536
556.09	0.04986914	67385.16443
556.09	0.050441514	68158.57835
557.75	0.052400869	70204.9877
559.4	0.054008726	71743.28046
561.03	0.055325841	72869.65079
562.64	0.058113963	75895.28075
564.23	0.058724566	76047.42537
564.23	0.060745331	78664.28449
565.81	0.062969229	80856.63037
567.37	0.064930351	82674.82599
568.92	0.065799066	83076.11638
570.45	0.068588288	85872.47715
570.45	0.069292582	86754.25228
571.96	0.071297998	88521.00984
573.46	0.073313685	90263.61617
574.94	0.074878605	91424.47412
574.94	0.075358632	92010.5727
576.41	0.077832836	94240.78599
577.87	0.079992869	96049.06766
579.31	0.081208609	96700.6535
580.73	0.083879961	99058.46935
582.15	0.085754996	100431.2453
582.15	0.08648944	101291.3837

583.55	0.088687743	103007.8309
584.93	0.090921651	104735.3211
586.31	0.092507296	105679.6182
586.31	0.093226049	106500.7158
587.67	0.095542403	108248.9217
589.02	0.097354388	109393.5845
590.36	0.100202979	111666.5129
591.68	0.101774721	112489.6397
591.68	0.102621951	113426.0673
593	0.104780847	114856.4032
594.3	0.110370727	119992.1986
595.59	0.111675462	120415.0855
596.87	0.112215276	120004.4887
596.87	0.113481802	121358.9287
599.4	0.11856353	124720.356
600.65	0.120595386	125671.6905
601.89	0.12150805	125307.6982
603.12	0.122807282	125333.6662
603.12	0.124597515	127160.7272
604.34	0.127927706	129206.5756
605.54	0.129944842	129896.827
606.74	0.13141079	130004.6702
607.93	0.133875334	131076.0257
609.11	0.136430608	132201.3957
610.28	0.13904535	133348.8875
611.44	0.142119982	134897.6043
612.6	0.143845532	135123.3503
613.74	0.144752157	134583.2727
613.74	0.147162091	136823.9077
614.88	0.149525754	137588.7763
616	0.152858756	139221.6146
617.12	0.155495673	140169.4165
618.23	0.156789948	139888.1777
619.33	0.157969934	139499.1369
619.33	0.162007307	143009.5684
620.43	0.163520979	142834.1361
621.51	0.166585837	143932.873
622.59	0.169706276	144992.8172
623.66	0.171320958	144817.5971
624.72	0.172550969	144285.4829
624.72	0.17581425	146812.0633
625.78	0.179059016	147757.9099
626.82	0.182827199	149025.2814
627.87	0.184477315	148722.261
628.9	0.186367232	148499.7835
628.9	0.18985098	150939.4765
629.92	0.193259892	151741.4409
630.94	0.196818957	152568.6605
631.96	0.198900765	152412.1433

632.96	0.202685866	153287.7303
632.96	0.204663542	154472.4679
633.96	0.208561134	155306.1137
634.95	0.21437658	157154.2215
635.94	0.216960433	157114.8846
636.92	0.219627426	157101.1611
637.89	0.223140878	157510.5252
638.86	0.225617669	157162.6015
638.86	0.230219542	159665.046
639.82	0.234841595	160482.1737
640.77	0.239642988	161323.0864
641.72	0.244613364	162163.5899
642.66	0.247667718	162087.937
643.6	0.251545357	162338.9214
644.53	0.255114045	162200.1859
644.53	0.259794656	164400.163
645.46	0.265456893	165252.5187
646.37	0.271418921	166170.9696
647.29	0.273994304	165695.4125
647.29	0.277792644	167142.409
649.1	0.289232059	168396.0604
650.89	0.299152505	168890.7613
652.66	0.299720627	165594.7512
652.66	0.314310012	170868.3953
654.4	0.330914926	172925.5867
656.13	0.33710379	171742.0835
656.13	0.343992077	173636.4128
657.84	0.363620757	175781.6322
659.53	0.379929608	176737.5675
659.53	0.382932322	177426.36
661.2	0.402201004	178692.5859
662.85	0.421820114	179697.4318
664.48	0.422901642	176134.7056
664.48	0.443385249	180739.9403
666.09	0.47058715	182344.1701
667.69	0.497282367	183386.0491
669.27	0.498024624	179598.7198
670.84	0.558732153	185160.6014
672.39	0.560029609	181330.5871
672.39	0.599023198	186236.3599
673.92	0.646381665	187138.3502
675.44	0.704275328	187705.858
676.94	0.706112456	183717.3231
676.19	0.736840536	187696.8018
676.94	0.755966356	186223.1479
676.565	0.785853219	188296.7341
676.7525	0.785204514	187486.0498
676.94	0.849214408	187362.8257
678.43	0.849614731	183450.4382

677.685	1.203905596	165290.1646
678.43	1.703570672	185715.2676
679.9	2.525439037	183389.9387
681.36	3.417854191	181080.442
682.8	4.980968688	178802.5507
684.23	6.530419813	176540.5113
685.65	8.44919199	174294.2648
687.05	9.17552572	172079.663
687.05	10.16824034	172079.663
688.44	12.17881107	169880.8934
689.82	12.80953672	167697.9167
689.82	13.7854901	167697.9167
691.19	15.64411213	165530.7723
692.54	15.65851821	163395.2725
692.54	17.42162394	163395.2725
693.88	19.12780115	161275.5853
695.21	19.36993655	159171.7107
695.21	20.89403673	159171.7107
696.53	22.55407265	157083.6683
697.83	24.17612411	155027.2509
699.13	24.23441709	151304.5505
699.13	25.83984427	152970.8336
700.41	27.08522832	151270.3362
701.68	27.18166589	150265.866
701.68	27.8569617	150265.866
702.94	28.62186878	149269.2922
704.2	28.62713221	148188.1344
704.2	29.47961556	148272.7185
705.44	29.9039228	147291.9671
705.44	30.14182143	147291.9671
706.67	30.97252127	146319.1318
707.89	30.97748781	145354.193
707.89	31.63094469	145354.193
709.1	32.33889097	144397.1703
709.1	32.43331054	144397.1703
710.3	33.14180912	143448.0538
711.49	33.14681462	142506.8535
711.49	33.8484659	142506.8535
712.67	34.46223519	141573.5594
712.67	34.54151656	141573.5594
713.85	35.24029312	140640.2653
715.01	35.24529328	139722.7838
715.01	35.92298174	139722.7838
716.16	36.51860354	138813.2184
716.16	36.6015795	138813.2184
717.31	37.27677308	137903.6529
718.45	37.76115456	137001.9938
718.45	37.94739872	137001.9938
719.58	38.61109948	136108.2409

720.7	39.0987274	135222.4041
720.7	39.26959471	135222.4041
721.81	39.94567082	134344.4736
722.91	40.43540298	133474.4494
722.91	40.60191148	133474.4494
724.01	41.25852908	132604.4252
725.1	41.77015811	131742.317
725.1	41.91974432	131742.317
726.18	42.47105851	130888.1152
727.25	42.57014248	129997.1292
727.25	43.22680121	130041.8196
728.31	43.72685355	129203.4401
728.31	43.89046659	129203.4401
729.37	44.4799335	128365.0508
730.42	44.5090803	127534.5776
730.42	45.27982363	127534.5776
731.46	45.9333676	126712.0107
732.5	46.04895952	125889.4437
732.5	46.66861274	125889.4437
733.52	47.07603338	125082.6992
734.55	47.14717912	124268.0385
734.55	48.04645551	124268.0385
735.56	48.42042463	123469.2002
736.57	48.47301344	122670.3619
736.57	49.3831413	122670.3619
737.57	49.74177595	121879.4397
738.56	49.89516871	121096.4238
738.56	50.7509032	121096.4238
739.55	51.14361357	120313.3981
740.53	51.33830552	119538.2885
740.53	52.22632133	119538.2885
741.5	52.71508224	118771.0851
742.47	52.90584813	118003.8916
742.47	53.66279892	118003.8916
743.43	54.31020877	117244.5945
744.39	54.42435374	116485.3072
744.39	55.22004426	116485.3072
745.34	55.92647489	115733.9262
746.28	56.02395664	114990.4515
746.28	56.80769469	114990.4515
747.22	57.53582525	114246.9768
747.22	57.57618736	114246.9768
748.15	58.35567559	113511.4182
749.08	58.5535167	112775.8497
749.08	59.16735787	112775.8497
750	59.9594339	112048.1974

cccccccccccccccccccccccccccccccccccccccccccccccccccccccccccccccccccccccccccccccccc

%% The Axial Force of the Top Compressive Spring

Temp (°C)	Displacement (mm)	Force (N)
20	0.00E+00	0
20	1.71E-06	0
20	3.42E-06	0
20	6.85E-06	0

…

% The top compressive spring is activited

70.41	-0.060164448	-134126.0182
90.42	-0.118819559	-264887.2356
99.245	-0.118819559	-264887.236
99.245	-0.130815683	-291630.4766
108.07	-0.130718145	-291413.0329
123.86	-0.114739141	-255790.6629
138.14	-0.11603108	-258670.8125
151.17	-0.111104683	-247688.2805
163.17	-0.105928747	-236149.4454
163.17	-0.092095255	-205310.1152
174.27	-0.093941571	-209426.1527
184.61	-0.095278979	-212407.6663
194.28	-0.091665778	-204352.6735
194.28	-0.089189411	-198832.0505
203.36	-0.086237461	-192251.1982
211.92	-0.083818634	-186858.8514
220.03	-0.081968921	-182735.2427
227.71	-0.079287845	-176758.2572
235.02	-0.077152413	-171997.6874
241.99	-0.075166487	-167570.4167
248.65	-0.073203057	-163193.2955
255.03	-0.071550254	-159508.6619
261.14	-0.070971972	-158219.486
261.14	-0.069124089	-154099.9552
267.02	-0.067425364	-150312.9495
272.68	-0.065201872	-145356.0651
272.68	-0.065357889	-145703.8784
278.12	-0.064029536	-142742.5498
278.12	-0.061723744	-137602.1927
283.38	0.233220655	0
280.75	-0.060937513	-135849.429
283.38	-0.064474276	-143734.0186

283.38	-0.063250268	-141005.3083
288.46	-0.059436006	-132502.0853
288.46	-0.059443407	-132518.5851
293.38	-0.058747426	-130967.0175
298.13	-0.058750058	-130972.8844
298.13	-0.058569558	-130570.4915
302.74	-0.059901208	-133539.1698
302.74	-0.057169129	-127448.4818
307.22	-0.057727658	-128693.6251
311.56	-0.059100953	-131755.1437
311.56	-0.056606565	-126194.3452
315.78	-0.055594981	-123939.1972
319.88	-0.055579619	-123904.9518
319.88	-0.055415745	-123539.623
323.88	-0.055742375	-124267.7864
323.88	-0.054777578	-122116.9424
327.77	-0.053907503	-120177.2633
331.57	-0.054591298	-121701.6625
331.57	-0.053276067	-118769.5884
335.27	-0.053348008	-118929.9668
338.88	-0.052891595	-117912.4748
338.88	-0.052954369	-118052.4189
342.4	-0.051882515	-115662.9093
345.85	-0.051598491	-115029.7282
345.85	-0.052197127	-116364.281
349.21	-0.051425978	-114645.1405
352.51	-0.051747123	-115361.0776
352.51	-0.051091227	-113898.873
355.73	-0.050517411	-112619.6523
358.88	-0.050794326	-113236.9843
358.88	-0.050186732	-111882.461
361.97	-0.049887952	-111216.383
365	-0.049804442	-111030.213
365	-0.049485761	-110319.7695
367.97	-0.048822669	-108841.5229
370.88	-0.048690079	-108545.9375
373.73	-0.049016953	-109274.6463
376.53	-0.047862863	-106701.8053
376.53	-0.047395841	-105660.662
379.28	-0.047035866	-104858.1625
381.98	-0.047226758	-105283.7211
384.63	-0.046674615	-104052.8151
384.63	-0.046459839	-103574.0099
387.24	-0.046308773	-103237.2355
389.8	-0.046300531	-103218.8608
392.32	-0.046001624	-102552.5022
392.32	-0.04574957	-101990.5904
394.79	-0.045021861	-100368.2933
397.23	-0.045424419	-101265.7249

399.63	-0.044859695	-100006.7713
399.63	-0.044450437	-99094.40362
401.99	-0.044021932	-97709.4729
404.31	-0.044644015	-98582.24499
406.6	-0.043280823	-95085.96704
406.6	-0.042584352	-93555.85253
408.85	-0.0414401	-90584.68222
411.07	-0.042247625	-91889.87269
413.26	-0.04096151	-88652.5656
413.26	-0.040140043	-86874.673
415.41	-0.039327585	-84701.58935
417.54	-0.038654299	-82847.692
419.64	-0.039163719	-83536.16312
419.64	-0.037946953	-80940.8037
421.7	-0.037275082	-79131.10483
423.74	-0.036670749	-77481.26783
425.75	-0.037326267	-78498.34236
425.75	-0.035984013	-75675.53937
427.74	-0.035253262	-73794.67556
429.69	-0.036083092	-75186.64632
429.69	-0.034668446	-72238.93499
431.63	-0.03408755	-70704.17876
433.54	-0.035412313	-73120.26889
433.54	-0.033887665	-69972.13597
435.42	-0.032234024	-66260.44013
437.28	-0.033934002	-69445.36573
437.28	-0.031855758	-65192.27422
439.12	-0.031252685	-63676.05969
440.94	-0.031146333	-63181.35631
442.73	-0.031336067	-63291.13428
442.73	-0.029783644	-60155.62282
444.5	-0.029861575	-60053.79638
447.99	-0.028720818	-57268.04317
451.39	-0.028624583	-56598.82923
451.39	-0.027119888	-53623.62514
454.72	-0.023938692	-46942.54197
457.98	-0.02660185	-51739.52801
457.98	-0.022137345	-43056.24457
461.17	-0.021381957	-41252.51983
464.29	-0.02368058	-45324.92384
464.29	-0.02075384	-39723.10564
467.35	-0.019539019	-37104.68795
470.35	-0.02133696	-40205.041
470.35	-0.01825672	-34400.9736
473.28	-0.017105174	-31985.3191
476.17	-0.018713411	-34727.35143
476.17	-0.015459027	-28688.03837
478.99	-0.014651832	-26987.4456
481.77	-0.016433562	-30045.17675

484.49	-0.013396345	-24313.57815
484.49	-0.012887332	-23389.74906
487.17	-0.011142816	-20077.09301
489.8	-0.01181797	-21141.14634
492.38	-0.012159943	-21599.03293
492.38	-0.009346023	-16600.82346
494.92	-0.007648054	-13489.53892
497.42	-0.00307985	-5394.436384
499.87	-0.005999254	-10435.76043
502.29	-0.004110312	-7082.258334
502.29	-0.002160876	-3723.289634
504.67	-0.000855568	-1460.111282
507.01	0.001077083	0
…		
509.31	0.00284568	0
…		
550.98	0.043763328	0